The Application of Nonlinear Dynamics to Ship Roll and Capsize

Ben Cotton

Thesis submitted for the degree of

Doctor of Philosophy

Centre for Nonlinear Dynamics and its Applications

University College London

October 1999

Acknowledgements

I would firstly like to thank the Centre for Nonlinear Dynamics and everyone there for their assistance in all aspects of my work over the last three years. I would like to express my gratitude to my supervisor Professor Michael Thompson for initiating my interest in this area and for helping me reach this stage. Thanks also to Dr. Kostas Spyrou for his guidance and many stimulating conversations during his time at UCL. I would also like to thank Professor Steven Bishop for his help and contributions to this work.

I would furthermore like to thank Dr. David Wagg, Robert Sturman, Giovanni Santoboni and Sakse Orstavik for their spirited assistance on numerous occasions.

This research was funded with the help of the Defence Evaluation and Research Agency, and I would like to thank Paul Crossland and Mike Johnson of DERA Haslar for their assistance in our experimental program in particular. Thanks also to the technicians at UCL for their invaluable assistance during our experiments here.

Finally, thanks to Fiona for encouraging me in the first place, my friends for keeping me sane throughout and to Cain for helping me finish the job.

Abstract

In this thesis we study a single degree of freedom model for ship roll motion. We model roll motion as a forced oscillator in a nonlinear potential well. By considering capsize as escape from this potential well, we have been able to apply many of the techniques of nonlinear dynamics developed in recent years to predict and better understand this behaviour.

It has been found in previous studies that bias in the restoring force for nonlinear oscillators can have a significant effect on the steady state solutions and, importantly for escape, reduce the region in which safe solutions exist. Using a parameterised family of restoring functions, the significance of bias for steady state solutions is investigated further. In particular we study the frequency dependence of such symmetry breaking and associate the observed behaviour with the bifurcations in parameter space. We then study some aspects of the application of Melnikov's method for the location of saddle connection orbits, which can cause a dramatic increase in the likelihood of transient motions leading to escape. Again we are interested in how this method should be applied to slightly biased systems.

We then study the modelling of damping functions and how this can affect capsize. Using Melnikov's Method we develop a new concept of equivalent linear damping, specifically designed to model damping close to capsize amplitudes. We accompany this theoretical work with results from a series of large angle roll decay tests and the key features of damping at capsize amplitudes is discussed.

The predictions from the theoretical work within this thesis and previous studies are then tested against capsize experiments conducted with a specially designed

prismatic model. Here we are interested in how well the single degree of freedom roll model approximates real roll motion and capsize. Nonlinear features of the roll motion are observed and we also compare the experimental results with the approximate and numerically derived predictions for capsize.

To conclude we discuss the possibilities for future application of these ideas and techniques within the field of ship design. An optimisation based approach to hull design is described and we ask what the next steps should be in the application of the nonlinear dynamical approach to ship capsize.

Contents

List of Figures

List of Tables

Chapter 1

INTRODUCTION

1.0.1 Capsize and design

One of the key steps in the design of a safe ship must be an understanding of the physical mechanisms that lie behind capsize (Francescutto 1993). This need to predict and model capsize has been with us for centuries but two main hurdles have hindered progress; the complexity of the physics and the nonlinearity of the system in question. With the former we refer to the fluid modelling aspects. A ship lies on the boundary between two phases and it is this that causes the physics to be extremely complicated. One example of this is the characterisation of damping. The modelling of viscous damping for a moving object in a fluid is currently a problem tackled using either empirical approaches or highly sophisticated computational fluid dynamics.

Even assuming we have a physically realistic model for our ship system we are then confronted with the nonlinearity in the equations of motion. The severest aspect of this is introduced through the restoring term. Indeed the very nature of capsize demands that this term be strongly nonlinear since we require the restoring force to drop to zero as roll angle increases for capsize to be a realistic possibility.

In the past studies into ship motion in general have been restricted by these problems and the science has typically focussed on aspects which are more tractable. For instance, small roll motions can be well modelled by linear approximation with empirically derived models for damping. Models such as these have led to a good understanding of parametric excitation and the subsequent dangers of large roll angles (Kerwin 1955). However, these linear approximations fail to cast any light on the large motions inherent to capsize. In other words, the linear approaches may be able to tell us where dangerous motions occur but cannot inform us how capsize might occur or what steps we might take to prevent it, either at a design or operational stage. As a result the nonlinear dynamical nature of the problem is often poorly appreciated when designing against capsize. Of course one can examine the safety of a new design by extensive experimental testing accompanied by large scale numerical simulations. These approaches are effective but limited in that they often tell us little about how we might progress or where we might be going wrong.

Internationally recognised criteria for safe ship design (Sarchin & Goldberg 1962; Vassalos 1985) reflect this approach and are built upon a largely empirical set of rules. The IMO criteria, for instance, are based largely on the work of Rahola (1939). After collecting data from a number of capsizes, Rahola defined a series of minimum values for parameters connected to ship stability and it is from these that the IMO criteria originate (de Souza 1995). Despite the somewhat arbitrary nature of these criteria they have been reasonably successful when applied to conventional ship forms and perhaps this is why they are still with us today. However, it is largely accepted that there is a need for more rational criteria, particularly with the proliferation of less conventional hull designs. One of the key failings, at least from a scientific perspective, is the lack of incorporation of the dynamical nature of capsize. Another more practical concern is that they may be over conservative.

In more recent times the use of numerical simulations along with some new analytic techniques has hugely enhanced our understanding of nonlinear ship roll motions (Nayfeh & Sanchez 1990; Falzarano, Esparza & Mulk 1995; Thompson 1997) and we seek to continue this approach.

From a naval architecture perspective, capsize is considered to occur via four basic mechanisms. These are typically referred to as pure loss of stability, broaching, parametric resonance and beam sea capsize. These mechanisms are briefly described below:

pure loss of stability	is the loss of static stability when buoyancy is lost as a boat sits on the crest of a wave - the upright position can lose stability in this way,
broaching	is a poorly understood phenomenon loosely characterised by sudden turning and heeling after surf riding. It is the dramatic heeling that may lead to capsize (Spyrou 1996a),
parametric resonance	occurs when waves from behind excite the vessel at twice the natural roll frequency thus leading to large resonant roll amplitudes and possibly capsize (Kerwin 1955),
beam sea capsize	is caused by waves from the side directly exciting large angle roll motions.

Whilst the modelling of these mechanisms has often taken a multi degree of freedom approach (Kan, Saruta & Taguchi 1991; Spyrou 1996b) the ultimate precursor of *intact* capsize must be large angle roll motion. For this reason we focus on the

problem of beam sea roll.

1.0.2 The single degree of freedom roll model

One of the earliest attempts to model the rolling of ships was that of Froude (1874) in which the nonlinear nature of the problem was identified. The introduction of steam powered vessels in the last century had lead to the unforseen increase in problems with roll due to the removal of the steadying effect of sails (Lloyd 1989). Having initiated the building of the world's first towing tank, Froude persuaded the British Government to allow him to perform tests aimed at exploring the problem of roll. Since then many different roll models of varying complexity have been proposed and there seems little consensus on the use of these models. In this work we use the formulation of Thompson, Rainey & Soliman (1992). One of the aspects we wish to study is the effectiveness of this model for predicting capsize, as well as determining its limitations.

By studying how we model this reduced system we hope to gain a better understanding of both capsize and the modelling process. Previous studies of this model have found the dynamics to be generally robust to choice of restoring or damping. However, sensitivity to features such as symmetry has also been observed and one of the main themes of this thesis is the determination of the limitations of this approach.

1.0.3 Objectives of the work

In recent years considerable advances have been made in the study of the single degree of freedom roll equation with the application of global geometrical techniques to the generalised problem of escape of a driven oscillator from a potential

well (Thompson, Rainey & Soliman 1990; Thompson 1997; Nayfeh & Khdeir 1986; Nayfeh & Sanchez 1990; Bikdash, Balachandran & Nayfeh 1994; Falzarano, Shaw & Troesch 1992). These advances have suggested a number of important new approaches to the modelling of capsize for design, as well as the development of new safety criteria. However, a frequent criticism has been that these new techniques are often inapplicable to the real problems faced by naval architects. One of the primary objectives of this work is to take a first step towards bridging this gap.

In applying nonlinear dynamics to the ship roll and capsize, it is helpful to write down some of the basic issues to be confronted.

1. To what extent do the simple approaches used in most nonlinear studies provide physically realistic models of real ship roll and capsize ?
2. With the enormously diverse behaviour seen in these nonlinear systems, what aspects are relevant for ship roll and capsize ?
3. How robust are these new methods for predicting capsize ?
4. How can we develop the techniques of nonlinear dynamics for use as part of a design process ?

The first problem is essentially a matter of where the simple models are physically valid. A simple example of this is the single degree of freedom roll model which assumes that the waves are long compared to the beam of the ship. This implies the existence of a short wavelength limitation to our model. While we clearly need to understand the limits of this approach it should be noted that dynamics observed beyond these limits may still be relevant. In this work we try to reconcile these differences, studying the more general nonlinear dynamics problems but highlighting the areas which are relevant for ship roll and capsize.

The second, more subtle issue, is whether the complicated nonlinear dynamics observed in numerically based studies actually occur in a real system. It is here

that the relative lack of activity in the experimental field (see for example Contento & Francescutto (1997)) has hindered progress. It is generally acknowledged that many of the rich dynamics observed in nonlinear systems are highly unlikely to be found in real ship motions, or even carefully conducted roll experiments. However, this does not imply that some of the consequences of the nonlinear behaviour are not relevant. For instance, the fractal basin boundaries and chaotic responses commonly seen in nonlinear oscillators may not be directly observed in experiment, yet the capsize predictions derived from these features may still be of use.

The third issue is a key one if the methods discussed in this thesis are to be applied to design or used to develop new criteria. We must be careful that a technique for predicting, for instance, a capsize boundary, is not sensitive to the way we have modelled the motion. One example of this is the studies of MacMaster & Thompson (1994) and Thompson (1997) which have highlighted the significance of symmetry and the importance of studying biased models.

Finally, as a theme running throughout, we wish to link the nonlinear dynamics to ship design - a problem that has, to this date been somewhat neglected (Spyrou, Cotton & Thompson 1997). Whilst we in no way attempt to produce a full design methodology, we repeatedly highlight how one might use the ideas and techniques developed in this work as part of a design process.

1.0.4 Overview

In this thesis we study the application of nonlinear methods to roll and capsize modelling. The focus is chiefly on the importance of the model we use and the effectiveness of our capsize prediction methods. We use simple models for restoring and damping throughout and the validity of this approach is addressed in a series of roll experiments, the results of which are presented herein.

We begin by describing the basic formulation of our equations of motion in chapter 2. This involves framing the problem of roll and capsize as one of a nonlinear oscillator in a potential well. As part of this process we examine the limitations of the model and derive formulae for these which we apply in the following chapters. We also describe some important aspects of the nondimensional equations and, by performing a linear capsize analysis, derive a simple design formula.

In chapter 3 we review the nonlinear dynamics of nonlinear oscillators, focussing on the escape of trajectories from potential wells. We look at the techniques available for analysing both steady state and transient escape, and discuss how they might be used for capsize prediction. As part of a discussion of the steady and transient dynamics typical to these models, we also present updated bifurcation diagrams and cellmaps for a new region of parameter space previously considered unimportant for capsize.

Previous studies have found a strong sensitivity of the steady state solutions to symmetry in restoring (MacMaster & Thompson 1994; Thompson 1997), a feature that has considerable implications for capsize testing. Using the concept of sustainable wave slope, these studies suggest that a small added bias can dramatically reduce the wave slope required to cause capsize. In chapter 4 we address the effect of bias in the restoring force over a range of forcing frequencies. We also associate the sensitivity with particular bifurcations in parameter space.

Melnikov's Method for approximately locating saddle connection orbits has been observed to provide good lower bounds for the existence of homoclinic tangencies and consequently the erosion of the safe basin of initial conditions (Foale & Thompson 1991). This technique seems to have good prospects for use as a design tool and we are interested in testing it further. The issue of symmetry is further explored in chapter 5 where saddle connections and the use of Melnikov's Method

for slightly biased systems are studied.

In chapter 6 we study the modelling of damping and how our choice of nonlinear damping model may affect predictions for capsize. Rather than trying to develop damping models that give accurate predictions for the roll motion alone, we study how one might model damping specifically for capsize. To this end we further develop the concept of a Melnikov equivalent damping (a concept first mooted by Bikdash, Balachandran & Nayfeh (1994)) and use the idea to justify the use of linear damping models for capsize. Also described here are some of the consequences of using this new equivalent damping within the simple design formula. This theoretical study of damping is accompanied by the results from a series of large angle roll decay tests in chapter 7, in which we have measured the effects of hull appendages on the nonlinear components of roll damping.

In chapter 8 we present a series of experiments conducted with the aim of validating the use of the single degree of freedom model as well as enhancing our characterisation of the terms in the equations of motion. These experiments were not designed to model real ship motion but rather to test the use of nonlinear dynamical methods for a real floating system. A number of important nonlinear features are observed in the data and the capsize tests are found to fit well with the theoretical and numerically derived predictions.

In the final chapter we summarise the findings in this thesis and highlight the key observations. To conclude we discuss some of the prospects for developing these techniques and ideas for design.

Chapter 2

ROLL MOTION AS A NONLINEAR OSCILLATOR

2.1 Introduction

The nonlinear modelling of roll and capsize as escape from a potential well was mapped out by Thompson, Rainey & Soliman (1990). This has proved an extremely effective approach, enabling a number of techniques developed for more general problems to be applied to the modelling and understanding of capsize (Virgin 1989; Foale & Thompson 1991; Kan, Saruta & Taguchi 1991; Bikdash, Balachandran & Nayfeh 1994; Nayfeh & Balachandran 1995; Thompson 1997).

In this chapter we follow this approach, formulating a single degree of freedom model for roll motion and rewriting it as a nondimensional nonlinear oscillator. The use of this single degree of freedom equation of motion was initially motivated by a desire to understand the dynamics of this simpler model. However we are now also interested in the accuracy of such models when modelling real roll and capsize. For this reason we also derive a nondimensional measure of wave slope

which is found to highlight features of the dynamics particularly relevant for ship roll motion.

Finally we note some important consequences of the formulation and describe the derivation of a simple design formula (Thompson 1997).

2.2 Equation of motion in beam waves

2.2.1 Deriving the roll equation

We firstly assume that a boat in a long beam wave in deep water follows the circular motions of a water particle in the wave. If the gravitational acceleration is then combined vectorially with the centrifugal acceleration, an effective gravitational field normal to the instantaneous wave surface is obtained (Thompson, Rainey & Soliman 1992). We also employ the Froude-Krilov assumption that the wave pressures are unaffected by the ship, so that the usual calm-water restoring moments act to keep the ship normal to the wave surface. Under these assumptions the ship will behave as if it were a rotational oscillator, tied by a nonlinear rotational restoring force to the wave normal.

Using this formulation, we consider a ship with rotational moment of inertia about its centre of gravity, I (which may also be written $I + \Delta I$ when incorporating an appropriate added hydrodynamic mass). The damping function, which will typically be highly nonlinear, is written as $B(\theta')$. Angle dependence has been omitted for simplicity. Moreover, as pointed out in Haddara & Bennet (1989), the dynamic relationship between angle and velocity implies that angle dependence can be modelled using only velocity dependent terms. The effective restoring moment after addition of any wind loading or cargo imbalance, based on calm-water hydrostatics, is $mgGZ(\theta)$, where m is the mass of the boat, g is the fixed

gravitational constant, and $GZ(\theta)$ is the righting arm. Finally we assume the quasi-static enslavement of the heave, and ignore the small parametric forcing of the fluctuating gravity field. We thus obtain the following equation for roll motion (Thompson, Rainey & Soliman 1992),

$$I\theta'' + B(\theta') + mgGZ(\theta) = IAk\omega_f^2 \sin(\omega_f \tau) \tag{2.1}$$

where the prime denotes differentiation with respect to real (unscaled) time τ, θ is the roll angle relative to the wave normal, Ak is the wave slope amplitude (A is the wave height and k the wave number) and ω_f is the wave frequency. We also write ω_n as the linearised natural frequency of undamped motions and $GM = \frac{dGZ}{d\theta}(0)$ is the metacentric height. The linear coefficient of the damping function is $B_1 = \frac{dB}{d\theta'}$ evaluated at $\theta' = 0$. The linear damping ratio is therefore $\zeta = B_1/\sqrt{4ImgGM} = B_1\omega_n/2mgGM$.

2.3 The scaled equation of motion

Here we follow the work of MacMaster & Thompson (1994) in developing a family of restoring curves that effectively model the addition of varied loading to the ship.

2.3.1 The GZ curve

The original GZ curve of a ship, figure 2.1(a), is derived from a static test in which the moment $mgGZ_0$ required to produce a roll angle θ, measured in radians, is determined. During this test the ship will heave to preserve the vertical static balance; this static enslaved heave will be approximately reproduced under most conditions of dynamic rolling.

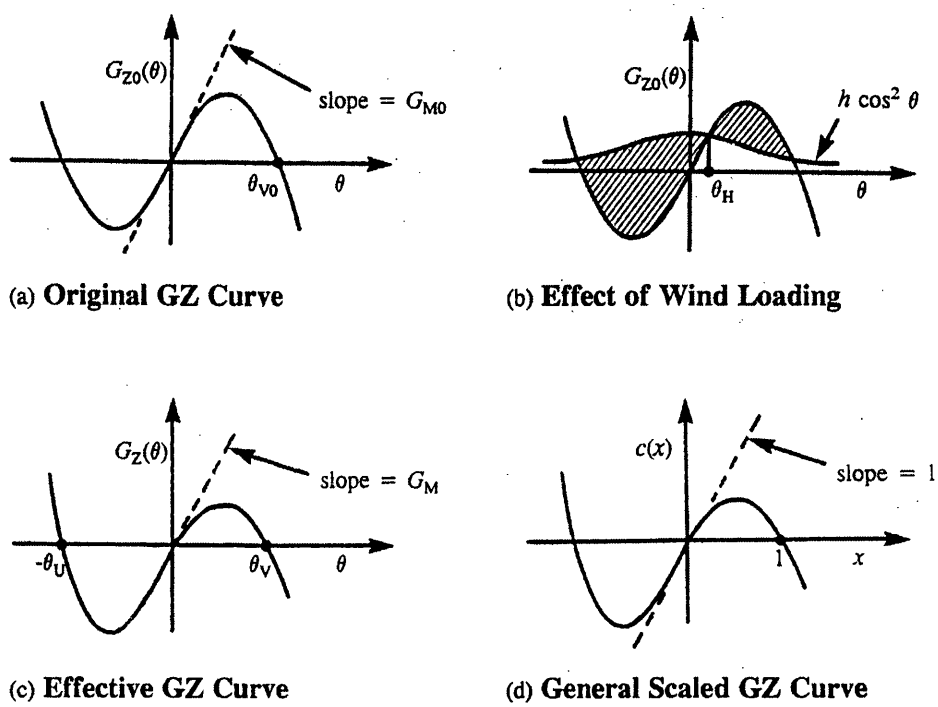

Figure 2.1: The general method for scaling the GZ curve of a ship, taken from Thompson (1997). Note that in this figure G_Z is equivalent to GZ.

For a symmetric ship the GZ curve is odd and hence $GZ_0(\theta) = -GZ_0(-\theta)$. The positive intercept with the θ-axis is the unbiased angle of vanishing stability, θ_{V0} .

In order to study the importance of symmetry in the restoring function, we now wish to incorporate an additional load into the GZ, to produce an effective GZ. This can be illustrated by considering a wind loading moment of the form $h \cos^2 \theta$, as shown in figure 2.1(b). Subtracting this wind moment from $GZ_0(\theta)$ gives us an effective moment that we write as $GZ(\theta)$. Under wind and any other imbalances, we thus write the final effective moment as $GZ(\theta)$, where θ is now measured from the stable heeled state, figure 2.1(c). The two angles of vanishing stability are written as θ_V and θ_U, and we set $\theta_U \geq \theta_V$ (note that both these variables are positive).

We finally scale the effective GZ curve so that it has unit slope at (0, 0) and

passes through (1, 0), as shown in figure 2.1(d). The general scaled GZ curve is written as $c(x) = GZ(x\theta_V)/\theta_V GM$, where the scaled roll angle is $x = \theta/\theta_V$. Here $c(0) = c(1) = 0$ and $dc/dx = 1$ at $x = 0$. Note that the original units of GZ_0 and GZ are now eliminated.

Additionally, under the approximations $\theta_V \approx \theta_{V0} - \theta_H$ and $\theta_U \approx \theta_{V0} + \theta_H$, we have the relationship,

$$\alpha = \frac{\theta_V}{\theta_U} \quad \text{and} \quad \alpha \approx \frac{1-H}{1+H} \tag{2.2}$$

where $H = \theta_H/\theta_{V0}$. This relationship provides a useful way of quantifying the effect of symmetry for the real system, see chapter 4.

2.3.2 The nondimensional equation of motion

The equation of motion (2.1) can now be written in nondimensional form,

$$\ddot{x} + b(\dot{x}) + c(x) = F \sin \omega t \tag{2.3}$$

where $x = \theta/\theta_V$ is the scaled roll angle and a dot denotes differentiation with respect to the scaled time $t = \omega_n \tau$. Note that this scaling ensures that the 'nondimensional angle of vanishing stability' is always equal to 1. We also write $c(x)$ and $b(\dot{x})$ as the restoring and damping functions,

$$b(\dot{x}) = \frac{B(\dot{x}\theta_V\omega_n)}{\theta_V mgGM} \qquad c(x) = \frac{GZ(x\theta_V)}{\theta_V mgGM} \tag{2.4}$$

Similarly, the nondimensional forcing magnitude, F, is given by

$$F = \frac{IAk\omega^2}{(I+\Delta I)\theta_V} \Rightarrow F \approx \frac{Ak\omega^2}{\theta_V} \tag{2.5}$$

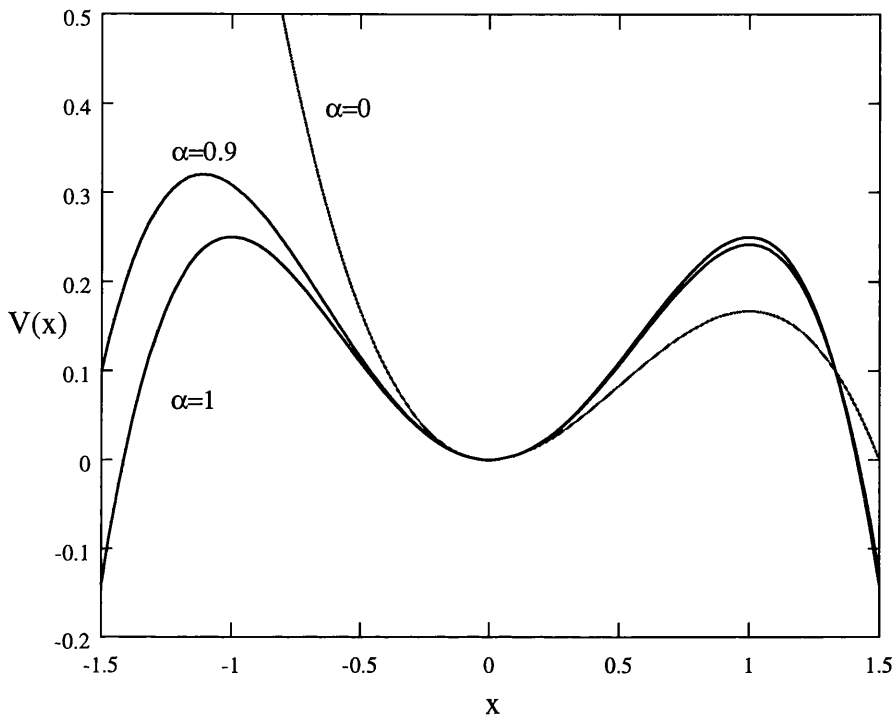

Figure 2.2: The potential wells for the α parameterised restoring.

Now consider the minimum F required to cause capsize at some worse case frequency. Fixing these two parameters at this point gives a simple relationship between sustainable wave slope and θ_V,

$$Ak \propto \theta_V \tag{2.6}$$

2.3.3 Escape from a potential well

In order to approach ship capsize from a nonlinear dynamical viewpoint, it is useful to generalise the problem to that of escape from a potential well. To this end we use a family of nondimensional restoring functions (MacMaster & Thompson 1994), designed to model the effects of bias on the dynamics,

$$c(x) = x(1-x)(1+\alpha x) \tag{2.7}$$

Following the scaling described above, this restoring function has unit slope at $x = 0$ and intercepts the x-axis at $x = 1$. By varying α we may smoothly add bias to the symmetric restoring. This is shown in figure 2.2 in which we plot the potential energy, $V(x) = \int c(x)$ for different values of α. For $\alpha = 0$ (and a linear damping coefficient, β) we recover the archetypal quadratic escape equation (Thompson, Bishop & Leung 1987; Thompson 1989; Szemplinska-Stupnicka 1992),

$$\ddot{x} + \beta\dot{x} + x - x^2 = F \sin \omega t \tag{2.8}$$

and for $\alpha = 1$ we obtain a symmetric escape equation,

$$\ddot{x} + \beta\dot{x} + x - x^3 = F \sin \omega t \tag{2.9}$$

Cubic restoring forces of this form have commonly been used in previous studies of ship roll (Kan, Saruta & Taguchi 1991; Contento & Francescutto 1997), often with an added constant bias force (Cusumano & Kimble 1994; Kan & Taguchi 1991). In fact we may transform the α parameterised restoring used here into the alternative biasing model (Gurd 1997),

$$\ddot{v} + \overline{\beta}\dot{v} + v - v^3 = B + \overline{F} \sin \overline{\omega}\overline{t} \tag{2.10}$$

where

$$\begin{aligned}
v &= x - \frac{(1-\alpha)}{3\alpha}\sqrt{\frac{3\alpha}{\alpha^2+\alpha+1}} & \overline{t} &= t\sqrt{\frac{\alpha^2+\alpha+1}{3\alpha}} \\
\overline{\beta} &= \beta\sqrt{\frac{3\alpha}{\alpha^2+\alpha+1}} & B &= \frac{(1-\alpha)(2\alpha^2+5\alpha+2)}{3\sqrt{3}(\alpha^2+\alpha+1)^{(3/2)}} \\
\overline{F} &= F\frac{3\alpha^2\sqrt{3}}{(\alpha^2+\alpha+1)^{(3/2)}} & \overline{\omega} &= \omega\sqrt{\frac{3\alpha}{\alpha^2+\alpha+1}}
\end{aligned} \tag{2.11}$$

The dynamics of these equations have been extensively studied in the past (Thompson, Bishop & Leung 1987; Thompson 1989; Szemplinska-Stupnicka 1992; Bikdash, Balachandran & Nayfeh 1994) and escape from the potential wells (equivalent to capsize) in such systems is well understood. In chapter 3 we describe the important results from previous studies and illustrate their significance for capsize and ship rolling in general.

2.4 Limits to the model validity

We now wish to determine the theoretical limits of our model for roll motion. Here we are chiefly interested in the limits within the parameter space spanned by forcing amplitude and frequency.

2.4.1 Wave breaking limit

The first limit is a consequence of the nature of water waves. For a slope above $Ak \approx \pi/7$ a wave will break and the use of a simple sinusoidal forcing is no longer valid. Hence,

$$Ak^{max} \approx \frac{\pi}{7} \tag{2.12}$$

$$\Rightarrow F^{max} \approx \frac{\pi}{7\theta_V}\omega^2 \tag{2.13}$$

2.4.2 Short wavelength limit

A further assumption is that the ship tries to follow the motions of the water particles in the wave and does not interfere with the pressures in the wave. This is only valid when the beam of the ship is small compared to the wavelength. We

can thus write a minimum wavelength, λ^{min}, permissible in terms of the beam, b

$$\lambda^{min} = \epsilon b \tag{2.14}$$

where we take, as a first estimate, $\epsilon \approx 6$. This in turn gives us a maximum forcing frequency

$$\omega_f^{max} = \sqrt{\frac{2\pi g}{\lambda^{min}}} = \sqrt{\frac{2\pi g}{\epsilon b}} \tag{2.15}$$

where we have assumed deep water conditions. This then gives us an expression for maximum nondimensional frequency,

$$\omega^{max} = \frac{\omega_f^{max}}{\omega_n} = T_n \sqrt{\frac{g}{2\pi\epsilon b}} \tag{2.16}$$

where ω_n and T_n are the natural roll frequency and period of the ship. Note that this second limit is due to the approximations of our roll model whereas the first is a feature of wave behaviour.

We can also now substitute this result into (2.5) to obtain an overall maximum nondimensional forcing amplitude,

$$F^{max} = \frac{2\pi^2 g}{7\epsilon b \theta_V \omega_n^2} \tag{2.17}$$

Substituting in three real ship values (a purse seiner (Umeda, Hamamoto, Takaishi, Chiba, Matsuda, Sera, Susuki, Spyrou & Watanabe 1995), a container (Takezawa, Hirayama & Acharrya 1990) and our experimental model, chapter 8) for beam dimension and natural frequency we obtain the values for F^{max} in table 2.1.

We have therefore derived rough limits on the validity of our roll model in the forcing amplitude/frequency parameter space. It should be observed that theoretical

Table 2.1: Limits to roll model validity for 3 cases

Ship	θ_V [degrees]	T_n [s]	beam[m]	ω^{max}	F^{max}
Fishing Boat	40	7.47	7.6	1.4	0.63
Container	-	19.4	25.4	1.9	-
UCL model ship	38	0.82	0.18	1.1	0.81

predictions for the parameter regions beyond the limits may still be meaningful, and we use these limits as a guide rather than strict criteria.

2.5 A linear capsize analysis

If we now look at the linear problem we can write the amplitude of steady-state motion by looking at the particular integral of the linearised, dimensional roll equation,

$$I\theta'' + B_1\theta' + mgGM\theta = IAk\omega_f^2 \sin\omega_f\tau \tag{2.18}$$

Assuming a solution of the form

$$\theta = \theta_m \sin(w_f\tau + \phi) \tag{2.19}$$

we can substitute into (2.18) and solve to find

$$\theta_m = \frac{IAk\omega_f \sin(\phi)}{B_1} \qquad \phi = \frac{\pi}{2} - \sin^{-1}\left(\frac{\theta_m(\omega_f^2/\omega_n^2 - 1)}{Ak}\right) \tag{2.20}$$

So assuming once more that we are always tuned to resonance with $\omega_f = \omega_n = \sqrt{\frac{mgGM}{I}}$, the linearised result 2.20 gives us the maximum roll angle θ_m,

as

$$\theta_m = \frac{Ak\sqrt{ImgGM}}{B_1} = \frac{Ak}{2\zeta} \tag{2.21}$$

where $\zeta = \frac{B_1}{2\sqrt{ImgGM}}$ is the equivalent damping ratio.

If we now make the rather crude assumption that capsize is likely to occur when the maximum amplitude is a multiple of the angle of vanishing stability, or $\theta_m = \mu\theta_V$, we find that

$$\text{Critical wave slope} = Ak = 2\mu\zeta\theta_V \tag{2.22}$$

which we will refer to as the simple design formula (SDF) (Thompson 1997; Thompson *et al.* 1998). The validity of this simple formula and the assumptions upon which it is based are confirmed in later chapters using numerical and analytic evidence. In particular we justify setting $\mu = 1$ by comparison with Melnikov's Method, see chapter 3, section 3.3.3.

Reassuringly, this simple equation, with $\mu = 1$, gives a plausible practical answer. If the severest wave slope encountered by a boat is $\pi/7$ radians and θ_V has a typical value of about $\pi/4$ radians, the effective linear damping ratio needed to prevent capsize is predicted to be $\zeta \approx 0.3$. Note that this seemingly high ratio is the linear damping required to prevent capsize; a nonlinearly damped system would typically require a much lower linear damping term. The importance of nonlinear damping is discussed in depth in chapter 6.

2.5.1 Nondimensional wave slope

For practical purposes we require a sensible measure of wave forcing. The most widely used measure is that of the wave slope Ak but this has dimension and hence

sits uncomfortably with our nondimensional approach. Also commonly used is the nondimensional F. However, we may now use the SDF to introduce a scaled wave slope, J such that

$$J = \frac{Ak}{2\zeta\theta_V} \tag{2.23}$$

We can thus construct a universal capsize diagram (Thompson 1997) by plotting capsize as a function of J and ω. The simple design formula predicts that capsize will occur for forcing levels greater than $J = 1$.

2.5.2 Interpreting the simple design formula

From the simple design formula (SDF), equation (2.22), we can immediately make some simple observations about the hull characteristics needed to resist capsize under beam sea resonance.

Resistance to capsize is provided by the product

$$Ak = 2\zeta\theta_V = B_1\theta_V/\sqrt{ImgGM} \tag{2.24}$$

Clearly we want the highest possible damping coefficient B_1, and the lowest possible inertia I - the latter statement of which is surprising. Focussing on the remaining two items which derive from the restoring moment $mgGZ(\theta)$, we have

$$GZ \text{ capsize resistance} = \theta_V/\sqrt{mgGM} \tag{2.25}$$

which seems to suggest that capsize resistance is to be improved by a high angle of vanishing stability, and a low GM. This latter result warrants further discussion.

Let us assume that we fit the effective GZ restoring function of a heavily-biased

boat in the presence of wind loading with a simple quadratic so that

$$mgGZ(\theta) = mgGM\theta(1 - \theta/\theta_V) \tag{2.26}$$

The potential energy function is then the integral of (2.26),

$$V(\theta) = \frac{1}{2}mgGM\theta^2 - mgGM\theta^3/3\theta_V \tag{2.27}$$

so the height of the potential barrier preventing capsize, H_B, is therefore,

$$H_B = V(\theta_V) = mgGM\theta_V^2/6. \tag{2.28}$$

Using this expression we can write the hydrostatic resistance to capsize, (2.25), in the three alternative forms

$$GZ \text{ capsize resistance} = \frac{\theta_V}{\sqrt{mgGM}} = \frac{\sqrt{6H_B}}{mgGM} = \frac{\theta_V^2}{\sqrt{6H_B}}. \tag{2.29}$$

We therefore see various counter-intuitive results, deriving from the fact that raising the restoring moment of inertia can increase the likelihood of capsize because it can lower the damping ratio. However, we must be careful with these interpretations as the linear damping assumed here has a significant effect on the outcome of the above analysis. For a fuller picture we repeat the above approach in chapter 6 using instead an improved design formula, which uses a capsize based method for incorporating nonlinear damping.

Chapter 3

DYNAMICS AND ESCAPE IN NONLINEAR OSCILLATORS

3.1 Introduction

In chapter 2 we have shown how the roll motion of a ship in beam seas can be written as a single degree of freedom nonlinear oscillator and capsize modelled as escape from a potential well. In recent years considerable progress has been made in the study of the generalised problem of escape from a potential well. Perhaps one of the first efforts to appreciate the applicability of nonlinear dynamics for the ship stability problem was that of Odabasi (1982), who discussed the use of topological dynamics and considered phase space approaches to stability assessment. This was taken further by Nayfeh & Khdeir (1986) who used harmonic balance methods and numerical simulations to locate bifurcations and chaotic motions in a single degree of freedom roll model.

In recent years considerable progress has been made in the study of the generalised problem of escape from a potential well. An early investigation of the dynamics of

the quadratic escape equation was made by Thompson, Bishop & Leung (1987). In this paper a number of escape related nonlinear phenomena were highlighted. These included the significance of homoclinic tangencies, fractal basin boundaries and a complex bifurcational structure. The use of Melnikov's Method for locating saddle connections was also highlighted.

These studies were followed by a number of works investigating the dynamics of these simple nonlinear oscillators (Thompson 1989; Thompson 1997; Szemplinska-Stupnicka 1992). The application of these approaches to ship capsize was also taken further with the development of new safety criteria considered by Thompson, Rainey & Soliman (1990). The use of these global methods for predicting capsize was also considered by Falzarano, Shaw & Troesch (1992) and Falzarano, Esparza & Mulk (1995).

An important factor to note is the remarkable robustness of these simple models; changes in the potential function for instance generally have little effect on the dynamics, from a quantitative as well as qualitative perspective (Lansbury *et al.* 1992; Stewart *et al.* 1995). For this reason we can expect the analysis of these simple models to have considerable relevance for more complex ones. Given the difficulty in analysing even the simplest of nonlinear systems, this feature is extremely useful. It is therefore important that we question this robustness and explore its limitations. In chapter 4 we discuss a sensitivity to symmetry in restoring which is an example of this issue.

Described here are some of the methods available for analysing these dynamics and predicting phenomena such as escape, illustrated with some new results. In doing this we consider transient and steady state behaviour separately. It is transient motion that is typically associated with capsize and since the actual wave forcing experienced by a real ship is irregular, the ship will never truly be in a steady

state. However it is the steady state solutions and bifurcations that define the possible types of motion as we vary system parameters. In particular we focus on the importance of bifurcations in the prediction of escape from a steady state perspective.

We begin by describing the significant steady state solutions over a physically realistic control space. We are primarily interested in varying the frequency and amplitude of forcing, thus loosely modelling the effect of changing wave conditions. By studying the types of steady state solution that exist as we vary these forcing parameters we are able to describe the likely types of motion onto which the system may settle. By locating the bifurcations in these solutions we can then map out different regions of behaviour in parameter space.

Modelling transient motions is extremely difficult but for the prediction of escape from the well, there exist a number of useful approaches. In the second part of this chapter we describe the transient problem and present some numerical results illustrating the important concepts such as the safe basin of attraction and the Dover Cliff (Foale & Thompson 1991).

In describing this general approach we also briefly describe some of the standard numerical algorithms used in this thesis and the theoretical concepts that lie behind them.

3.2 Steady state dynamics

In the nonlinear oscillator model for roll motion, escape from the potential well is equivalent to capsize and we are therefore interested in how this might occur. One approach is to consider the steady state oscillations and where they do, or do not, exist. For a nonlinear system there will typically be a multitude of steady states

and we concentrate only on those onto which the system has a reasonable chance of settling. This is ultimately determined by the basins of attraction of the steady states and we discuss these further in section 3.3.

We discuss firstly the slow[1] increase of forcing amplitude (or, equivalently, wave slope) from zero. One can think of this as a ship in initially calm waters, faced by slowly varying waves of ever increasing slope. In this way we review the mechanisms for escape from the potential well using the canonical escape equation, (Thompson, Bishop & Leung 1987). In our formulation this is equivalent to the $\alpha = 0$ restoring function, equation (2.8). In particular, we associate escape with bifurcations in the dominant steady state solutions. With this approach we do not need to study the actual trajectories in phase space in order to investigate escape from the well.

In considering steady state solutions we frequently use the concept of a Poincaré Section (Thompson & Stewart 1986) taken by sampling the dynamics every forcing period. This reduces the dimension of the phase space from 3 to 2 and is a particularly useful tool for simplifying the problem. For instance, a periodic orbit of period equal to the forcing is represented by a fixed point and we can follow this point as we vary a parameter.

3.2.1 Escape from a cubic potential well

Figure 3.1 shows schematic versions of the steady state solution paths as the parameter, F is slowly and smoothly ramped up (increased) from zero, with initial conditions of $(x = 0, \dot{x} = 0)$ at the start of the ramping. Hence we are crudely modelling a gradual increase in wave slope at constant frequency. In figure 3.2 an actual steady state solution path is plotted. A continuation algorithm (Foale &

[1]slow compared to the dynamics, i.e. we assume that the system is always at steady-state until escape occurs

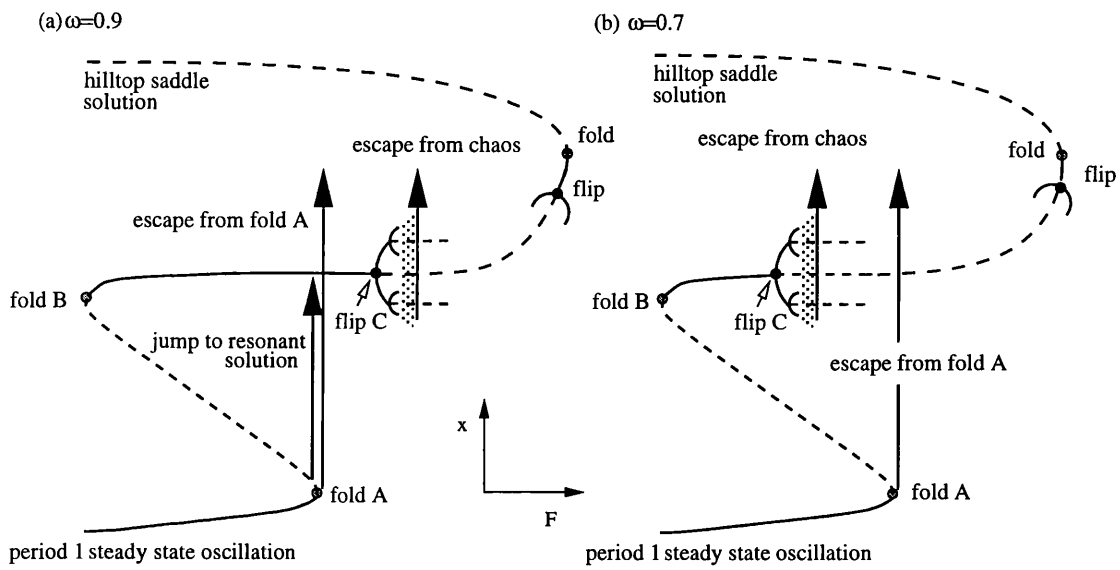

Figure 3.1: Schematic diagrams showing possible steady state paths (dashed = unstable) and escape (capsize) mechanisms, around resonant frequencies. Each represents the roll amplitude plotted against forcing amplitude.

Thompson 1991) has been used to generate the steady state path and the stable parts located by allowing the solution to settle onto a steady state from initial conditions along the solution path. We could also have determined stability by considering the eigenvalues in the Poincaré map at each parameter value. An example of two numerically integrated solutions are shown in figure 3.3.

For this system, as the forcing amplitude is slowly increased, escape may occur in two ways;

(a), the steady state being followed locally ceases to exist for higher F: this occurs at the fold A

(b) the steady state becomes unstable at higher F: this occurs at the final crisis (escape from chaos) - approximately located by the first period doubling bifurcation, C.

In either of these cases, if the current state does not lie in the basin of attraction[2] of

[2]basin of attraction: the set of initial conditions that settle onto a steady state and hence

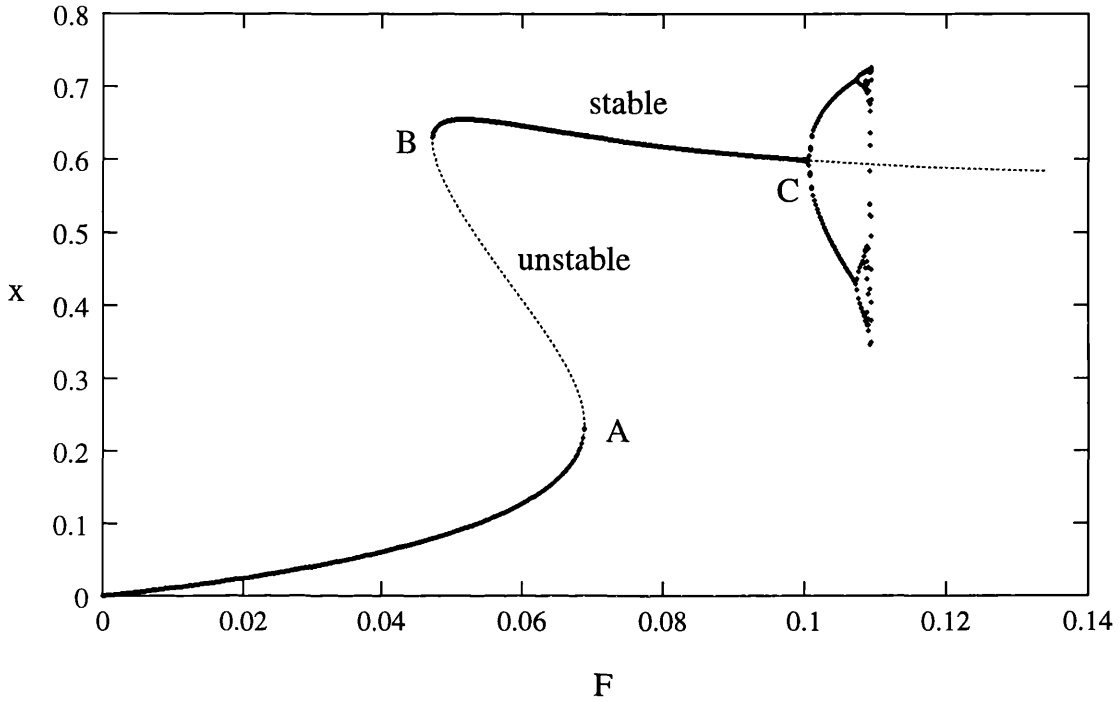

Figure 3.2: A numerically integrated steady state solution path for the $\alpha = 0$ system. The bold dots show the steady state settled onto as F is slowly increased. The dotted lines, generated using a continuation method, show the unstable parts of the period 1 solution path. The period doubling bifurcation at C leads to a cascade to chaos and then escape.

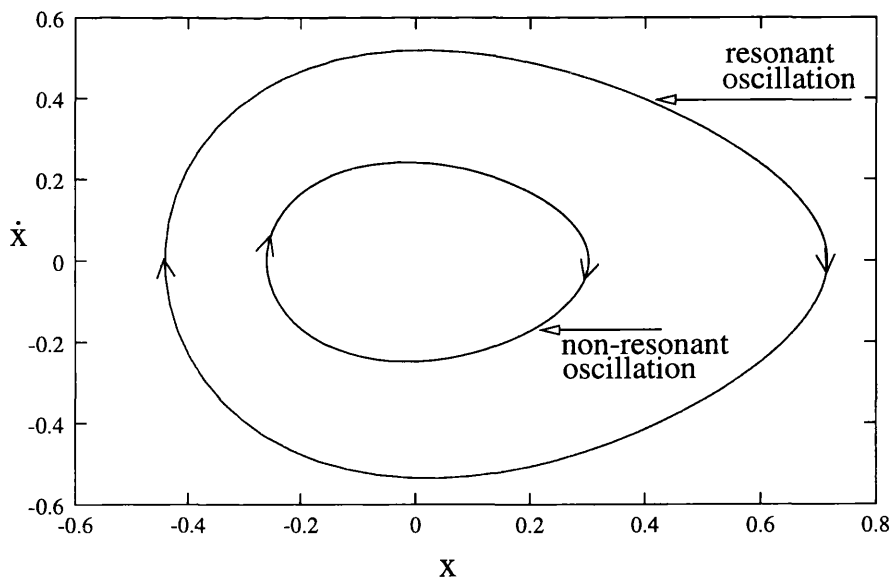

Figure 3.3: Numerically integrated orbits for the case where two main solutions exist. By main we refer to the fact that both have significant basins of attraction (see next section) and randomly chosen initial conditions are likely to settle onto these two steady states or escape. Here, $\omega = 0.85$ and $F = 0.06$.

another stable steady state, the oscillations will lead to capsize. For higher forcing frequencies, figure 3.1(a), the system will escape from fold A. As ω is decreased fold A shifts to lower F values than the flip, figure 3.1(b). In this case a stable $n = 1$ steady state exists when the system jumps from fold A and the system may now 'jump' to the resonant solution. This will occur providing the trajectory is in the basin of attraction of the resonant solution at the point of bifurcation. As we shall see, this can become unclear when the basin boundaries become fractal (see chapter 4, section 4.3.2 and Thompson (1992)).

Note that stable solutions other than those shown here exist but are usually ignored since they have very small basins of attraction (i.e. few initial conditions $(x_0, \dot{x}_0)$ will settle onto such steady states). The system is thus highly unlikely to jump onto any of these solutions and even should this happen would be quickly 'knocked off' by any perturbing influence. For the real system with irregular waves and the presence of noise, these 'rogue' solutions are extremely unlikely to be observable. Unstable solutions can however play an important role, e.g. the escape from chaos bifurcation is actually due to the collision between the stable chaotic steady state and an unstable period 6 solution (Thompson 1989).

In chapter 8 we plot experimentally derived phase portraits of resonant and non-resonant solutions which show the same qualitative behaviour exhibited here.

3.2.2 Bifurcations in parameter space

Following our study of the physically realistic limits to the single degree of freedom beam sea roll model in chapter 2, we now extend the bifurcation diagrams of Thompson, Bishop & Leung (1987) to higher frequency regimes. Here we have used limits of $J^{max} = 3$ and $\omega^{max} = 2.1$ (Cotton & Spyrou 1997). These limits

don't lead to escape, see section 3.3

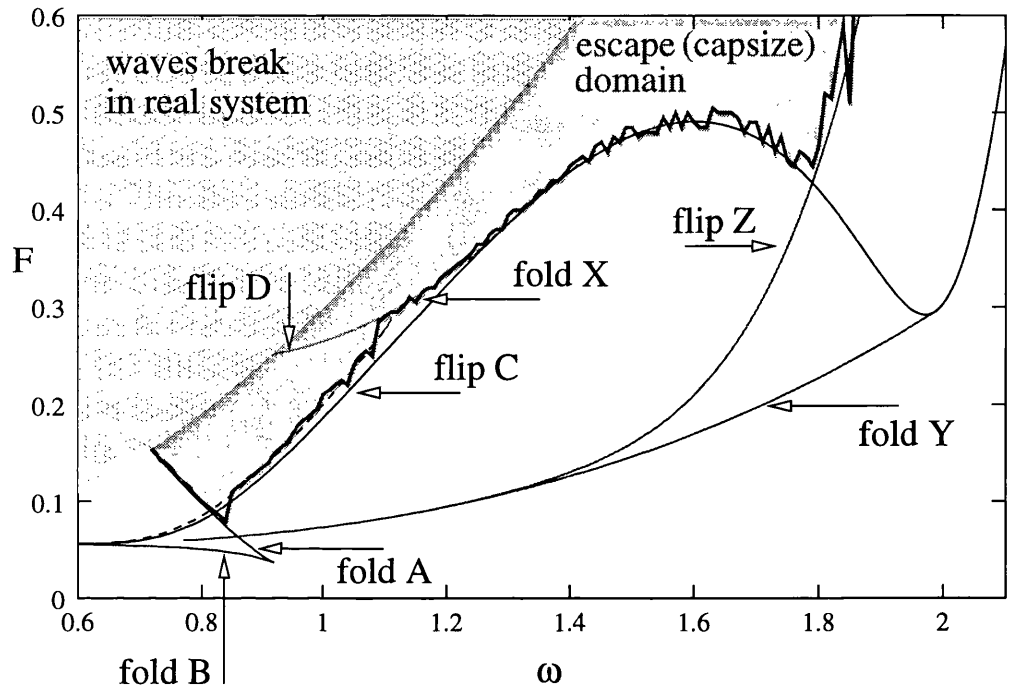

Figure 3.4: Bifurcation arcs in (ω, F) control space for the escape for the cubic potential well (quadratic restoring). Superimposed is a numerically determined steady state escape boundary. The region for which real waves would break (taking $\theta_V = 90$) is hatched. Note that the truncation of the Y and Z arcs at lower frequencies is due to ill-conditioning in the numerical algorithms used to locate these lines.

are, of course, dependent on dimensional parameters describing the real ship, so we have chosen a sensibly large range.

In figure 3.4, we show the key steady state bifurcations along with a numerically generated escape boundary. The steady state escape boundary is the point at which escape from the potential well occurs if forcing is slowly wound up from zero, with the system being allowed to settle onto a steady state before each small increase in F. We can see how the bifurcation arcs determine the locus of steady state escape. Note that on this plot the worst case resonant region at $\omega \approx 0.85$ is the dominant feature. The hatched area shows the region where real waves would break, within which we must be careful when using this simple model. To

determine this we have used the relationship of equation (2.5),

$$F = \frac{Ak\omega^2}{\theta_V}$$

with maximum wave slope, $Ak = \pi/7$. We have chosen $\theta_V = 90°$, thus imposing a reasonably tough limit.

The schematic diagram of figure 3.1 can be deduced by following steady state paths vertically on figures 3.4. In figure 3.5(a)-(e), schematic diagrams, similar to those of figure 3.1 are drawn . These paths can be deduced from the bifurcation diagrams but are shown here for clarity.

In figure 3.6 the bifurcation arcs and escape locus are again plotted, but here with the scaled wave slope $J = F/\beta\omega^2$ on the y-axis. This tends to emphasise the importance of the second resonance region centred on $\omega \approx 1.8$. We see here how the choice of a nondimensional wave slope rather than F has highlighted a significant feature that might otherwise be missed. The worst case capsize point in this second resonance region is almost as low as that at resonance and this certainly seems a phenomenon worthy of further attention. Interestingly we see that the flips C and Z define a capsize boundary in a similar way to the resonant boundary, which is defined by the fold A and flip C. Note that the simple design formula predicts escape to occur above $J = 1$.

These bifurcation arcs have all been located using numerical continuation algorithms. These provide a fast and accurate way of locating bifurcations in control space. However one can also plot bifurcation arcs with reasonable accuracy using harmonic balance and variational methods, (Virgin 1988; Szemplinska-Stupnicka 1992). Whilst for the purpose of analysing the dynamics there is little advantage in using approximate analytic techniques, they may be of use from a design perspective since it is possible to write capsize boundaries as explicit functions of ship

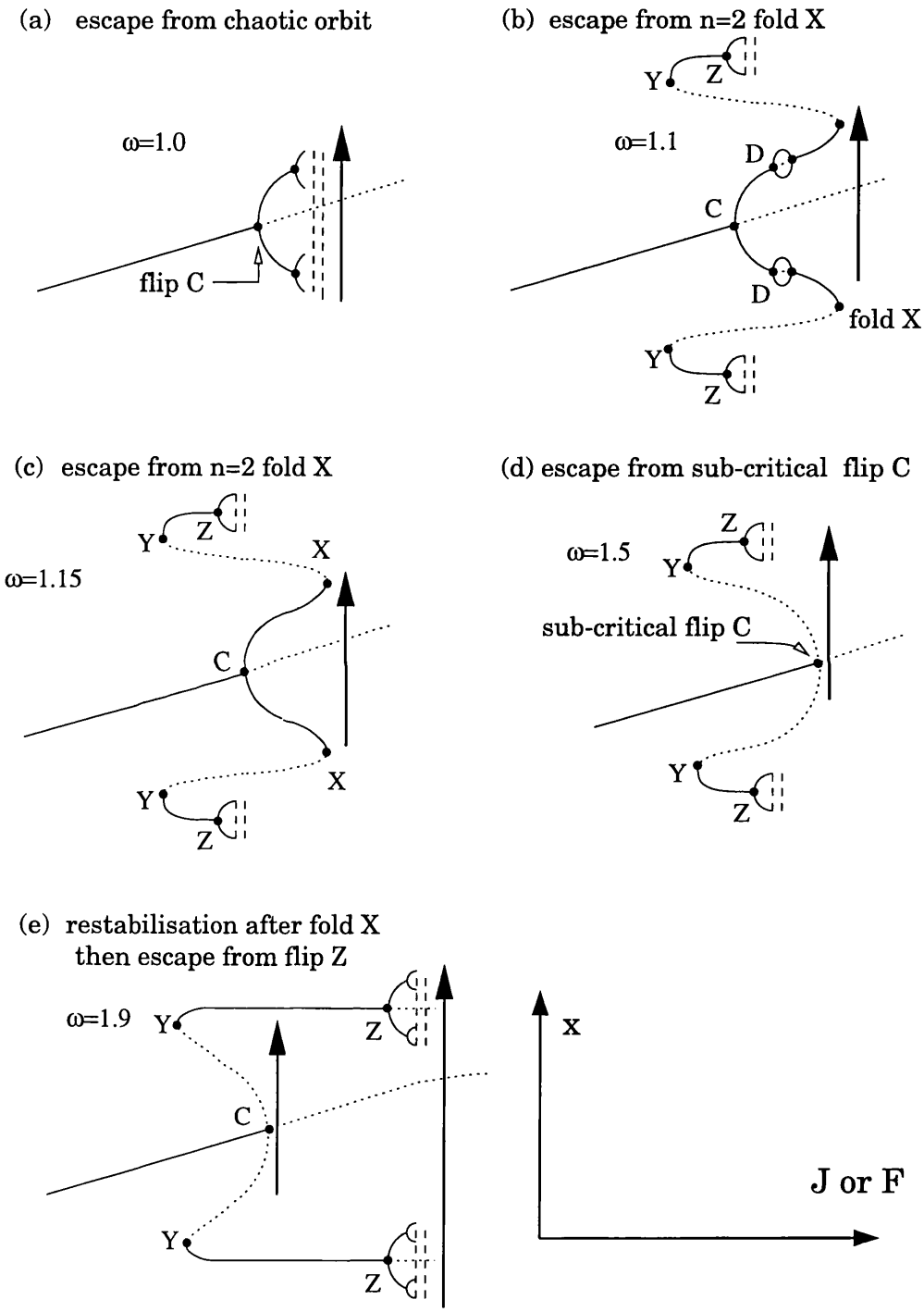

Figure 3.5: A series of schematic diagrams showing the evolution of the steady state solution paths as forcing amplitude is increased at constant frequency. The possible mechanisms for escape are indicated by large arrows and the bifurcation points by filled circles.

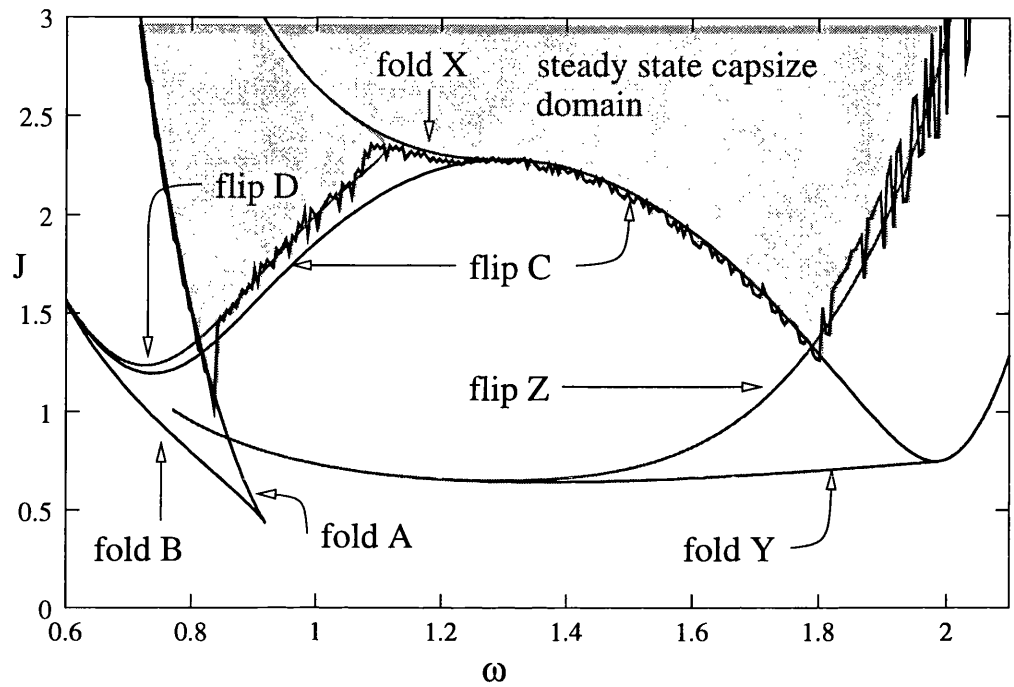

Figure 3.6: Bifurcation arcs in (ω, J) control space for the escape for the cubic potential well, or $\alpha = 0$ restoring. When the scaled wave slope is used the significance of the second resonance region is clearer.

parameters.

3.3 Transient escape and basin erosion

While the stability of steady state solutions can tell us a lot about the dynamics of the system in question, the modelling of ship capsize also requires an understanding of how transient motions can lead to escape from the well. Clearly capsize can still occur when a stable steady state exists and we are interested in predicting the likelihood of this outcome. To this end we use the concept of safe basins of attraction (Foale & Thompson 1991; Soliman & Thompson 1989) as part of an integrity measure that encapsulates the essentially transient nature of capsize in the real world.

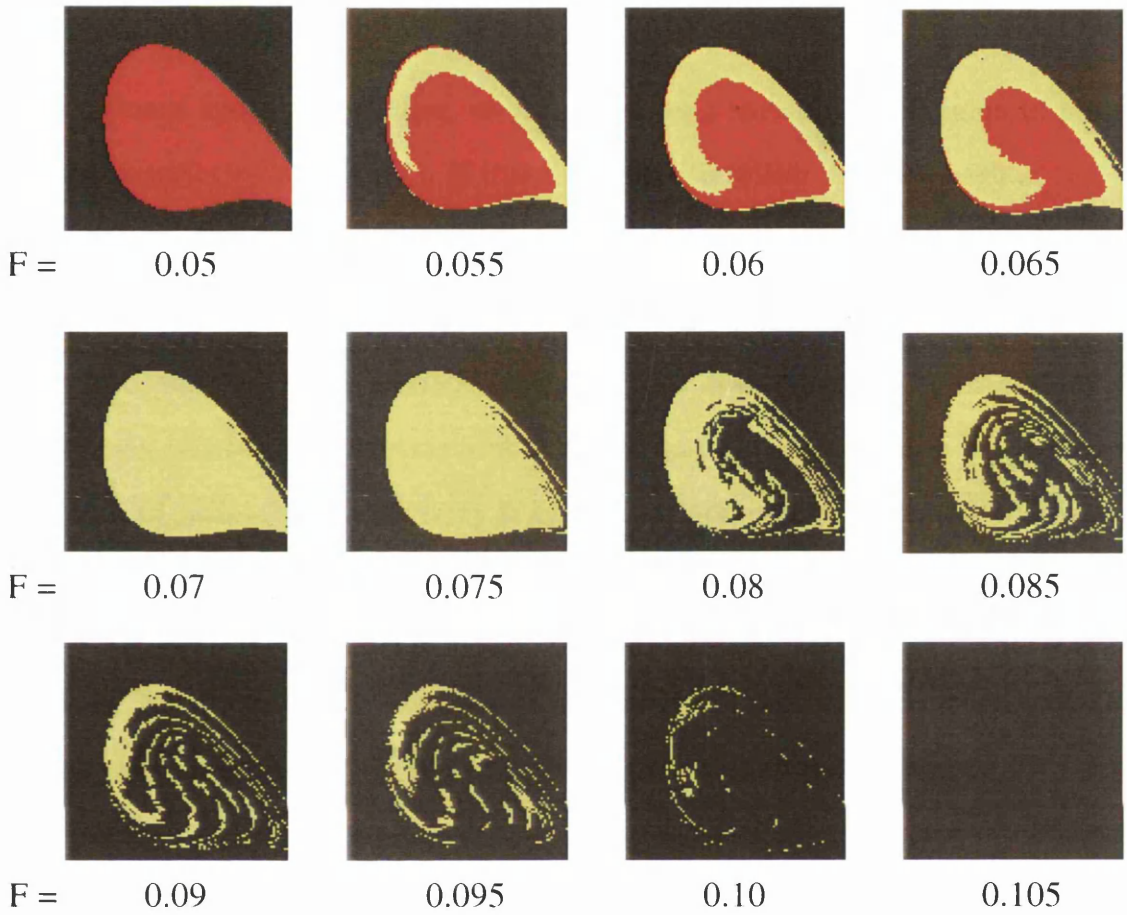

Figure 3.7: Basin erosion the quadratic escape equation, for with $\beta = 0.1$ and $\omega = 0.85$, for various values of forcing amplitude, F, underneath each diagram. Each cellmap shows the basins of attraction in $(x, \dot{x})$ space, with $(0, 0)$ in the centre. In the first figure the single basin of attraction for the period one solution can be seen in red. As F increases, the yellow basin of the resonant solution appears (at the fold B). Shortly after $F = 0.065$, only the basin of attraction for the resonant solution can be seen. For a small further increase in F we see the sudden erosion of the resonant solution. In the final figure the basin has been completely eroded.

3.3.1 Basins of attraction

The safe basin of attraction is the domain of initial conditions in phase space which do not lead to escape from the well as the system evolves in time, (Soliman & Thompson 1989; Foale & Thompson 1991). For a single degree of freedom forced oscillator this phase space is 3-dimensional (Guckenheimer & Holmes 1983). However, since our forcing is sinusoidal we can reduce this by considering a Poincaré section of the space. We thus obtain a 2-dimensional phase space and a 2-D

Poincaré map. We are then interested in the size of the safe basin of attraction in this reduced space. In practice, we only consider a suitably large region of phase space, monitoring the fraction of this region that is within the safe basin.

Using the cellmapping algorithms of Hsu (1987) one can numerically determine basin size with reasonable efficiency, and studies of this kind (Thompson 1989; Lansbury & Thompson 1990) have shown that erosion of the basin can occur extremely quickly with variation of a forcing parameter. In figure 3.7 we show a series of cellmaps for the $\alpha = 0$ system. Black represents initial conditions that escape from the well. The safe basin is therefore composed of the shaded areas, different shadings being initial conditions that lead to different final steady states. We can see that erosion occurs rapidly after the initial incursion. This has significant implications for the prediction of transient escape which we discuss in further detail below.

Known as the 'Dover Cliff' (Soliman & Thompson 1991; Soliman & Thompson 1992), this sudden erosion is associated with saddle connection events (Lansbury, Thompson & Stewart 1992) and we can use this to predict the boundaries in parameter space at which it occurs. A homoclinic saddle connection occurs when the inset of a saddle point intersects with the outset of the same point[3]. When the insets and outsets belong to different saddles, then we have a heteroclinic connection. The state at which the saddle inset and outset are tangent is referred to as a homoclinic or heteroclinic tangency. It is this event that can signal the onset of basin erosion.

[3]The saddle orbit is reduced to a point when we consider a Poincaré section

3.3.2 Transient capsize diagrams

A consideration highlighted by Odabasi (1982) was that in general for nonlinear systems with multiple solutions one needs to consider all possible initial conditions. However, in this case, the rapid erosion of the safe basin at the Dover Cliff allows us to reduce the problem of determining a boundary for transient capsize in control space. Rather than studying a large number of possible initial conditions, the fact that most of the safe basin is eroded for a small parameter change implies that we can merely consider one and look for the parameter values at which one starting condition leads to escape. The effectiveness of this approach has been demonstrated by Thompson & Soliman (1990) and Bishop & de Souza (1993).

In figure 3.8 a transient capsize diagram for the quadratic escape equation is shown, with the steady state bifurcations superimposed. The shaded areas represent parameter values for which the initial condition of $(x = 0, \dot{x} = 0)$ leads to capsize (or escape from the well). The shading is darker the faster the trajectory reaches the assigned escape boundary (in this case, oscillations greater than $x = 1.2$). We can see how capsize occurs even where steady state solutions are available (see figure 3.6 for comparison). Although we only tested one initial condition for each parameter setting, the rapid basin erosion shown in figure 3.7 means that the diagram would look much the same for any choice within the zero forcing safe basin of attraction. Importantly we can also see how the steady state bifurcations give a poor estimate for the capsize boundary since they only indicate where no safe steady state exists. It is also interesting to note the effectiveness of the simple design formula, detailed in chapter 2, $J = Ak/2\zeta\theta_V = 1$ (chapter 2). This formula, although based on a simple linear model, proves a good lower bound for transient capsize.

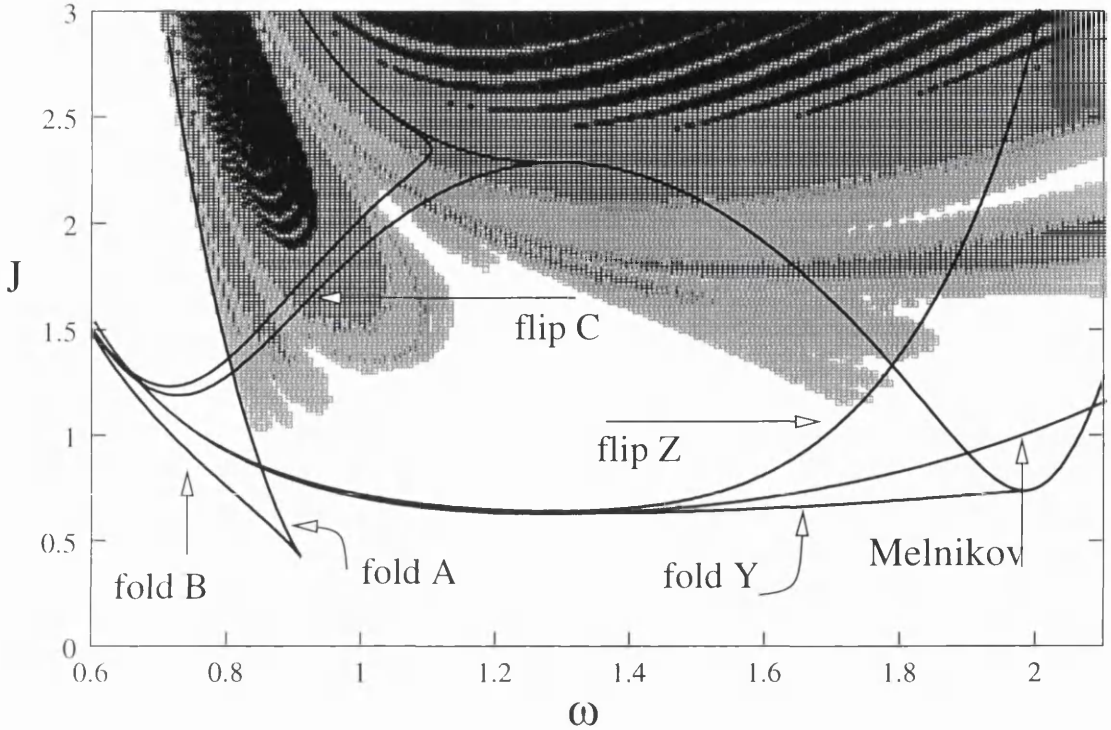

Figure 3.8: Transient capsize diagram for quadratic restoring, $\alpha = 0$. The shading represents the number of cycles before the escape criteria was breached; black is less than 4, dark hatching is 4-7 and light hatching is 8 or more. Superimposed are the steady state bifurcations from figure 3.6. Also shown is the Melnikov boundary, which merges with the fold Y and flip Z at lower frequencies.

3.3.3 Locating transient capsize boundaries using Melnikov's Method

Melnikov's Method for the approximate location of saddle connections provides us with a way of estimating the transient capsize boundary, see figure 3.8 (Bikdash, Balachandran & Nayfeh 1994; Thompson 1997). By approximating the saddle connection orbit, this method allows us to determine where a homoclinic or heteroclinic tangency occurs. The key advantage of this analytical approach is that it takes into account the nonlinear nature of the problem. The method is based on considering saddle connections in the relevant Hamiltonian system, and then perturbing in forcing and damping. It can, in this case, be most simply understood as an energy balance approach. Essentially we balance the energy lost through

damping with that gained from forcing around the saddle connection orbit in the Hamiltonian system.

For the quadratic escape equation, we firstly rewrite (2.8),

$$\ddot{x} + x - x^2 = \epsilon \left[\overline{F} \sin \omega t - \overline{\beta}\dot{x}\right] \tag{3.1}$$

where $\epsilon\overline{F} = F$ and $\epsilon\overline{\beta} = \beta$. For $\epsilon = 0$ the homoclinic connection from the only saddle at $x = 1$ is,

$$x(t) = 1 - \frac{3}{1 + \cosh t} \tag{3.2}$$

By balancing energy gained through forcing with that lost through damping around this orbit we can derive the Melnikov expression (Thompson, Bishop & Leung 1987),

$$F^M = \beta \sinh \pi\omega / 5\pi\omega^2 \tag{3.3}$$

$$\Longrightarrow J^M = \sinh \pi\omega / 5\pi\omega^4 \tag{3.4}$$

where the parameters are as for (3.1). This function is plotted in figure 3.8.

The solution of the integrals in the energy balance is generally a nontrivial procedure (see appendix A.1.1 for a more general solution of the above problem) and this is one of the chief obstacles to the use of Melnikov's method for predicting basin erosion. However, a number of these integrals have already been solved for various low order polynomial restoring functions, (Nayfeh & Balachandran 1995; Scolan 1997).

Reassuringly we find that this approach, which encapsulates the nonlinear nature of the restoring function, supports the setting of $\mu = 1$ in the simple design formula

of chapter 2. If we choose the worst case frequency $\omega \approx 0.8$ we find that,

$$J^M(0.8) \approx 1 \tag{3.5}$$

$$\Longrightarrow \mu \approx 1 \tag{3.6}$$

and hence we find from (2.22) that critical wave slope, $Ak \approx 2\zeta\theta_V$.

The similarity between Melnikov and the SDF is, perhaps, unsurprising, since the SDF with $\mu = 1$ can be thought of as a crude approach to modelling saddle connections. Rather than using the solution to the Hamiltonian system, the SDF uses a harmonic solution, also passing through the saddle point.

Some further issues associated with using saddle connections to identify erosion of the safe basin are discussed in chapter 5, in which the Melnikov Method for approximately locating such events is described in more detail.

Chapter 4

SYMMETRY BREAKING

4.1 Introduction

In chapter 3 we discussed the robust nature of nonlinear oscillators to perturbations in the damping or restoring functions. This is an important requirement if we wish to use these models for design purposes. However, the dynamics can be sensitive to certain important features. For instance, a hardening system will have a frequency response curve skewed the opposite way to that of a softening system, even though the restoring functions may be close throughout the range of interest. Symmetry in the equations of motion can also have a significant effect on the dynamics. In this chapter we explore the significance of symmetry for the steady state dynamics.

For a real system such as a loaded ship in wind, we can never expect the restoring to be perfectly symmetric. In fact, for a typical ship, we can expect a static heel angle of a few degrees. The use of symmetric models for ship roll thus seems unrealistic and this is compounded when one considers the results of MacMaster & Thompson (1994) who observed a sensitive dependence of worst case capsize on symmetry in the restoring force and Thompson (1997), in which sensitivity

was observed over a range of frequencies. We now extend this work, studying the different aspects of this sensitivity and associating it with particular bifurcations.

4.1.1 The effect of a loading bias

A loading bias for a ship may have many causes; wind, cargo shift or damage being perhaps the more typical. We are interested in modelling a generic bias and we therefore use a family of restoring functions that allows us to introduce bias by varying just one parameter. This approach is similar to that used in other studies but rather than adding a bias term (Kan & Taguchi 1991; Nayfeh & Sanchez 1990) we use a family of restoring functions that vary smoothly between the cubic and quadratic models. The advantage of this is that we keep a zero in restoring at $x = 1$. This allows us to study the significance of changes in the shape of the potential separately from the effect of reduced angle of vanishing stability.

In chapter 2 we described the α parameterised escape equation, introduced by MacMaster & Thompson (1994) to model the effects of bias in the restoring force. From the formulation of the nondimensional equations of motion, we can use the relationship of equation (2.6) to write the capsizing wave slope as

$$\text{capsizing } Ak = \left(\theta_V/\omega^2\right) \times f(\alpha, \beta, \omega) \tag{4.1}$$

where the unknown function of the system parameters, f, can be found numerically (MacMaster & Thompson 1994).

Using this result we find that the sustainable wave slope, Ak, is reduced by a loading bias in two ways;

(a) arises from the fact that the effective angles of vanishing stability will become $\theta_V \approx \theta_{V0} - \theta_H$, $\theta_U \approx \theta_{V0} + \theta_H$: the θ_V appearing explicitly in the result will

thus decrease Ak linearly with θ_H.

(b) arises from the fact that the shape coefficient, α, will be changed from 1 to $\alpha = \theta_V/\theta_U$, thus altering the function $f(\alpha, \beta, \omega)$. It is the subtle effects of this change in potential shape that we are primarily interested in here.

As we are working in the nondimensional equations, for which the nondimensional angle of vanishing stability remains equal to 1, we will generally observe only effect **(b)**.

4.2 Sensitivity over a range of frequencies

To investigate symmetry breaking we use the nondimensional model for roll motion with α parameterised restoring and linear damping,

$$\ddot{x} + \beta\dot{x} + x(1-x)(1+\alpha x) = F \sin \omega t \tag{4.2}$$

so that the restoring always equals zero for $x = 1$. We are therefore modelling capsize in biased ships as escape from the potential wells of figure 2.2. The reduction in θ_V with heeling due to wind loading is incorporated into the equation of motion. Since we are primarily interested in the effects of symmetry breaking on sustainable wave slope (the minimum Ak that causes capsize), we again utilise the nondimensional wave slope J, in addition to F. As has been previously noted, the use of J tends to highlight behaviour relevant for capsize.

4.2.1 Steady state escape algorithm

To find the capsizing J, forcing amplitude is slowly increased from zero at constant ω until an escape criteria is breached. A simple $|x| > 1.2$ criteria was used to de-

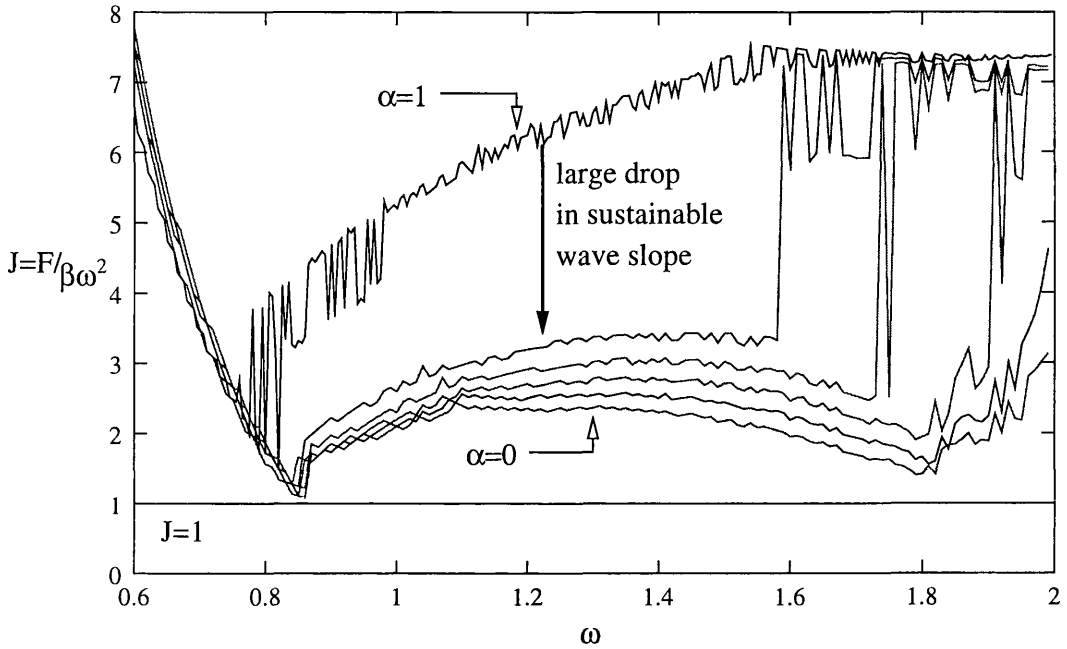

Figure 4.1: Here α is varied from 0 to 1 in steps of 0.2. The drop in capsizing J due to a symmetry breaking bias occurs between frequencies $\omega \approx 0.84$ and $\omega \approx 1.8$.

fine escape. This is quite a strict test since, typically, once an oscillation becomes greater than approximately $x = 0.7$ escape to infinity occurs. Further approximations are required to specify when steady state conditions have been reached. We allow 16 forcing cycles before steady state is assumed to have been reached and J incremented by ΔJ. Reassuringly, small variation of the cycles allowed for steady state and the step size in J proves to have little effect on the results. The forcing amplitude at which escape occured is recorded, a new frequency is then chosen and the process begun again.

4.2.2 Steady state capsize

Figure 4.1 shows the capsize boundaries for α varied in steps of 0.2 between 0 and 1. Note also that we have extended the diagram to unrealistically high J values to demonstrate the dramatic effect of the loss of symmetry in restoring. For symmetric restoring we can see that the capsizing domain is mostly above the

$J = 3$ line at which a wave will typically break (recall that the maximum J is determined by θ_V and damping as well as actual wave slope). For the biased cases this is certainly not the case. Also plotted on this diagram is the predicted escape boundary using the simple design formula detailed in chapter 2; $J = Ak/2\zeta\theta_V = 1$. The effectiveness of this formula is evident and we discuss how it may be extended to nonlinearly damped systems in chapter 6.

Escape in the resonance region can now be roughly divided into 2 areas;

1 the low frequency regime where loss of symmetry has little effect on J,

2 mid-range frequencies where loss of symmetry leads to a significant reduction of the J, or capsizing wave slope. The J lines are irregular in this region, but still show trend behaviour,

To illustrate the significance of these results we can use equation (2.2) to transform the information from the escape diagram into a more physically meaningful form. In the more sensitive frequency region of figure 4.1, J is roughly halved when α is reduced from 1 to 0.9. We also find from equation (2.2) that $\alpha = 0.9 \Rightarrow \theta_H/\theta_{V0} \approx 0.05$. Hence we have a halving of the sustainable wave slope when the heel angle is roughly 5% of the unbiased angle of vanishing stability, θ_{V0}. Note that for heel angles of this size, the effect of the stability drop due to reduced θ_V is negligible when compared to the extreme symmetry breaking effect. Returning to our breaking wave limit of about $J = 3$ we find, for a ship with $\theta_V = 50°$, that over a large range of wave periods a heel angle of only 2° could easily make the difference between capsize or no capsize, under regular seas.

4.2.3 Sensitivity analysis

We can focus on the sensitivity to α by plotting the capsize boundaries as a function of α, figure 4.2. At a frequency of $\omega = 0.7$, the effect of varying α is small. In the studies of MacMaster & Thompson (1994) the worst case capsize point was found to be sensitive to α, and we can see this verified in figure 4.2. It can be seen that the worst case capsize point shows a 20% drop as α is reduced from 1 to 0. However, the sensitivity of the higher frequency region is far more dramatic, with a drop of more than 60% being observed at the example frequencies of $\omega = 1.0$ and $\omega = 1.4$. Moreover, most of this drop takes place when α is reduced only a small amount from 1. It is this region that has perhaps the more serious implications for ship capsize.

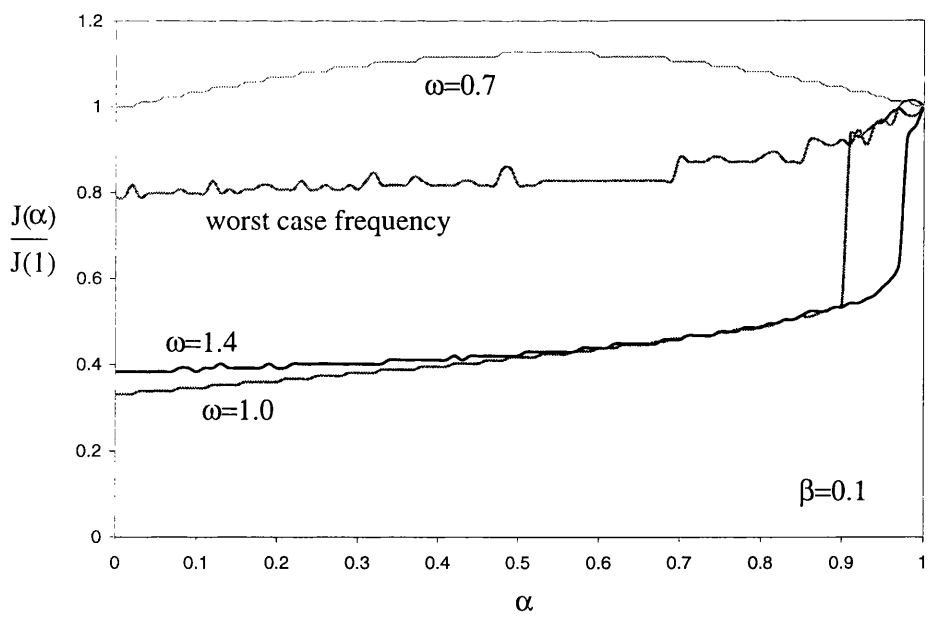

Figure 4.2: Dependence of relative capsize boundary, $J(\alpha)/J(1)$ on α near resonant frequencies. Also plotted is the worst case capsize point which is much less sensitive to bias. This measure of sensitivity only captures the effect **(b)**.

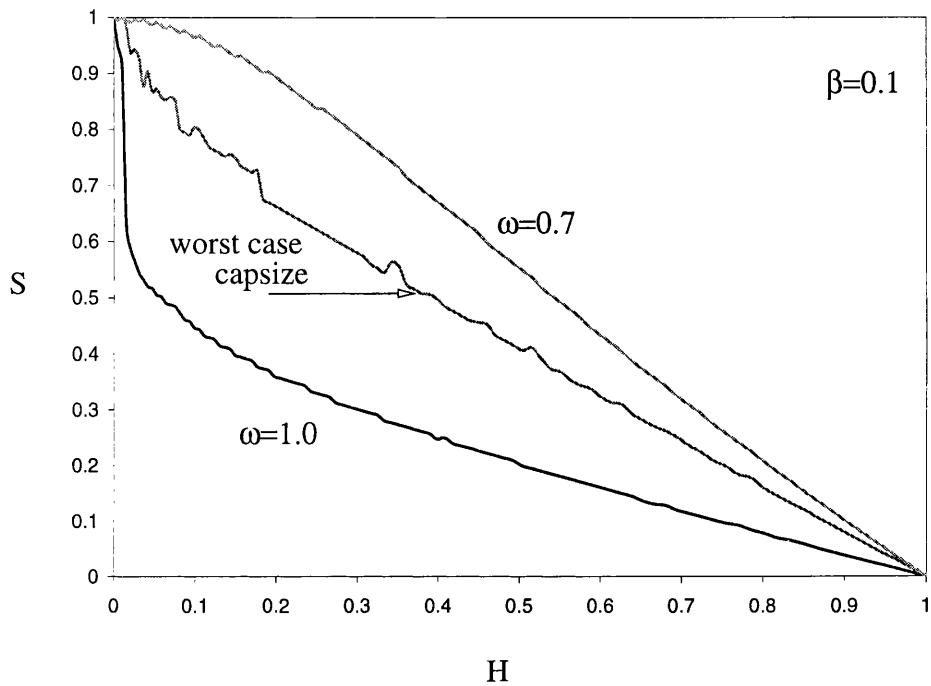

Figure 4.3: Dependence of S on α in the main sensitive region. Also plotted is the worst case capsize point which is much less sensitive to bias. Using S enables us to incorporate effect (a), reduction of θ_V as heel is increased, thus demonstrating the overall effect of the biasing.

Relative sustainable wave slope

In order to study effects **(a)** and **(b)** together, we use a relative sustainable wave slope,

$$\begin{aligned} S &= (Ak \text{ with loading bias})/(Ak \text{ without loading bias}) \\ &= \frac{J(\alpha)\theta_V}{J(1)\theta_{V0}} \end{aligned} \tag{4.3}$$

which we can use with equation (2.2) to give S as a function of $H = \theta_H/\theta_{V0}$.

In figure 4.3 we plot S against H for the three main cases. The incorporation of the reduction in θ_V (effect **(a)**) can be seen in the linear relationship at higher H

(recall that $Ak \propto \theta_V$) where effect **(b)** is less.

We can now compare this study to that of Thompson (1997) for which a diagram similar to that of figure 4.3 is plotted, for a damping level of $\beta = 0.2$. These results show much the same sensitive behaviour for the worst case frequency. However, the sensitivity for forcing frequencies higher than worst case, as shown for $\omega = 1.0$, is extreme once the reduction in θ_V is included.

4.3 Bifurcational sensitivity to bias

The positions of the fold and flip bifurcations have been shown to be vital in determining the parameter values at which steady state escape occurs (see chapter 3). A useful next step is to extend the path-following methods to generate these bifurcation lines in the 2-dimensional control space spanned by F and ω and compare them to our capsize boundaries.

The bifurcation arcs around resonant frequencies are shown in figure 4.4 with the relevant capsize boundaries superimposed. More details of this method may be found in (Foale & Thompson 1991). It was found that the flip and escape lines stayed close throughout the region of interest, supporting the use of the flip as a close approximation to the point of escape from chaos.

4.3.1 The symmetry breaking bifurcation

Following previous studies (outlined in chapter 3) we can now describe the steady state solutions and how escape might occur as forcing amplitude is slowly increased. Escape in the symmetric system, $\alpha = 1$, figure 4.5, is similar to that of the biased system, with the important addition of a symmetry breaking bifurcation. The symmetric $n = 1$ solution loses stability at the pitchfork bifurcation, where two

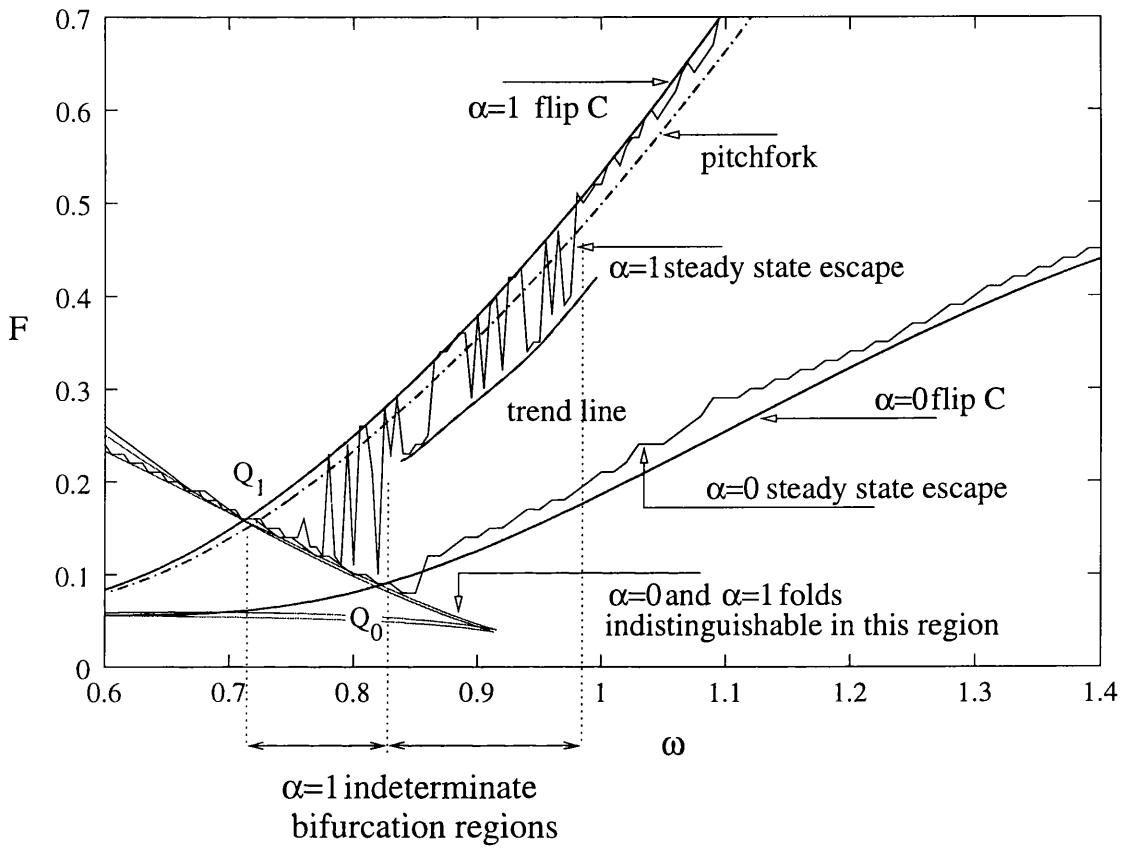

Figure 4.4: A bifurcation diagram for $\alpha = 1$ and $\alpha = 0$, showing the large difference in the flip lines and similar fold lines. The capsizing J lines for each system are superimposed. We refer to the points where the flips cross the fold line as $Q_{0,1}$.

unsymmetric, stable solutions branch off, losing stability after only a small further increase in F, at the flip bifurcation C. By 'symmetric' we refer to the fact that a negation of the coordinates, so that $(x, \dot{x}) \to (-x, -\dot{x})$, leaves us on the same trajectory in phase space.

For $\alpha < 1$ the pitchfork is replaced by a fold bifurcation. The flip bifurcation that is taken as an approximation of capsize falls back to lower forcing amplitudes for $\alpha = 0$.

As discussed in chapter 3, the significance of the fold and flip bifurcation lines in determining steady state escape is evident from figure 4.4. The bifurcation lines effectively mark escape for both systems over a range of frequencies. We can now

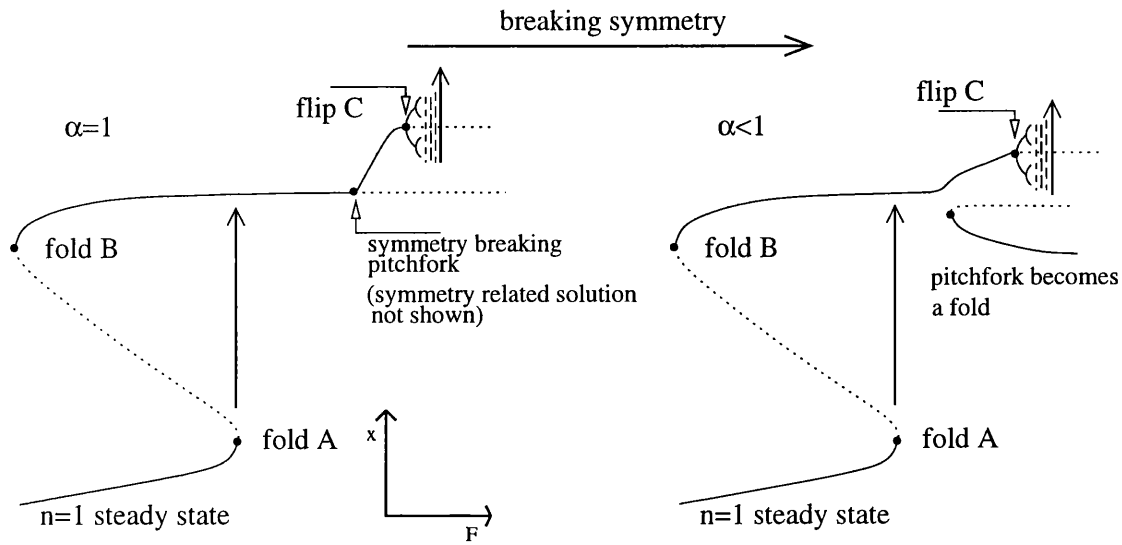

Figure 4.5: Schematic diagram showing solution paths in the frequency region where escape occurs from chaos. As symmetry is broken the pitchfork bifurcation becomes a fold. Escape occurs from the fold A or at the final crisis after the period doubling cascade to chaos.

identify the flip C, with the sensitivity to symmetry breaking bias seen in region **2** of figure 4.1. It is the change in the flip arc with α that lies behind the sensitivity seen in this region.

The flip sensitivity can be explained roughly in terms of the expected significance of the symmetry breaking for solutions of different oscillation amplitudes. From figure 2.2 we can see that the effect of symmetry breaking is greater away from the bottom of the well. Hence, it is sensible to expect oscillations of higher amplitudes (e.g. near to the flip) to be the most affected by variation of α.

4.3.2 Indeterminacy and worst case capsize

The escape boundary is irregular throughout the frequency range, particularly around the region showing the sensitivity to bias. We associate this irregularity with two basic features of the dynamics; long chaotic transients and indeterminate bifurcations (Thompson 1992).

Escape via the period doubling cascade occurs from a chaotic orbit and associated with this are very long transient motions. Hence it is likely that our algorithm assumes a steady state too quickly in such regions. If the steady state solution is not followed sufficiently closely then the initial conditions may lead to escape, thus recording the escape boundary erroneously. It is possible that this problem may be reduced or eliminated by more stringent escape and steady state conditions. However, even then, rigorous criteria cannot be defined for the long transient motion associated with a chaotic orbit.

Indeterminacy occurs where the system escapes from two trend lines at arbitrarily close frequencies, see figure 4.4. This occurs when the steady state bifurcates when it lies on a fractal basin boundary (Soliman & Thompson 1991). The escape boundary shows significant indeterminate regions between two trend lines for ω around worst case escape - the two regions are identified on the diagram. More important is the indeterminacy - for forcing frequencies lower than the flip/fold crossing point (Q_0 and Q_1) the steady state will escape from the fold A as F is increased. In the first indeterminate region at higher ω the system can either 'jump' to resonance and then escape from chaos (shortly after the flip bifurcation) or escape directly from the fold bifurcation. For the symmetric system in particular there is a significant region of indeterminacy. The cause of this behaviour is the heteroclinic tangle between the unstable resonant saddle and the hill-top saddle, see figure 3.1 . It is this feature that leads to the fractal basin boundary and determines the worst case escape point. Occurring at lower oscillation amplitudes, it is perhaps unsurprising that the boundary of the heteroclinic tangle and hence the worst case escape point is less sensitive to bias.

Further indeterminacy has been noted for $0.84 < \omega < 0.98$ for $\alpha = 1$ and also at higher frequencies around $\omega \approx 1.7$ for $\alpha < 1$, see figure 4.1. Without a careful study of the steady state solutions in these regions of parameter space it is difficult

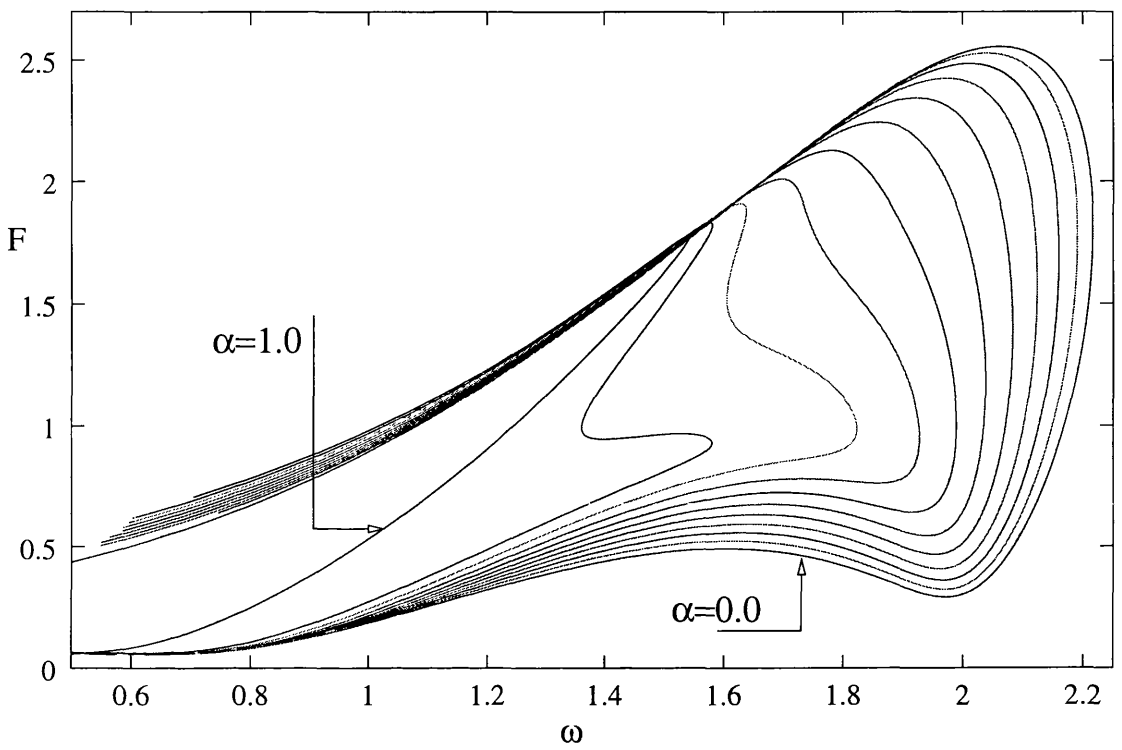

Figure 4.6: The flip bifurcations as α is varied between 0 and 1 in steps of 0.1. We can see how the sensitivity to symmetry originates in the S shape which moves swiftly to lower frequencies as α approaches 1. The termination of the flip arcs at low ω is due to the failure of the bifurcation following algorithm (due to ill-conditioning) at lower frequencies.

to differentiate between indeterminacy and a failure in the algorithm due to long transient motions associated with the chaotic behaviour close to the flip. However, the presence of a trend line, as indicated in figure 4.4, suggests the presence of an indeterminate bifurcation.

4.3.3 The flip bifurcation

Having identified the main features of the escape diagram in terms of the bifurcation lines and indeterminacy, the sensitivity in the second frequency region is now considered further. The flip arcs for a series of α values are plotted in figure 4.6.

Focussing firstly on the resonant frequency region the high sensitivity of the flip

line to symmetry breaking is evident in figure 4.6. The flip falls steeply back towards the $\alpha = 0$ line as α is reduced from unity. We can see how the global structure of the flip bifurcation leads to the sensitivity close to resonance. The S-shape moves swiftly to low frequencies as α approaches 1. At a fixed frequency, this has the effect of moving the flip to higher F values, for only a small change in α.

4.3.4 The pitchfork bifurcation

As before (see chapter 3), we can use Poincaré maps to follow steady state solutions of the equation of motion. We can also follow the stability of orbits in the flow by considering stability in the map (Thompson & Stewart 1986; Guckenheimer & Holmes 1983). In figure 4.4 we can see that, as F is increased, the pitchfork bifurcation occurs before the flip (which leads to escape). We now describe why the symmetric period one orbit cannot undergo a period doubling bifurcation.

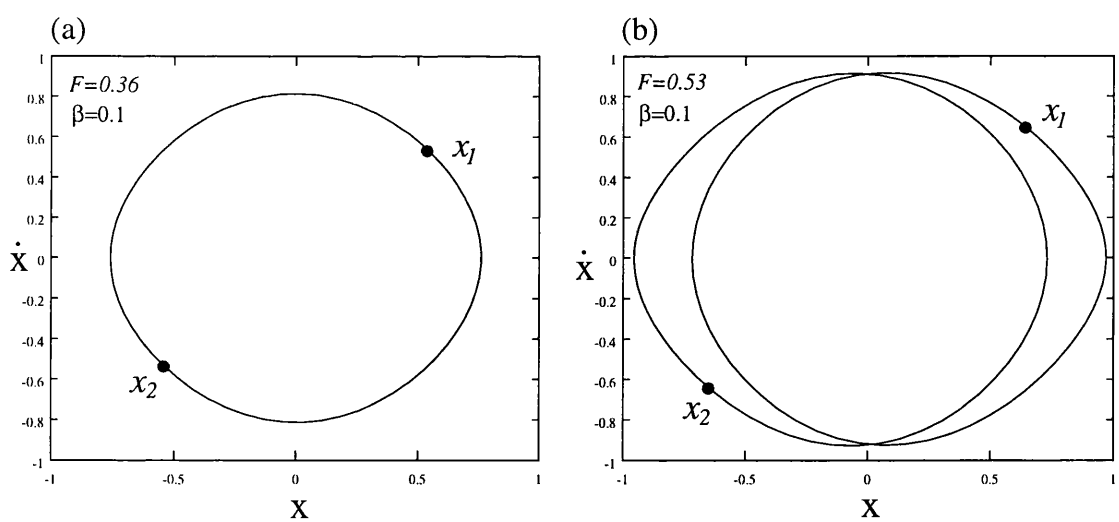

Figure 4.7: Orbits before and after the symmetry breaking bifurcation for the symmetric restoring system. Both are shown for $\omega = 1.0$ and the two asymmetric orbits are very close to escaping. Note how the symmetry related points x_1 and x_2 are on the same orbit in (a) and symmetry related orbits in (b).

Reduction of a symmetric oscillation to two half maps

When we are dealing with a symmetric system (by which we refer to symmetry in the potential and damping), it is possible to consider orbits that may be further reduced to two half maps. Taking a solution for equation (2.9) to be $(x_1, \dot{x}_1)$ at $t = t_1$ and considering another solution $(x_2, \dot{x}_2)$ half a forcing period advanced in time,

$$\ddot{x}_1 + \beta\dot{x}_1 + x_1 - x_1^3 = F\sin(\omega t_1) \tag{4.4}$$

$$\ddot{x}_2 + \beta\dot{x}_2 + x_2 - x_2^3 = F\sin(\omega(t_1 + \pi)) = -F\sin(\omega t_1) \tag{4.5}$$

we can see that by choosing $x_2 = -x_1$ and $\dot{x}_2 = -\dot{x}_1$ the equations are equivalent and so the dynamics are the same. Hence $(x_2, \dot{x}_2)$ is also a solution. We define a symmetric oscillation to be one where these two solutions are part of the same trajectory, see figure 4.7.

So, for a symmetric oscillation, we can think of the orbit as being composed of two dynamically identical parts and can therefore write the time T map, P, in the following way,

$$P(\underline{x}) = Q(\underline{x}) \circ Q(\underline{x}) = Q(Q(\underline{x})) \tag{4.6}$$

where Q is the time T/2 map and $\underline{x} = (x, \dot{x})$. Differentiating this gives,

$$DP(\underline{x}) = DQ(Q(\underline{x}))DQ(\underline{x}) \tag{4.7}$$

where $DQ(\underline{x})$ is the Jacobian of $Q(\underline{x})$, differentiated with respect to $\underline{x}$. Now $Q(\underline{x})$ is dynamically identical to $\underline{x}$ (since we have a symmetric system). We can therefore

write,

$$DP(\underline{x}) = DQ(\underline{x}) \circ DQ(\underline{x}) \tag{4.8}$$

where DQ is the Jacobian of the time T/2 map.

Hence if $\lambda_{1,2}^{DP}$ and $\lambda_{1,2}^{DQ}$ are the eigenvalues of DP and DQ respectively we know that,

$$\lambda_{1,2}^{DP} = (\lambda_{1,2}^{DQ})^2 \tag{4.9}$$

Implications for bifurcation sequences

Now, if a parameter is varied such that one of the eigenvalues of DP goes through the unit circle (in the complex plane) then the solution is said to have bifurcated. Constraints on the eigenvalues for these systems (Thompson & Stewart 1986) mean that this can happen in three ways:

1 one eigenvalue passes through the unit circle at 1, typically at a fold or pitchfork bifurcation

2 one eigenvalue passes through the unit circle at -1, typically at a flip bifurcation. This is represented as a period doubling in the full orbit

3 both eigenvalues pass through the unit circle with complex conjugate values. Typically this will be a Hopf bifurcation(Thompson 1996)

Now, since the eigenvalues of DP are the square of the eigenvalues of DQ, DP cannot have only one real and negative eigenvalue which lies outside the unit circle. Of course it is possible for the eigenvalues of DQ to be $\pm i$ - however this would mean that both eigenvalues of DP pass through -1. Hence a flip bifurcation

cannot occur. Consequently, the symmetric oscillation cannot undergo a period doubling bifurcation, and the pitchfork bifurcation must occur first.

This requirement for symmetry to be broken before the period doubling cascade can occur lies behind the shifting of the final crisis to higher forcing values.

4.4 Conclusions

In order to study the significance of bias in restoring for escape and hence capsize, we used a numerical algorithm to estimate the steady state capsize boundary over a wide range of forcing frequencies. Using the nondimensional wave slope J two main escape regions were identified, the higher frequency region of which showed extreme sensitivity to bias. The sensitivity was then examined in more detail and compared with the studies of MacMaster & Thompson (1994) and Thompson (1997). The worst case escape point identified in these previous studies is then shown to be less sensitive to bias than the higher frequency range.

We have also noted a number of regions of possible indeterminate bifurcations for the symmetric ($\alpha = 1$) system. These suggest the presence of further important steady state solutions and complicated basin structure that may be an interesting route for future studies to pursue.

In the second part of this chapter we have associated a particular escape mechanism with the observed sensitivity of escape to bias. Using the flip bifurcation as an estimate, the final crisis which occurs after a period doubling cascade is identified as the escape route for which bias has the most significance. We have argued that it is the high amplitude nature of escape via this mechanism that gives it its sensitivity to symmetry in restoring. Escape from the fold bifurcation, which occurs at a much lower amplitude, shows almost no dependence on symmetry.

Due to heteroclinic tangling (Thompson & McRobie 1993), worst case escape also occurs via the fold mechanism and is defined by the arc of the heteroclinic tangency. Since this heteroclinic tangency exists at low amplitudes, the worst case escape point is found to be less sensitive to symmetry.

This sensitivity has great significance for ship safety criteria and capsize testing, implying that small biasing from symmetry can lead to a sudden reduction in the wave slope necessary to cause capsize. Note that the biasing required is extremely small and in reality there will always be some bias in a ship due to design or cargo imbalance. Thus, the dramatic sensitivity seen here will not occur should loading be increased from a 'normal' state. However the sensitivity would be important in an idealised mathematical model that might be used in a design process. It is also an important consideration for any experimental capsize studies. We discuss this further in chapter 8 in which the effect of bias is noted in a series of roll and capsize tests.

A further conclusion is that these results support the use of the canonical escape ($\alpha = 0$) to be a sensible model of ship roll motion.

Chapter 5

MELNIKOV ANALYSIS

5.1 Introduction

As discussed in chapter 3, a saddle connection event can have dramatic effects on the global integrity of a system. In the case of oscillations within a potential well we may see the Dover Cliff phenomenon (Thompson 1997) where the set of safe (non-escaping) initial conditions is drastically reduced, for only a small change in a parameter. A homoclinic or heteroclinic connection can lead to the sudden erosion of the basin of attraction of a steady state solution. This greatly enhances the likelihood of transient motions escaping from the well and we are therefore interested in predicting such events. One important result is that we can use this behaviour to simplify our modelling of transient capsize. The fast erosion of the safe basin means that we need only consider one initial condition in order to determine a boundary for transient capsize. Of course, we may also try to determine where the saddle connection occurs and use this as an estimate for the transient capsize boundary.

The numerical location of saddle connection events is a laborious and computer in-

tensive process and the use of an analytic method for locating approximately such events is highly desirable. One answer to the problem is Melnikov's Method for locating saddle connections. This technique has been shown to provide a good estimate of the homoclinic tangency in forcing parameter space for a number of simple nonlinear forced oscillators (Bikdash, Balachandran & Nayfeh 1994; Thompson 1997), therefore providing a good estimate for the domain of escape from a potential well.

In this chapter we explore some aspects of using Melnikov for systems of this type. We have seen in the previous chapter how biasing can be very important for the steady state dynamics. The significant feature of biased systems for transient dynamics is the existence of two potential hills with differing heights. The number of different saddle connection orbits is therefore greater than is the case for the symmetric or single hilltop systems. As a result, we find that the identification of the saddle orbit that leads to safe basin erosion is a key problem. Here we study the coexistence of homoclinic and heteroclinic connections from the hilltop saddle cycles and determine where they occur in parameter space. We also discuss the important factors governing the occurrence of these saddle connections.

Our primary reason for locating saddle connection boundaries is to predict the occurrence of basin erosion and thus any loss of system integrity (Foale & Thompson 1991). However, we cannot assume that the occurrence of saddle connections leads to basin erosion in a similar way seen for the quadratic escape equation. In this system the hilltop saddle homoclinic connection causes the initial basin erosion but this is followed by a complex series of saddle connection events between a number of steady states that eventually destroys the whole safe basin (Lansbury, Thompson & Stewart 1992). The complexity of the process means that we must be careful in extending these ideas to different systems, particularly if there is a number of possible hilltop saddle connections. For this reason we wish to deter-

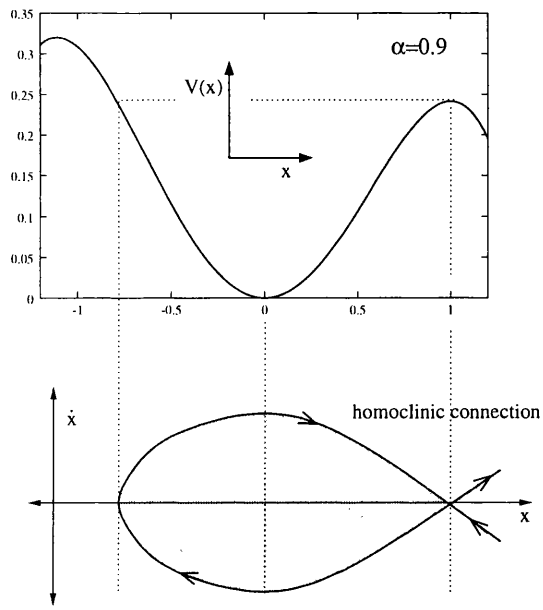

Figure 5.1: The potential well and phase portrait for the unforced, undamped system with $\alpha = 0.9$. Although there is only a homoclinic connection from the smaller of the saddle points for $\alpha = 0.9$, we may also surmise that two heteroclinic connections exist for the forced, damped system.

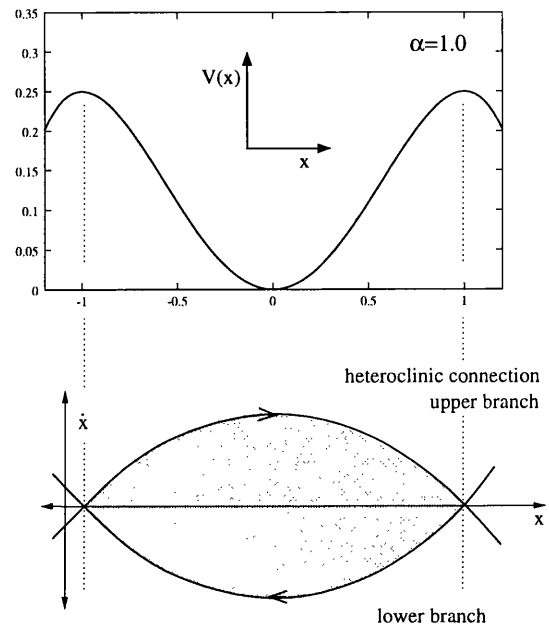

Figure 5.2: The potential well and phase portrait for the unforced, undamped system with $\alpha = 1.0$. Here we can see the heteroclinic connection that exists for the unforced undamped case. We use this orbit as a basis for the Melnikov approach to locating saddle connections. For $\alpha = 1$ the upper and lower branches are dynamically identical, this is not the case as α is reduced from 1.

mine which, if any, of these possible homoclinic or heteroclinic orbits may be used to estimate the transient capsize boundary.

5.2 The coexistence of homoclinic and heteroclinic connections

We now consider a potential well with two saddle points of slightly differing heights. For the forced, damped system we have 3 possible hilltop saddle connections;

1. homoclinic connection from the lower hilltop saddle (figure 5.1)
2. heteroclinic connection from higher to lower hilltop saddles (see figure 5.3)
3. heteroclinic connection from lower to higher hilltop saddles (see figure 5.3)

Note that only the first of these, the homoclinic connection, occurs in the Hamiltonian (unforced, undamped) system.

We are interested in where these connections occur in parameter space. To investigate this problem we again use the α parameterised escape equation (see chapter 2), where α is our symmetry breaking parameter.

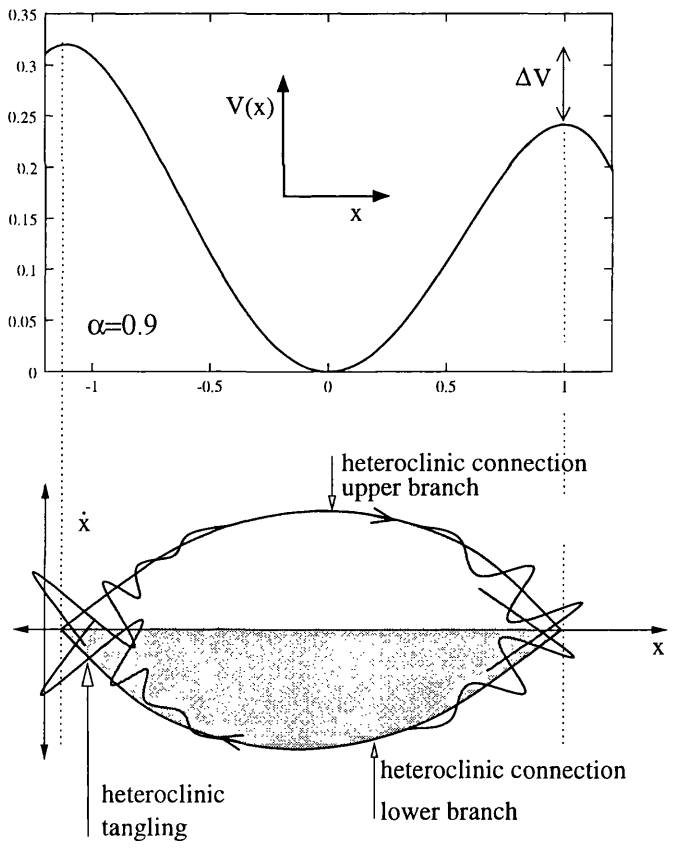

Figure 5.3: A schematic rendering of the two possible heteroclinic orbits for $\alpha < 1$.

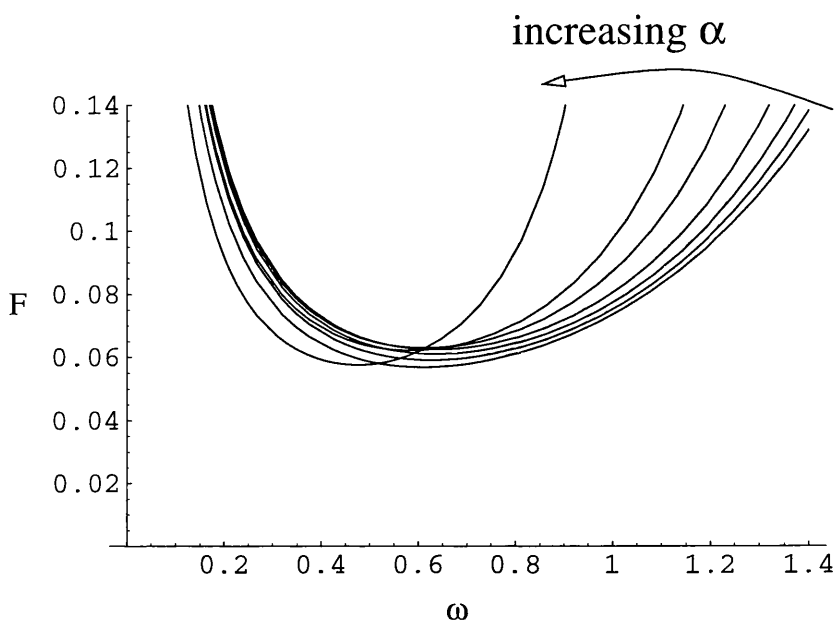

Figure 5.4: The homoclinic Melnikov curve for $\alpha = 0, 0.2, 0.4, 0.6, 0.8, 0.9, 0.999$ and $\beta = 0.1$.

5.3 Locating the saddle connections using Melnikov's Method

Following Thompson (1996) we apply Melnikov's Method by considering an energy balance around a saddle connection in the unforced, undamped system. Essentially we choose our saddle connection orbit in the unperturbed system and then balance energy lost through damping with that gained through forcing. Since there is no heteroclinic saddle connection in the Hamiltonian system for $\alpha < 1$, we must also perturb in α from the symmetric potential. In terms of the energy balance interpretation, we need to incorporate the additional energy gained or lost from the potential difference once the perturbation is added.

5.3.1 The homoclinic connection

We firstly specify the appropriate saddle connection orbit from which we wish to peturb. For the undamped, unforced case, with $\alpha < 1$, we are restricted in choice to the homoclinic connection from the smaller hilltop saddle, figure 5.1. Applying Melnikov's Method leads us to the following equation for the homoclinic connection (Gurd 1997) (see appendix A.1.1 for derivation);

$$F^M_{hom} = \frac{\sqrt{1+\alpha}\beta\left[\sqrt{-2\lambda+4\mu}\,(4\lambda+4\mu) - 12\lambda\,(1+2\alpha)\cosh^{-1}(\sqrt{\frac{2\mu}{\lambda}})\right]\sinh\left(\frac{\omega\,\pi}{\sqrt{1+\alpha}}\right)}{54\omega\pi\sqrt{2}\alpha^{\frac{3}{2}}\sqrt{-2\lambda+4\mu}\sin\left(\frac{\omega\cosh^{-1}\sqrt{\frac{2\mu}{\lambda}}}{\sqrt{1+\alpha}}\right)} \tag{5.1}$$

where

$$\lambda = (1-\alpha)\,(2+\alpha) \quad \text{and} \quad \mu = (1+2\,\alpha)^2 \tag{5.2}$$

If we now look at the F^M_{hom} boundary plotted as a function of ω, figure 5.4, we can make some observations. Firstly, for the homoclinic connection $F^M_{hom} \propto \beta$ as indeed it must for linear damping (see derivation). We also find that variation of α has little effect upon the boundaries. As $\alpha \to 1$ we find that the minimum point rises to higher F and then falls, whilst also shifting to a lower forcing frequency. The shift in frequency could be explained by increased softening of the system as the potential shape is altered (see chapter 2, figure 2.2). For practical purposes however, this shifting is small, given the approximate nature of the technique.

The accuracy of the Melnikov prediction for the homoclinic tangency for the $\alpha = 0$ escape equation (2.8) has been tested by Foale & Thompson (1991) and found to be accurate up to damping levels of $\beta \approx 0.2$. However, we cannot assume that this is the case for $\alpha > 0$ and this is explored further in 5.4.2.

5.3.2 The heteroclinic connection

We now wish to repeat the above analysis for the two possible heteroclinic connections between the two hilltop saddle solutions (for $\alpha < 1$). Note that the upper branch heteroclinic connection (from higher to lower saddle) can exist when we have damping but no forcing; we simply need to balance the energy lost through damping with that gained from the potential difference between the two hilltops, see figure 5.3. For the alternative heteroclinic connection to occur, forcing (or negative damping) is required.

To approximate these heteroclinic connections we again begin with those for the unforced, undamped, unbiased system ($F = \beta = 0$, $\alpha = 1$), and consider a small perturbation in these parameters. In comparison with the homoclinic analysis we are perturbing in the additional variable, α. The derivation is basically identical to that of the heteroclinic connection in the symmetric system (Nayfeh & Balachandran 1995), with an additional term accounting for the perturbation in α.

We now write down the condition for the upper and lower saddle connections to exist in the biased symmetric escape equation (see appendix A.1.3 for derivation),

$$F_{het}^{M} = \frac{\sqrt{2}\,\left(\alpha - 1 + \sqrt{2}\beta\right)\sinh(\frac{\omega\pi}{\sqrt{2}})}{3\omega\pi\sin(\omega t_0)} \qquad \text{upper branch} \tag{5.3}$$

where the trajectory is from the higher saddle to the lower, and

$$F_{het}^{M} = \frac{\sqrt{2}\,\left(\alpha - 1 - \sqrt{2}\beta\right)\sinh(\frac{\omega\pi}{\sqrt{2}})}{3\omega\pi\sin(\omega t_0)} \qquad \text{lower branch} \tag{5.4}$$

where the trajectory is from the lower saddle to the higher.

Note that we have left in the phase ωt_0, which is normally chosen to minimise F^M. For the lower branch we simply choose $\sin(\omega t_0) = -1$ (assuming non-negative damping). However, for the upper branch we need to change the phase (so that $\sin(\omega t_0) = \pm 1$) depending on whether $\left(\alpha - 1 - \sqrt{2}\beta\right)$ is positive or negative. It is when this term is equal to zero that the upper branch heteroclinic connection (approximately) exists in the damped unforced system.

In order to find the lowest possible F^M we can therefore rewrite these expressions,

$$F^M_{het} = \frac{\sqrt{2}\sinh(\frac{\omega\pi}{\sqrt{2}})}{3\omega\pi}\left|1 - \alpha - \sqrt{2}\beta\right| \qquad \text{upper branch} \tag{5.5}$$

$$F^M_{het} = \frac{\sqrt{2}\sinh(\frac{\omega\pi}{\sqrt{2}})}{3\omega\pi}\left(1 - \alpha + \sqrt{2}\beta\right) \qquad \text{lower branch} \tag{5.6}$$

where $0 \leq \alpha \leq 1$ and $\beta \geq 0$. We can now see that the lower branch connection will always exist at higher forcing amplitudes than the upper branch, for $0 \leq \alpha < 1$, unless we consider negative damping. Hence, we now focus on this branch, plotted in figure 5.5.

5.3.3 The unforced heteroclinic connection

If we set forcing to zero in equation (5.5) we obtain the following relationship between α and β

$$\sqrt{2}\beta = 1 - \alpha \tag{5.7}$$

This equation is an estimate of the damping required to balance the loss of potential energy between the two hilltops and is plotted against a numerically derived line in figure 5.6. We can see from the plot that this approximate approach is reasonably

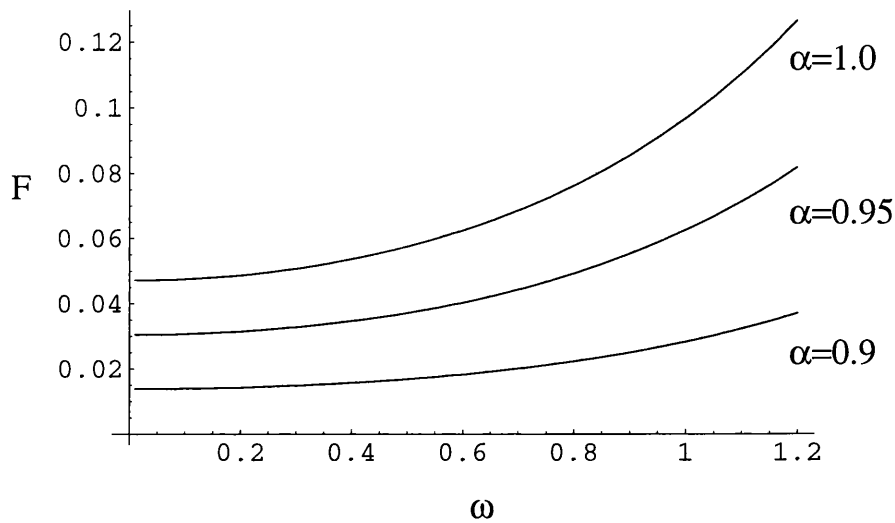

Figure 5.5: The upper branch heteroclinic connection for $\alpha = 0.9, 0.95$ and 1.0. The arc has a simple linear dependence on α.

accurate for perturbations of at least 10% in α.

We can now use the relationship between β and α to define heavily and lightly damped systems, see figure 5.7. In this way we effectively reduce the number of parameters we need vary; rather than studying the whole (α, β) plane we need only consider the heavy and light damping situations. Note that, although this reduction is valid only for the unforced system, it may still be usefully extended to the forced problem, as we discuss in the following section.

If we have light damping ($\sqrt{2}\beta < 1 - \alpha$), we find that trajectories from the higher saddle point escape and the phase portrait is similar to that of the single hilltop $\alpha = 0$ system, (a). For the heavily damped ($\sqrt{2}\beta > 1 - \alpha$) case, a trajectory from the higher saddle point spirals into the stable equilibrium, leading to a phase portrait similar to that of the symmetric $\alpha = 1$ system, (c). We henceforth refer to the case where damping exactly balances the potential energy gain as critical damping, (b).

We now examine how the addition of forcing affects the upper branch heteroclinic

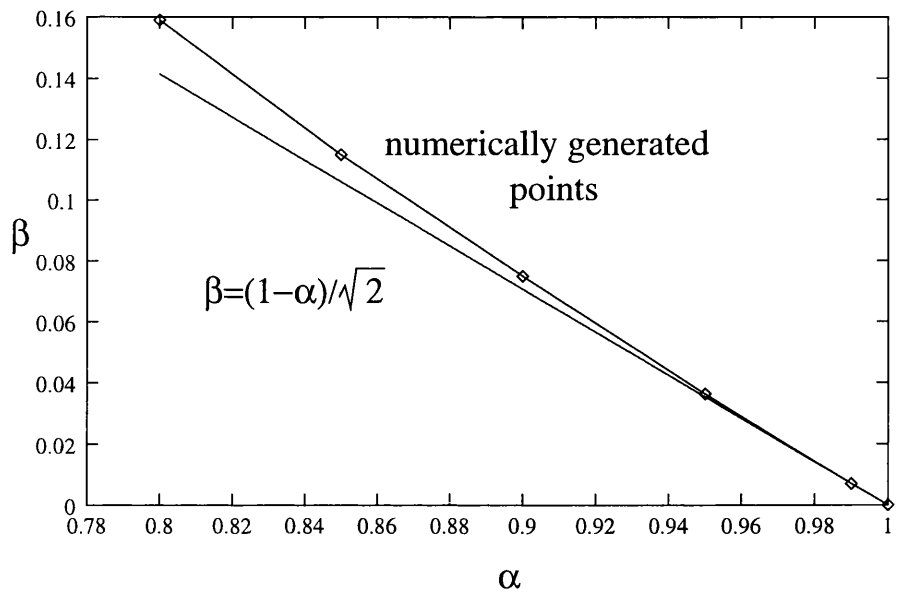

Figure 5.6: The damping required for a heteroclinic connection to exist in the unforced $\alpha < 1$ system. Plotted here is the approximate relationship derived using a perturbation approach, and points at which the connection exists in the numerically integrated system.

connection for heavy and light damping.

5.4 The saddle connections in the forced system

5.4.1 Accuracy of Melnikov's Method

We have seen how the relationship between α and β affects the phase portraits in the unforced system. We now add forcing and plot the two connections together for light and heavy damping, figures 5.9 and 5.8. We have omitted the lower branch heteroclinic connection since this only occurs at much higher forcing amplitudes. Shown are the Melnikov arcs along with boundaries where the saddle connections occur in the numerically integrated system. To generate the latter boundaries an algorithm for following saddle insets and outsets was used to determine when tangencies occurred. It is clear from these figures that Melnikov's Method gives a

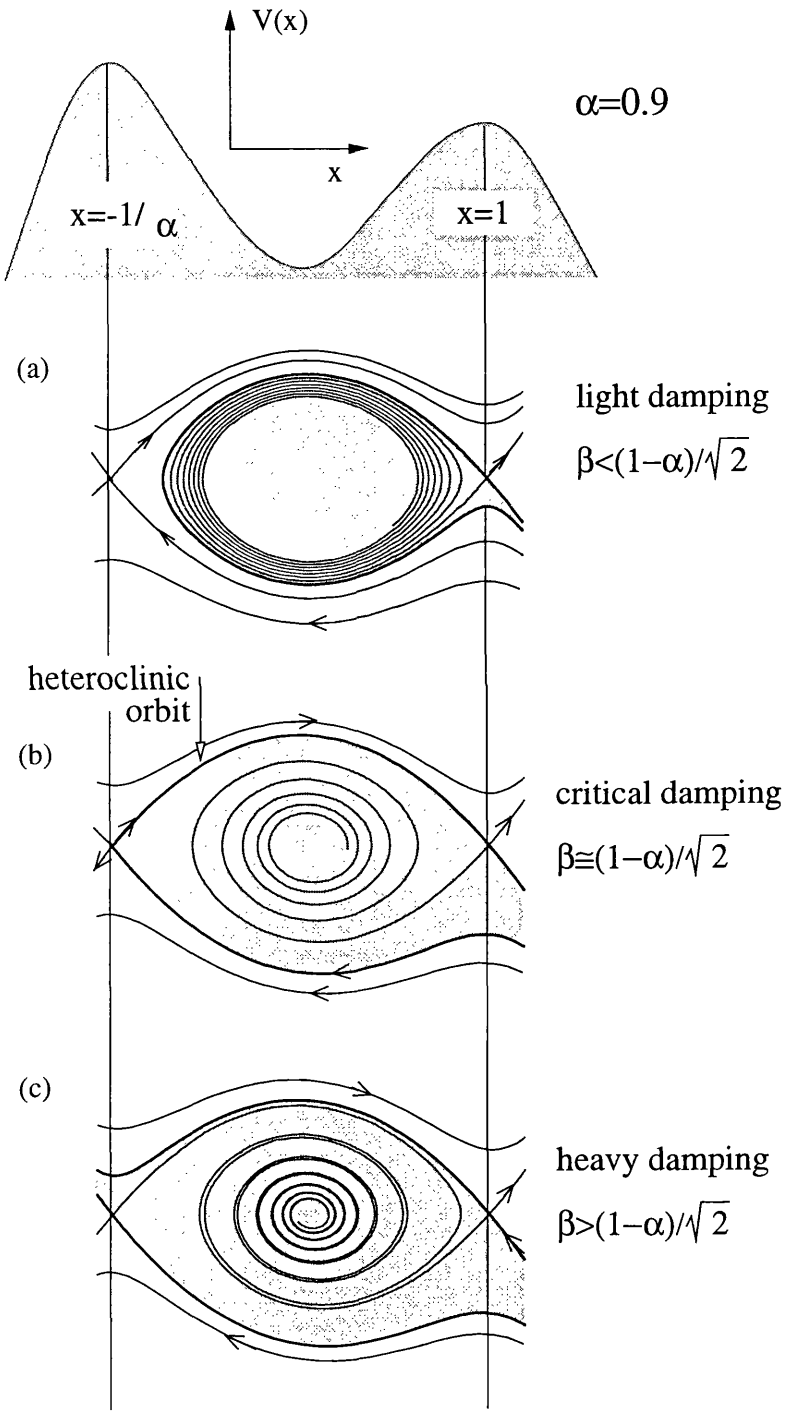

Figure 5.7: Phase portraits of unforced system for 3 levels of damping.

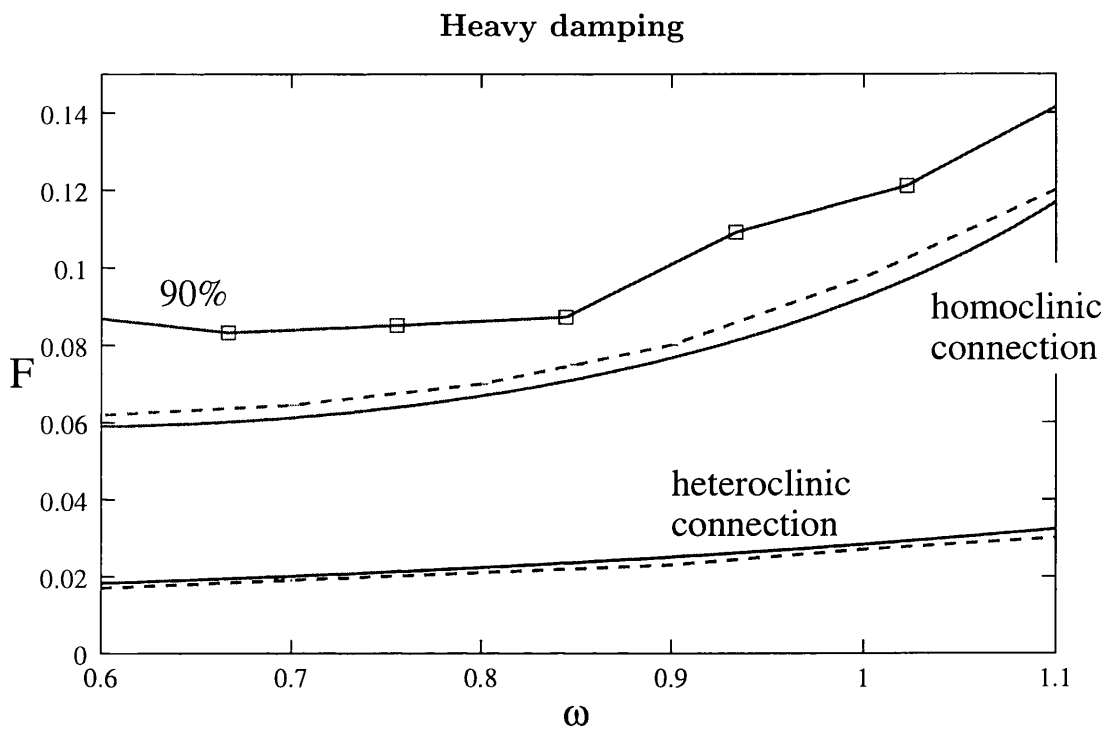

Figure 5.8: The homoclinic and heteroclinic connections for $\alpha = 0.95$ and $\beta = 0.1$. The dashed lines show the numerically determined connection boundaries. Also shown is the 90% of safe basin remaining line.

reasonably accurate estimation of the occurrence of these saddle connections, even for high forcing amplitudes.

With heavy damping, the heteroclinic connection occurs for lower F than the homoclinic. However if we now look at the lightly damped system, the reverse occurs, figure 5.9. We can see why this occurs by looking at the respective Melnikov expressions. The homoclinic arc is linearly dependent on damping and hence falls to lower forcing amplitudes as damping is reduced. The heteroclinic arc also falls as damping is reduced, but only to the point where it exists for zero forcing ($1 - \alpha \approx \sqrt{2}\beta$). Reduction of damping beyond this actually leads to the arc rising again as the phase term in (5.3) is switched by π.

If we refer once more to figure 5.7 an intuitive argument for this can be made. For the highly damped zero forcing case the phase portrait is qualitatively like that

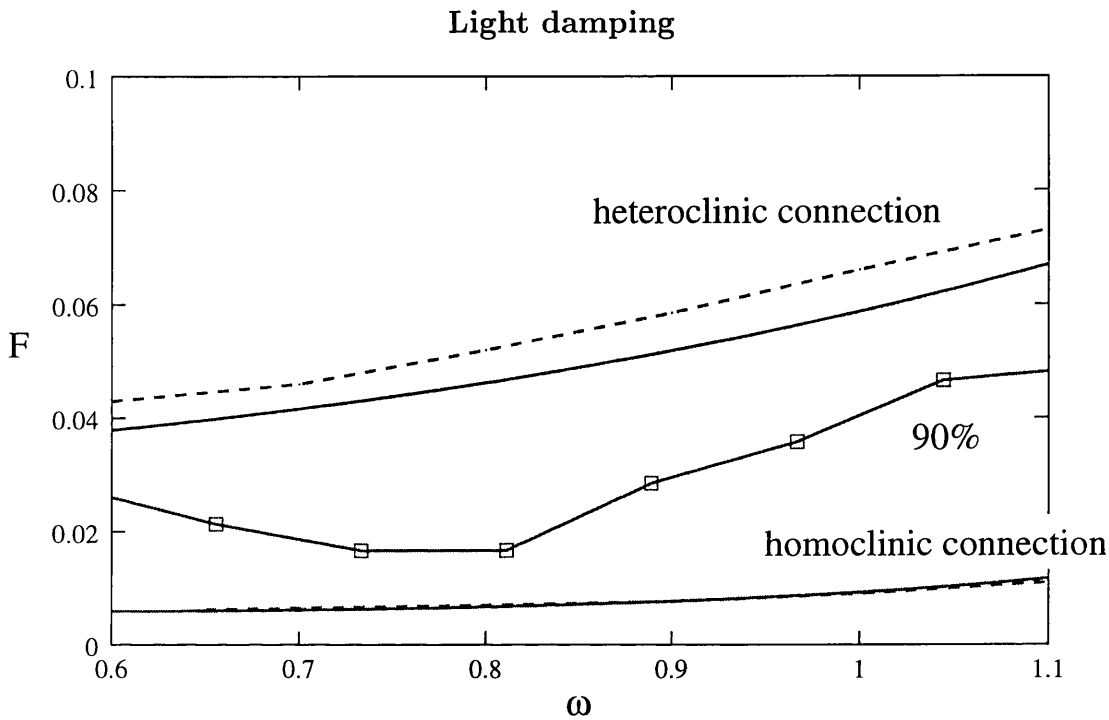

Figure 5.9: The homoclinic and heteroclinic connections for $\alpha = 0.9$ and $\beta = 0.01$. The dashed lines show the numerically determined connection boundaries. The 90% line refers to the points at which the safe basin is 90% of its zero forcing size.

of the symmetric system. With forcing we might therefore expect the heteroclinic connection to occur more readily (i.e. for lower forcing levels). In contrast, the lightly damped system has a phase portrait similar to that of the quadratic restoring escape equation, and we similarly expect the homoclinic connection to occur first.

In both figures we see that the Melnikov prediction is less accurate for the connection at higher F values. This is simply because the perturbation is greater for larger F. Similarly we find that the estimate for the heteroclinic connection is worse since we are perturbing in 3 variables rather than 2.

We illustrate these findings further in figure 5.10 in which the two saddle connection boundaries are plotted as functions of β and ω. We can see in this diagram how the heteroclinic connection rises to higher F either side of the zero forcing connection

line.

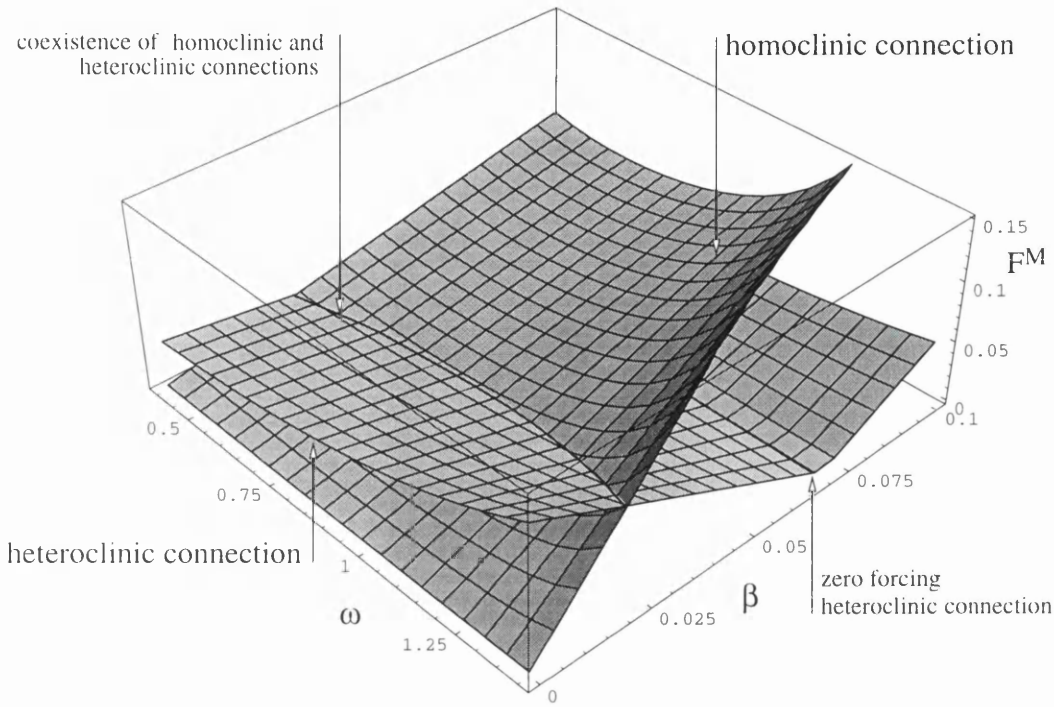

Figure 5.10: The homoclinic and heteroclinic connection boundaries plotted as functions of β and ω, for $\alpha = 0.9$. We can see how the heteroclinic boundary rises either side of the line defined in equation (5.7), and crosses the homoclinic boundary at lower damping levels.

5.4.2 Basin erosion

Finally we must address the issue of which saddle connection event has more significance for safe basin erosion. Plotted in figures 5.8 and 5.9 are lines showing approximately where 90% of the safe basin remains[1]. We can see from these that it is the homoclinic connection that has the more significant role in determining the onset of safe basin erosion. Significantly, this is for both the heavy and lightly damped cases. This is further illustrated in figures 5.11 5.12, which show how the erosion of the basins of attraction occurs. In fact the heteroclinic connection

[1]Here we take the safe basin size equal to 1 for zero forcing.

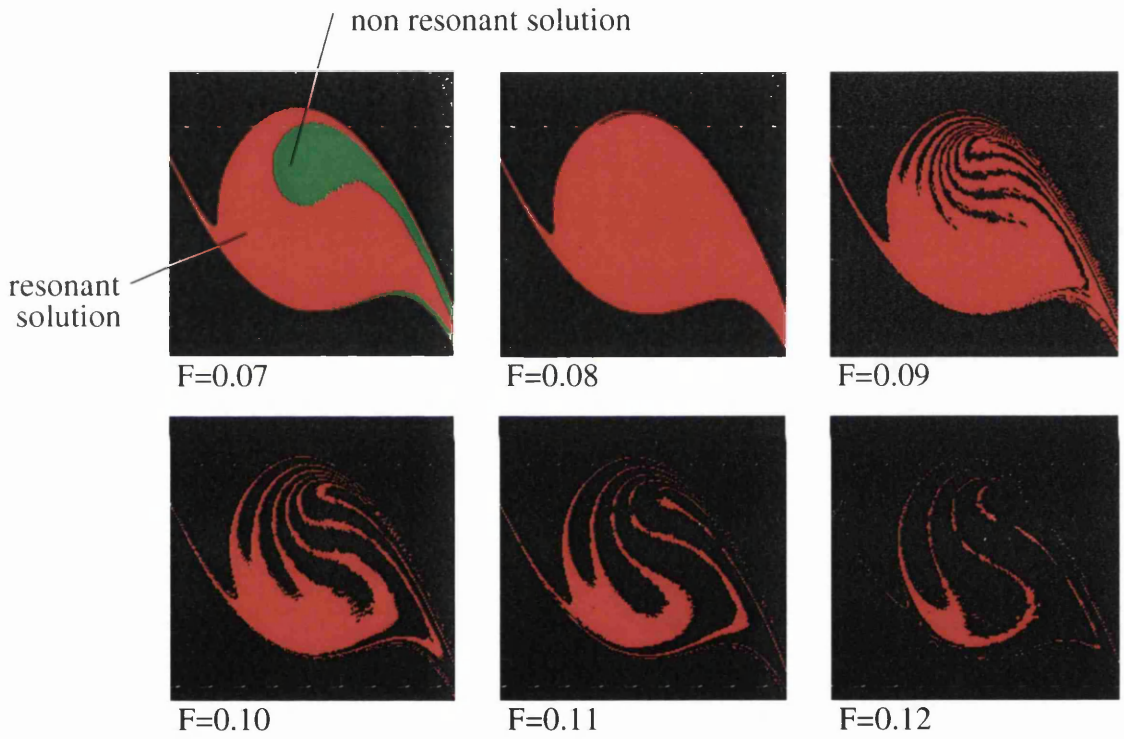

Figure 5.11: Basin erosion for the heavily damped system, with erosion occuring in the basin of attraction of the resonant solution (the non resonant steady state having ceased to exist beyond the fold A). Each cellmap shows the basins of attraction in $(x, \dot{x})$ space, with $(0, 0)$ in the centre.The homoclinic connection occurs at $F \approx 0.07$ and we can see the first fractal incursion at $F = 0.08$. Qualitatively this is similar to erosion for the symmetric , cubic escape system.

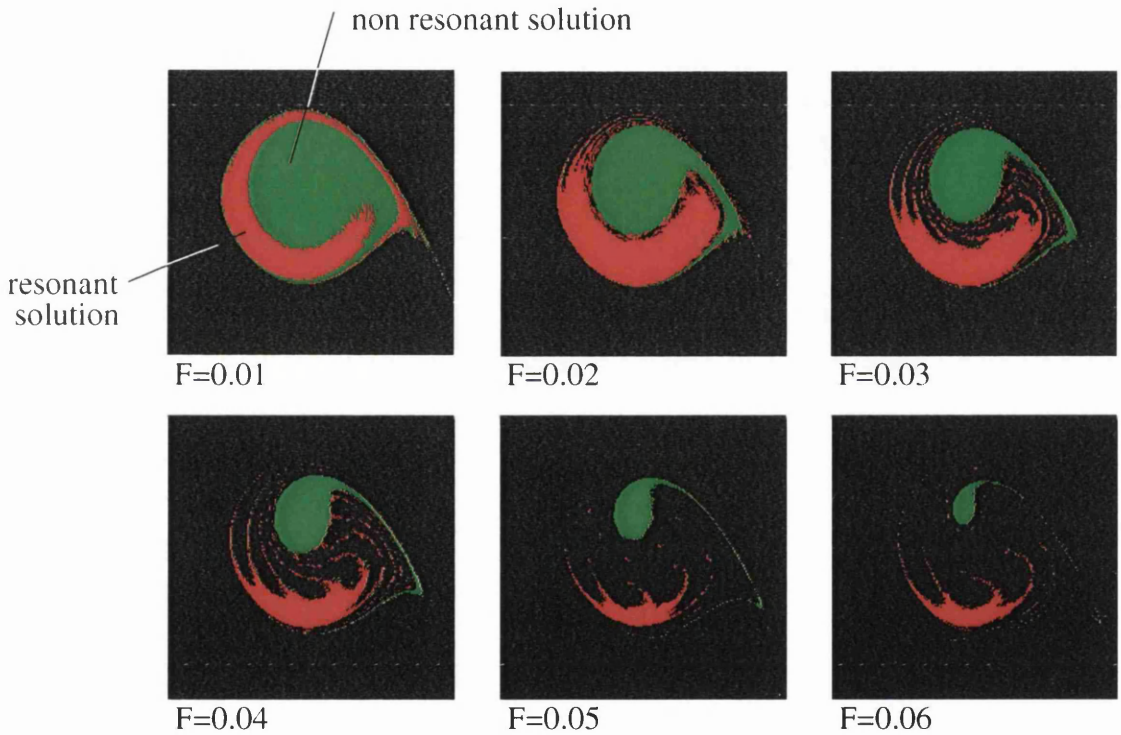

Figure 5.12: Basin erosion for the lightly damped system.Each cellmap shows the basins of attraction in $(x, \dot{x})$ space, with $(0, 0)$ in the centre. Erosion occurs in the basin of attraction of the resonant steady state. The homoclinic connection occurs at $F \approx 0.01$ and we can see the first fractal incursions at $F = 0.02$. Qualitatively this is similar to erosion for the asymmetric quadratic escape system.

appears to have very little effect on basin erosion. To see why this is the case a thorough investigation of the heteroclinic and homoclinic tangling events is required which is beyond the scope of this work. However, this seems an interesting topic for further research.

5.5 Conclusions

Melnikov's Method has been widely used to estimate the location of saddle connection orbits in parameter space (Bikdash, Balachandran & Nayfeh 1994; Foale & Thompson 1991). Typically it has been applied to simple nonlinear oscillators with quadratic or cubic potential wells. Motivated by the need to model slightly biased ship capsize, we have examined its application to single well systems with two potential hills of differing heights. For this purpose we have again used the α-parameterised system first introduced as a ship roll model by MacMaster & Thompson (1994).

For these twin hilltop potentials we have described three possible saddle connecting orbits. Using Melnikov's Method, we have evaluated expressions for the occurrence of these connections. In particular, we have investigated the significance of parameters governing the bias and damping. Using this approach it is possible to show how the balance between energy loss through damping and that gained from the potential difference between the saddle points governs the occurrence of the heteroclinic tangency.

Finally we observed that the homoclinic tangency provides the best estimate for the occurrence of basin erosion, even where the heteroclinic occurs first.

Chapter 6

DAMPING FUNCTIONS

6.1 Introduction

In chapter 2 we described the derivation of a simple design formula (SDF) for predicting capsize. While this formula gives excellent predictions for worst case capsize in linearly damped systems, the incorporation of nonlinear damping poses a problem. Also in chapter 2, comparison of the SDF with severe wave slopes lead to the conclusion that a linear damping ratio of approximately 0.3 is required to prevent capsize. As noted, this seems a high damping level: but remembering that roll damping is highly nonlinear, the ratio must be given a relatively high value to take into account the strong damping at high roll amplitudes. This question of how we might choose a suitable linear model for damping remains an open one. In fitting an equivalent linear coefficient to a nonlinear damping characteristic it has been suggested that the roll amplitude should be assumed to be approximately one half of the angle of vanishing stability, (Thompson 1997). Obtaining a damping ratio in this way seems reasonable, but there is a need for a more systematic approach. This is particularly true for the transient capsize problem, for which it

is difficult to associate a roll amplitude with capsize. In this chapter we assess the effect of choosing a particular amplitude for the damping ratio and how sensitive our capsize predictions might be to our choice of amplitude.

We then propose a new, capsize based method for deriving an equivalent damping ratio, and illustrate how it is calculated for two example restoring functions.

6.2 The equivalent damping ratio

The traditional approach, sketched out below, uses energy balance over cycles of an harmonic oscillation to obtain a relationship between the nonlinear damping coefficients and an equivalent linear damping coefficient. This relationship is a function of the amplitude of the oscillation.

The basic idea is to require that the energy lost through damping over one period of oscillation be the same for the nonlinearly damped and the equivalent linearly damped roll motion. The effectiveness of this method therefore depends upon how close the real motion is to the harmonic oscillations used for the equivalence. In this section we test the validity of the standard equivalent linear damping.

In order to derive a formula for equivalent linear damping, we return once more to our non-dimensional model for roll motion,

$$\ddot{x} + b(\dot{x}) + c(x) = 0 \tag{6.1}$$

where we have set forcing to zero. As before we also let

$$b(\dot{x}) = b_1\dot{x} + b_2\dot{x}|\dot{x}| + b_3\dot{x}^3 \quad \text{and} \quad c(x) = x(1-x)(1+\alpha x) \tag{6.2}$$

where, typically, either b_2 or b_3 is taken to be zero (Dalzell 1978). We have assumed

that damping can be accurately modelled using only velocity dependent terms. This is a sensible simplification, given that the dynamics imply a relationship between velocity and displacement (or angle) (Haddara & Bennet 1989).

Now we wish to find an equivalent linear damping ratio that gives the same energy loss over a cycle. For low amplitudes, we may approximate the motion as linear ($c(x) \approx x$ for small x). Remember that since amplitudes are generally lower than $a \approx 0.5$ (or $\theta_V/2$), the linear approximation for restoring is reasonable. Thus, assuming an harmonic solution, $a \cos t$, and equating the energy losses over half a cycle[1],

$$\int_{-a}^{a} 2\zeta \dot{x} dx = \int_{-a}^{a} b_1 \dot{x} + b_2 \dot{x}|\dot{x}| + b_3 \dot{x}^3 dx \tag{6.3}$$

$$= \int_{-a}^{a} \left[b_1 \dot{x} + b_2 \dot{x}|\dot{x}| + b_3 \dot{x}^3\right] \dot{x} dt \tag{6.4}$$

$$\begin{aligned} \Longrightarrow 2\zeta a^2 \int_0^{\pi} \sin^2 t dt &= b_1 a^2 \int_0^{\pi} \sin^2(t) dt \\ &\quad + b_2 a^3 \int_0^{\pi} \sin^3(t) dt + b_3 a^4 \int_0^{\pi} \sin^4(t) dt \end{aligned} \tag{6.5}$$

which leads us finally to,

$$\zeta(a) = \frac{1}{2} b_1 + \frac{4a}{3\pi} b_2 + \frac{3a^2}{8} b_3 \tag{6.6}$$

This is a formula for an equivalent linear damping in terms of the nonlinear damping coefficients and the amplitude at which the motion occurs.

[1] We use half a cycle to avoid complications with the $\dot{x}|\dot{x}|$ term.

6.2.1 Using the equivalent damping ratio for a forced system

Using the method outlined above, the damping ratio is a function of the oscillation amplitude, a, and so cannot be relied upon as a good representation of damping for any amplitude other than that for which it is measured or chosen. The importance of this factor depends on the behaviour we wish to model. If we are interested only in steady state oscillation, then we can select ζ for the required amplitude of motion. However, the study of a phenomenon such as capsize must necessarily require a model for damping that includes high and low amplitudes of motion. One solution is to choose some amplitude that best reflects the motion shortly before capsize, such as $a = 0.5$, equivalent to roll amplitudes of half the angle of vanishing stability, (Thompson 1997). However, it is not clear how one might apply this approach to transient motions.

To investigate the sensitivity of capsize modelling to this approach, we now define a family of nonlinear damping functions with fixed damping ratio at some roll amplitude, a.

Deriving a family of damping functions

In order to define a family of damping functions, we specify the nonlinear damping function to have an equivalent linear damping ratio of ζ for an oscillation amplitude of a. To simplify the study we consider only linear plus quadratic damping (so $b_3 = 0$). It then follows from (6.6) that

$$b_2 = \frac{3\pi}{4a}(\zeta - b_1/2) \tag{6.7}$$

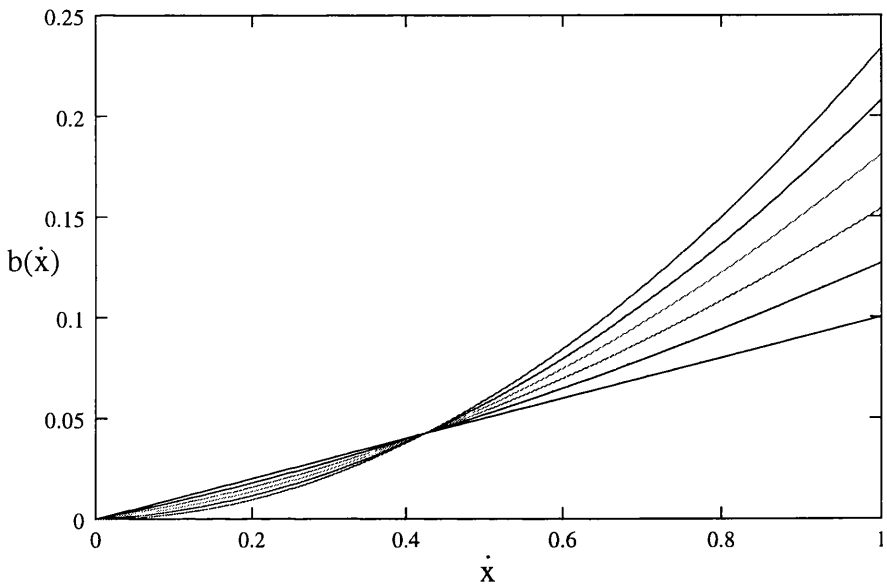

Figure 6.1: A family of damping functions with the same equivalent linear damping ratio ($\zeta = 0.05$) for $a = 1/2$.

The quadratic damping function can then be written

$$b(\dot{x};\beta) = \beta\dot{x} + \frac{3\pi}{4a}(\zeta - \frac{\beta}{2})\dot{x}|\dot{x}| \tag{6.8}$$

where β is our 'nonlinearity' parameter. For $\beta = 0$ we have a fully nonlinear damping function and for $\beta = 2\zeta$ the damping is linear. As we vary β the equivalent linear damping (as defined in (6.6)) is constant at a chosen amplitude, a. By choosing suitable values for a and ζ, we can thus construct a family of damping functions. In figure 6.1, such a family of damping functions is plotted for $\zeta = 0.05$ at $a = 0.5$.

Thus, using this simple idea of equivalence we have produced a set of systems for which the damping is equivalent in an energy loss sense, at a particular amplitude. How well this concept performs when applied to capsize modelling can now be tested.

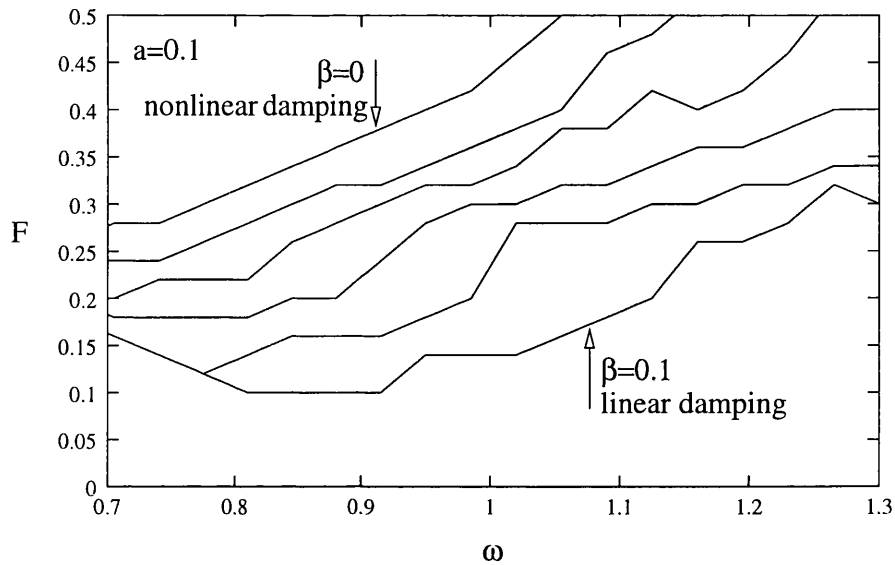

Figure 6.2: Transient capsize for a family of damping functions with $a = 0.1$ and $0 < \beta < 0.1$. For this low value of a the nonlinearity becomes far more important and has a dramatic effect on the forcing required to cause capsize.

6.2.2 Transient capsize and nonlinear damping

To investigate the sensitivity of capsize modelling to our damping function, we firstly use the transient capsize diagrams introduced in chapter 3. As stated before, this problem is particularly important for transient motions, since we cannot associate a certain roll amplitude with capsize. By studying how transient capsize changes as we vary our family of damping functions, we can see the significance of nonlinearity in the damping. To simplify our analysis we focus on the transient capsize boundary. This is the minimum forcing amplitude for which transient capsize (defined as in chapter 3) occurs, determined over a range of frequencies.

Figures 6.2 to 6.4 show how important the choice of a may be in determining how different the escape behaviour is over a family of damping functions. Plotted in these diagrams are the capsize boundaries with $\alpha = 0$ restoring, for the different damping families. Each family is generated for $\zeta = 0.05$ at three values of a. For $a = 0.1$, capsize is heavily suppressed as the damping becomes more nonlinear.

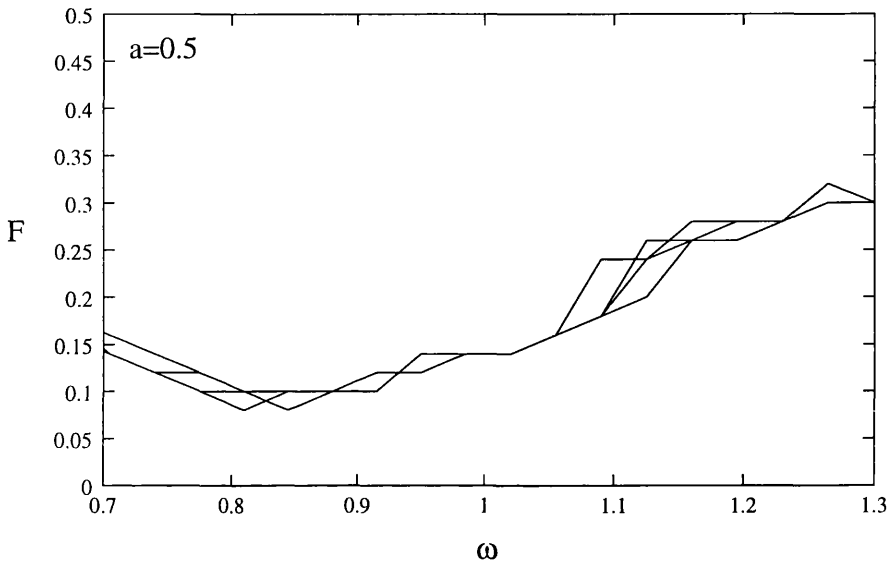

Figure 6.3: Transient capsize for a family of damping functions with $a = 0.5$ and $0 < \beta < 0.1$. The nonlinearity of the damping makes little difference.

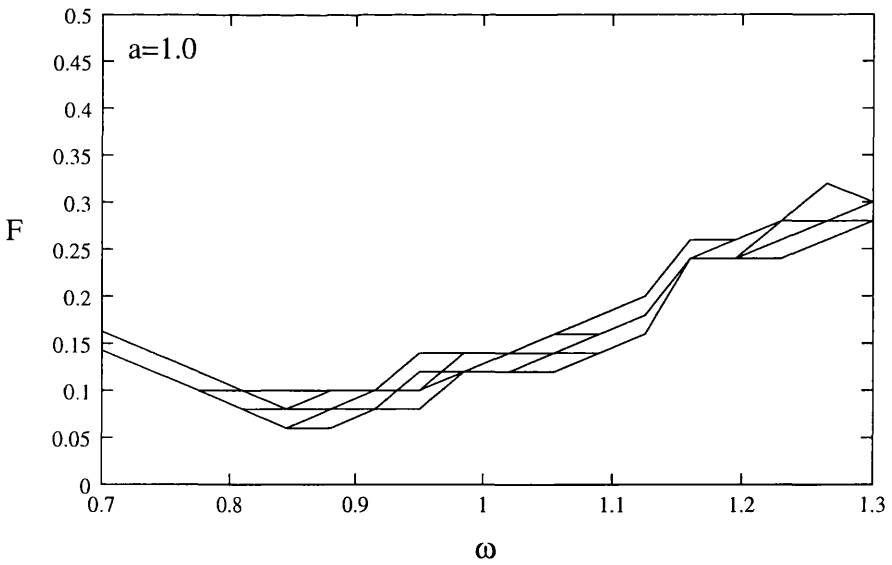

Figure 6.4: Transient capsize for a family of damping functions with $a = 1.0$ and $0 < \beta < 0.1$. Again the amount of nonlinearity in the damping has little effect on capsize.

The spreading of the escape lines can be seen to demonstrate the inaccuracy of an equivalent linear damping model for lower a. For the damping families with $a = 0.5$ and $a = 1.0$ we find that capsize is insensitive to our choice of β. Essentially this means that the equivalent linear damping model gives a close estimate for the nonlinear models, providing it is chosen for high amplitude motions.

6.2.3 Steady state capsize and nonlinear damping

Steady state capsize occurs when we alter a parameter by a small amount and the steady state either ceases to exist or loses stability. If the system is not in the basin of attraction of another stable steady state then capsize typically takes place extremely quickly. Although, in this case, we may define an amplitude from which steady state capsize occurs, we are still interested in how sensitive our modelling may be to this choice. We therefore repeat the previous analysis for steady state capsize, figures 6.5 to 6.7. A similar sensitivity to a is seen here, again across a wide range of frequencies around resonance. Hence we find our choice of damping model to be important for the different capsize mechanisms either side of resonance. It should, however, be noted that sensitivity is reduced at lower frequencies in figure 6.7 where capsize occurs from the fold bifurcation.

6.2.4 Choosing amplitudes for equivalent damping

So, our choice of a (the amplitude at which the equivalent linear damping is determined), is something with which we must be careful. Perhaps unsurprisingly, we have found that using a linear damping model determined for low amplitude motion gives the worst model for capsize. This is shown more clearly in figures

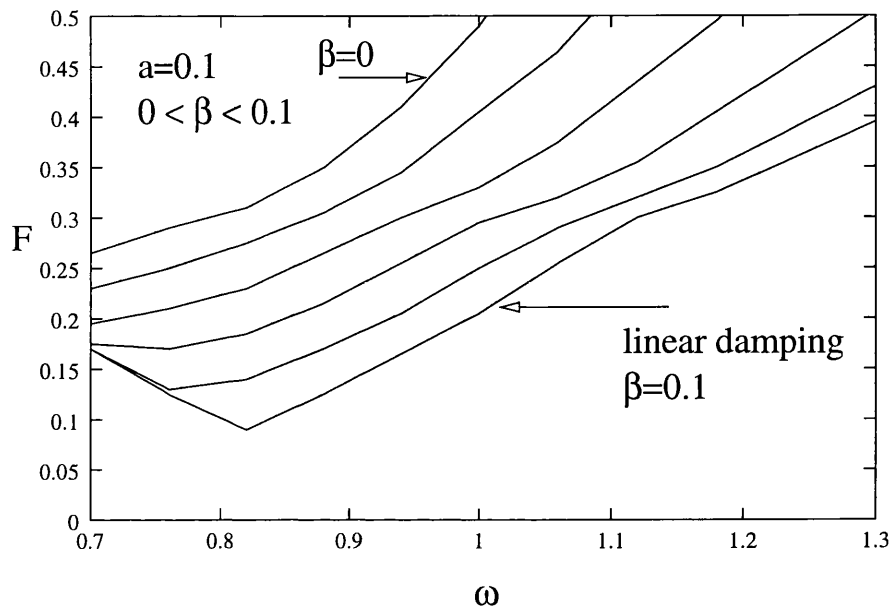

Figure 6.5: Steady state capsize for a family of damping functions with $a = 0.1$ and $0 < \beta < 0.1$. For this low value of a the nonlinearity becomes far more important and has a dramatic effect on the forcing required to cause capsize.

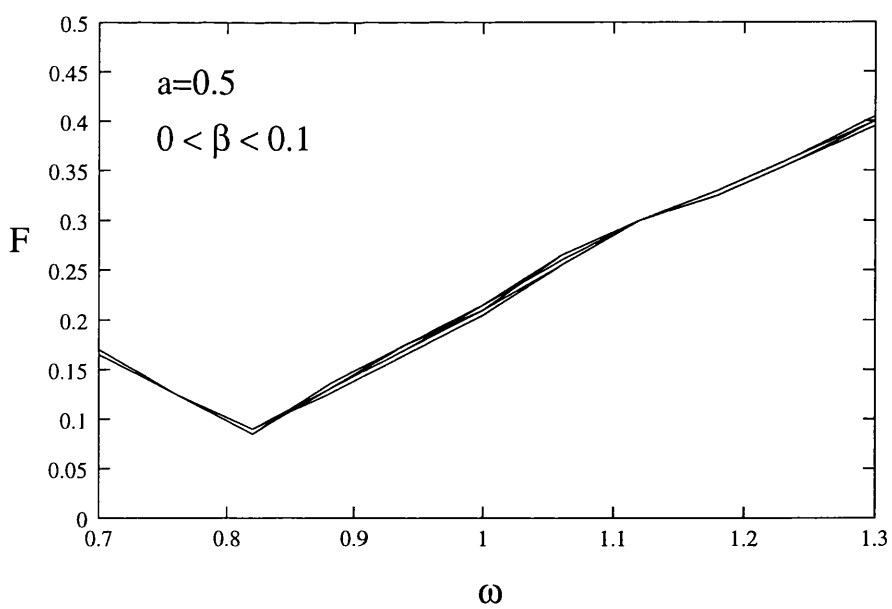

Figure 6.6: Steady state capsize for a family of damping functions with $a = 0.5$ and $0 < \beta < 0.1$. The nonlinearity of the damping makes little difference.

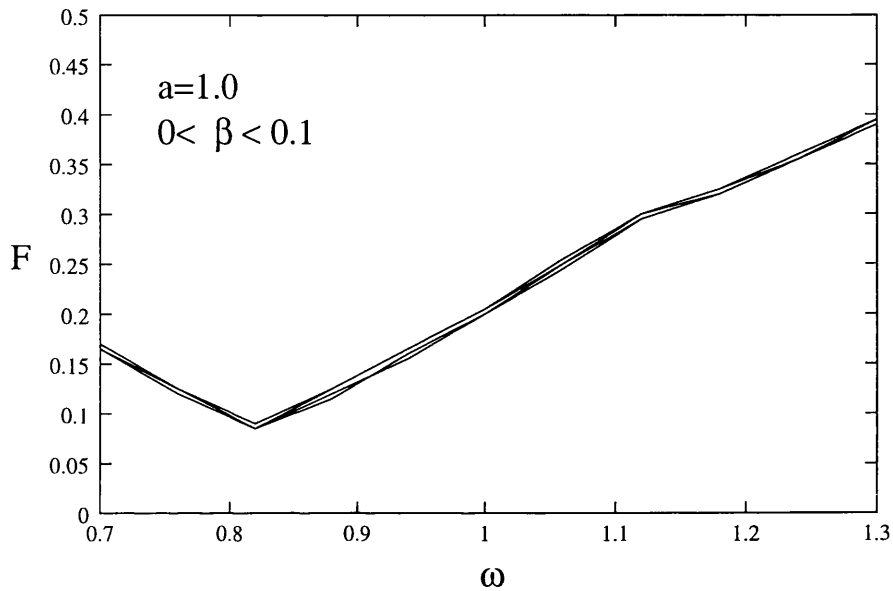

Figure 6.7: Steady state capsize for a family of damping functions with $a = 1.0$ and $0 < \beta < 0.1$. Again the amount of nonlinearity in the damping has little effect on capsize.

6.8 and 6.9, where the mean difference[2] between $\beta = 0$ and $\beta = 0.1$ (nonlinear and linear damping respectively) capsize lines for each damping family is plotted against a, the amplitude for which that family is defined. The first figure shows the results for transient capsize and the second for steady state. The first point to note is the considerably worse sensitivity for the transient case (e.g. twice as bad for $\alpha = 0$ and $a = 0.2$). This is probably due to the less sensitive nature of steady state capsize from the fold bifurcation, which occurs at lower amplitudes. This feature can be seen at lower frequencies in figure 6.5.

It is clear that for both systems plotted in figures 6.8 and 6.9, the choice of a can have a dramatic effect on how close the equivalent linearly damped system is to the nonlinear, in terms of capsize. Choosing high values for a is certainly the safest option but we can identify minima in both lines, particularly for transient capsize.

[2]This measure of the difference is constructed by adding the percentage differences between linear and nonlinearly damped capsize boundaries from one damping family and taking the mean over the frequency range.

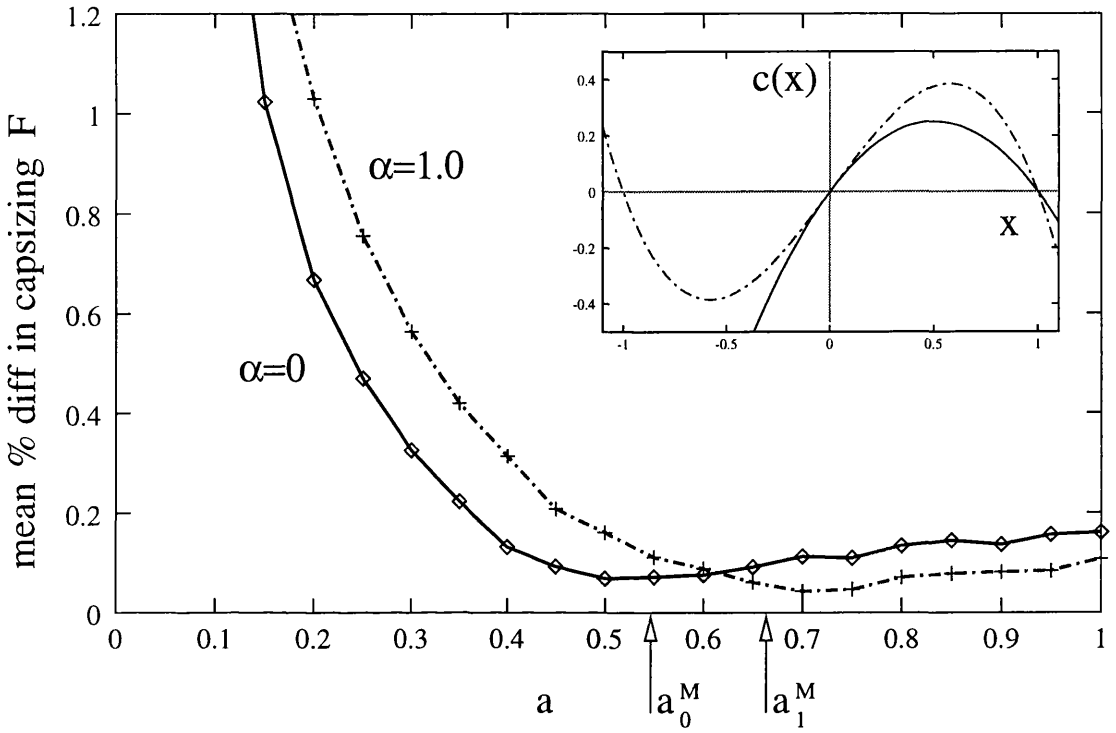

Figure 6.8: Mean difference in linearly and nonlinearly damped transient capsize lines, plotted for asymmetric and symmetric restoring. Also marked on the diagram are the amplitudes at which equivalence is expected to work best, a^M (according to the Melnikov equivalent damping described in section 6.3). For both cases the family of damping functions has $\zeta = 0.05$ at the specified amplitude. The range of frequencies taken was $0.7 < \omega < 1.8$.

The presence of these minima implies that there is an optimal choice for a if we wish to match the linearly and nonlinearly damped systems as close as possible when studying capsize. This represents the amplitude from which capsize approximately occurs. We can identify this optimal a from the diagram in figure 6.8 but it is also possible to show why the minima occur at certain a values and in the next section we develop a method for identifying the best choice of a, using Melnikov's Method. This involves deriving a new concept of equivalence, aimed specifically at capsize studies.

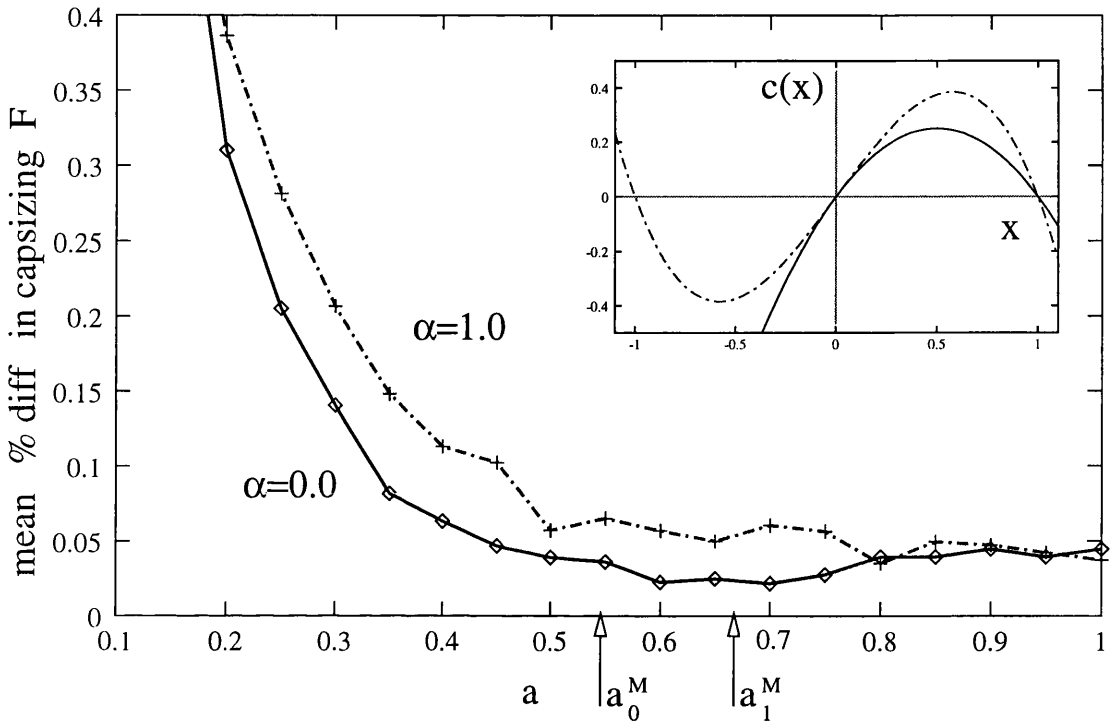

Figure 6.9: Mean difference in linearly and nonlinearly damped steady state capsize lines, plotted for asymmetric and symmetric restoring. Here we see a less marked sensitivity than for transient capsize, the mean difference being generally lower. Also marked on the diagram are the amplitudes at which equivalence is expected to work best, a^M (according to the Melnikov equivalent damping described in section 6.3). For both cases the family of damping functions has $\zeta = 0.05$ at the specified amplitude. The range of frequencies taken was $0.7 < \omega < 1.8$.

6.3 An equivalent damping ratio for capsize

Instead of requiring the energy lost through damping around a cycle to be equal for two 'equivalent' systems, we can use different definitions of equivalence, depending on the behaviour, or features of the system we wish to study.

One alternative is to demand that the equivalent linear damping satisfes criteria based on transient or steady-state capsize. Furthermore, if we use harmonic balance or Melnikov Methods, it seems possible to write down explicitly an expression for the equivalence.

Here we demonstrate this approach by deriving an equivalent damping ratio using

an equivalence based on a Melnikov analysis. One advantage of this particular approach is that it tackles the problem of transient capsize. As discussed in chapters 3 and 5, the sudden erosion of the safe basin after a saddle connection event can be used as a guide to where such transient capsize will occur. We can use the Melnikov's Method to derive an approximate curve for the saddle connection in forcing parameter space (F, ω). Further details on this technique and its application to capsize modelling are described in chapter 5.

We again use our non-dimensional roll model,

$$\ddot{x} + b(\dot{x}) + c(x) = 0 \tag{6.9}$$

where as before the damping term $b(\dot{x})$ depends on some number of parameters $b_1 \cdots b_n$. We then consider an 'equivalent' system,

$$\ddot{x} + 2\zeta\dot{x} + c(x) = 0 \tag{6.10}$$

We now wish choose ζ such that the resultant system satisfies a Melnikov based criteria, derived from a capsize perspective.

6.3.1 Transient capsize equivalence

To find an equivalent damping for a transient capsize, we can now perform a Melnikov analysis on the 'real' and equivalent systems. It is then possible to choose ζ so that the $F^M(\omega)$ curves (and hence the predicted capsize domain) are the same for both damping functions.

We again view Melnikov analysis as an energy balance over the relevant homoclinic

or heteroclinic orbit. For the nonlinearly damped system this gives,

$$E_{loss} = E_{gain} \tag{6.11}$$

$$\Longrightarrow \int b(\dot{x})dx = \int F\sin(\omega t + t_0)dx \tag{6.12}$$

$$\Longrightarrow \int_{-\infty}^{\infty} b(\dot{x})\dot{x}(t)dt = \int_{-\infty}^{\infty} F\sin(\omega t + t_0)\dot{x}(t)dt \tag{6.13}$$

where $\dot{x}(t)$ is found for the homoclinic or heteroclinic orbit in the Hamiltonian system and the integrals are taken over this orbit. Note that the choice of this orbit may not always be a simple procedure.

Rewriting then gives

$$F^M = \frac{\int_{-\infty}^{\infty} b(\dot{x})\dot{x}(t)dt}{\int_{-\infty}^{\infty} \sin(\omega t + t_0)\dot{x}(t)dt} \tag{6.14}$$

If we again write $b(\dot{x}) = b_1\dot{x} + b_2|\dot{x}|\dot{x} + b_3\dot{x}^3 + \cdots$ then this result can be rewritten in terms of a sum of integrals for each damping term,

$$F^M = \frac{b_1 I_1 + b_2 I_2 + b_3 I_3 + \cdots + b_n I_n}{I_F(\omega)} \tag{6.15}$$

where $I_F(\omega)$ is the denominator of equation (6.14). The dependence on t_0 has been dropped since the 'worst case' (lowest F^M) result will be chosen (see chapter 5). The important feature here is that the damping terms have no dependence on forcing frequency.

If we go through the same process for the linearly damped system it is easy to see

that the result will be

$$F^M = \frac{2\zeta^M I_1}{I_F(\omega)} \tag{6.16}$$

where ζ^M is to be the Melnikov equivalent damping.

This means that exactly the same $F^M(\omega)$ curve can be obtained for the linear system, providing

$$\zeta^M = \frac{b_1 I_1 + b_2 I_2 + b_3 I_3 + \cdots + b_n I_n}{2I_1} \tag{6.17}$$

where

$$I_n = \int_{-\infty}^{\infty} \dot{x}^{n+1}(t)dt \qquad \text{for odd } n \tag{6.18}$$

$$I_n = \int_{-\infty}^{\infty} |\dot{x}|\dot{x}^n(t)dt \qquad \text{for even } n \tag{6.19}$$

We have thus defined a Melnikov equivalent linear damping (MED), ζ^M (Bikdash, Balachandran & Nayfeh 1994). This can now be derived for two example systems. Its effectiveness can be tested by comparison of the nonlinear terms in (6.17) with the minimum a values found in figure 6.8.

6.3.2 A Melnikov equivalent damping

In order to find the Melnikov equivalent damping for a particular system we require solutions for the integrals in equation (6.17). Since each integral is a function of the velocity over the orbit, they are determined by the restoring function $c(x)$.

We derive here ζ^M for our two example systems with asymmetric and symmetric restoring.

Quadratic restoring

For this example we take the restoring force to be $x - x^2$, or $\alpha = 0$ in (6.2). For this case we are interested in the homoclinic orbit from the saddle point at $x = 1$. As before we locate the orbit in the Hamiltonian system and then find the energy loss around this orbit.

This gives the following result (see appendix A.2);

$$\zeta^M = \frac{1}{2}b_1 + \frac{15}{64}b_2 + \frac{9}{77}b_3 \tag{6.20}$$

Comparison of the nonlinear terms in the above result with the standard (harmonic balance) definition of equivalent damping (6.6) allows us to define an amplitude, a^M, for which the two expressions give the approximately the same ζ or

$$\zeta^M \approx \zeta(a^M) \tag{6.21}$$

Thus we find that for the escape equation, comparison of the damping terms gives (appendix A),

$$a_0^M \approx 0.56 \tag{6.22}$$

Cubic restoring

For this example we take the restoring force to be $x - x^3$ ($\alpha = 1$ in (6.2). We are therefore interested in the heteroclinic orbit between the two saddle points

at $x = \pm 1$ in the Hamiltonian system. By evaluating the relevant energy loss integrals (see appendix A) and substituting into (6.17) we eventually arrive at,

$$\begin{aligned} \zeta^M &= \left[\frac{4}{3\sqrt{2}}b_1 + \frac{8}{15}b_2 + \frac{16}{35\sqrt{2}}b_3\right]\frac{3\sqrt{2}}{8} \\ \Longrightarrow \quad \zeta^M &= \frac{1}{2}b_1 + \frac{2\sqrt{2}}{10}b_2 + \frac{6}{35}b_3 \end{aligned} \tag{6.23}$$

which we can once more compare to the energy balance equivalent damping, (6.6), by finding the amplitude for which $\zeta(a) \approx \zeta^M$. This gives (see appendix A.2),

$$a_1^M \approx 0.67 \tag{6.24}$$

Comparison of these two values for a^M to the minima in figures 6.8 and 6.9 shows that for transient escape, the use of the Melnikov equivalent damping gives a good approximation to the nonlinear system, for transient capsize modelling in particular.

6.4 An improved design formula

Having derived a Melnikov equivalent damping we can now use it to improve upon the simple design formula (2.22). If we replace ζ with the equivalent nonlinear damping function and set $\mu = 1$, then we obtain

$$\text{Critical wave slope} = Ak_{crit} = 2\left[\frac{1}{2}b_1 + \frac{15}{64}b_2 + \frac{9}{77}b_3\right]\theta_V \tag{6.25}$$

where we have used the MED from the quadratic restoring model.

Now we can substitute our real damping coefficient back in giving

$$Ak_{crit} = \frac{\theta_V B_1}{(ImgGM)^{1/2}} + \frac{30\theta_V^2 B_2}{64I} + \frac{18\theta_V^3 (mgGM)^{1/2} B_3}{77I^{3/2}} \tag{6.26}$$

where B_i are the dimensional damping coefficients, such that the damping term $B(\theta') = B_1\theta' + B_2|\theta'|\theta' + B_3\theta'^3$. We will refer to this formula as the improved design formula or IDF.

This new formula clearly has a more complicated dependence on GM, θ_V and I than the linearly damped version (the simple design formula) described in chapter 2. Interestingly, there will be a minimum point as we vary GM, suggesting a worst case GM which should be avoided. This is not a resonance phenomenon as the simple design formula requires the forcing to be tuned to resonant frequency. The situation is further complicated by the fact that one would expect θ_V to be a function of the position of the centre of gravity, and hence GM. However it is possible to identify some important characteristics of the IDF, e.g. the possibility of a worst case value for GM. For instance, if we focus on the dependence on GM alone, the expression reduces to one of the following form,

$$\frac{1}{GM^{1/2}} + 1 + GM^{1/2} \tag{6.27}$$

As pointed out for the linearly damped system by Thompson (1997), this expression suggests that we might increase critical wave slope by reducing GM to very low levels. This is misleading since we have failed to consider the dependence of θ_V on GM. We can crudely incorporate this factor by assuming a $\theta_V \propto GM$ relationship, giving the following basic dependence of critical wave slope on GM,

$$GM^{1/2} + GM^2 + GM^{7/2} \tag{6.28}$$

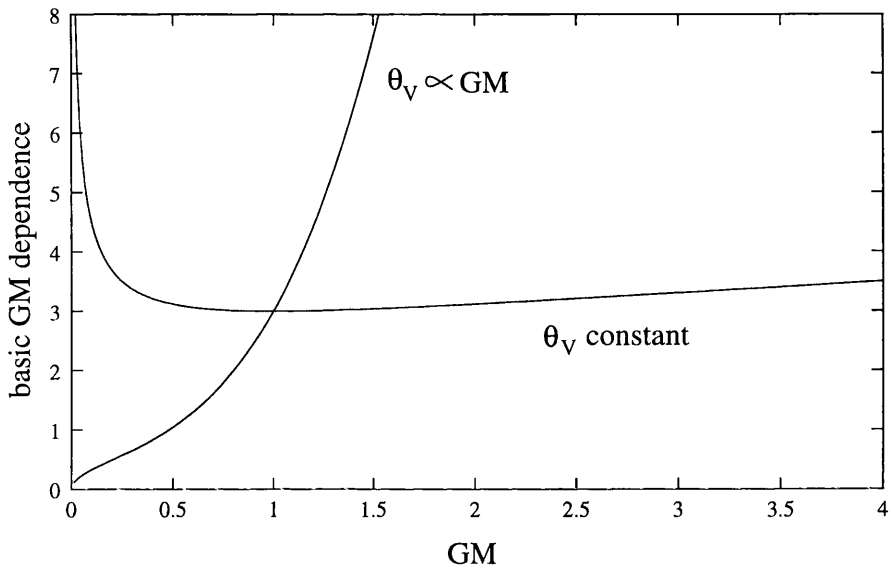

Figure 6.10: The basic dependence of critical wave slope on GM from the IDF.

These two functions are plotted in figure 6.10 and we can see from this how important the relationship between θ_V and GM can be.

6.5 Conclusions

In order to derive simple design formulae we wish to obtain an equivalent linear damping coefficient for capsize. Traditionally this is performed by choosing the linear system for which energy loss around an harmonic orbit is the same as that for the original system. This gives a linearly damped oscillator which is 'equivalent' when considering behaviour that is close to harmonic.

However if we wish to examine a phenomenon such as capsize, the trajectories we observe are not close to harmonic (Spyrou & Thompson 1998). There is therefore a need for a new 'equivalence' which can be used to model such features.

Here we have defined an equivalent linear damping using the Melnikov criteria, an approximate analytic method for determining capsize domains in parameter space. Effectively this involved balancing energy loss over a heteroclinic (or homoclinic)

orbit for the nonlinear and linearly damped systems. This concept has been used to obtain amplitudes for which the standard equivalent linear approach should be used. These corresponded well with the minima in a plot of the difference between equivalent linear and nonlinearly damped capsize.

Using the concept of a Melnikov equivalent damping, an improved design formula (IDF) has been developed. This replaces the linear damping of the simple design formula with the Melnikov equivalent damping. We have also discussed some implications of the form of the IDF and how it might be applied to a design process. For the IDF the forcing is tuned so that $\omega_n = \omega_f$ and the minimum seen for constant θ_V is not a resonance phenomenon. We have also pointed out the problems with solely considering variation in GM. In chapter 8 we test the IDF further, comparing it with experimental capsize tests.

Chapter 7

ROLL DECAY TESTS

7.1 Introduction

Deriving a good model for ship rolling requires effective characterisation of the various terms in the equation of motion. Even considering only the single degree of freedom roll model, this is not a simple procedure. While the restoring can be reasonably well modelled using a static approach, the significance of viscous effects means that the derivation of the damping term is empirical in nature. Similar problems are faced in the modelling of excitation, although empirical approaches can give good results (Contento, Francescutto & Piciullo 1995). Typically a low order nonlinear velocity dependent model for damping is fitted to roll decay data. By performing a number of different tests, under varied conditions, the damping model obtained is considered valid for most purposes.

A series of roll experiments was undertaken with a frigate model in order to better characterise the damping term at the high roll amplitudes close to capsize. As well as the significance of roll amplitude we were also interested in the effect of bilge keels and fins. Tests were performed with and without hull additions, for

normal and light displacement. Furthermore, the metacentric height was set at three different values, centred on the normal (scaled) GM.

We now present an analysis of these tests ,with a focus on the sources of nonlinear roll damping. Using an harmonic balance approach a simple expression is derived for equivalent nonlinear damping terms, giving the damping ratio, ζ, as a function of roll amplitude. By applying this formula to the calculated damping ratios we then reconstruct nonlinear damping functions for the different conditions.

7.2 Experimental details

Roll decay tests were performed at DERA Haslar, using a scale model frigate, the various conditionings of which are detailed in appendix B.1. Froude scaling was applied but to best capture the importance of viscous effects (particularly with respect to appendages), the largest practicable scale model (1/25) was used.

The tests were performed for normal displacement and a light displacement conditioning, with bilge keels and fins. For the normal displacement the tests were repeated without bilge keels and fins. The GM of the model was also set at 3 values; average, high and low, by varying the position of an aerial mass. The details can be found in appendix B.1. At least 2 runs were performed for each conditioning and the model was released from a number of different angles (e.g. above and below the downflooding angle).

Roll motion was measured using an on-board gyroscope, with the data from this read into a computer using an umbilical connecting cable. A sampling rate of 10Hz was used. The gyroscope was zeroed before every test. Records were checked after every test and bad runs were repeated.

7.3 Nonlinear analysis

Although for an approximate linear analysis of the roll equation, it is often convenient to use an equivalent linear damping term, for numerically based studies a nonlinear term provides more accuracy and is no more difficult to apply.

The basic approach used here to determine the nonlinear damping functions for the different conditions can be summarised:

1 find the damping ratio, ζ, for a certain roll cycle, giving ζ as a function of roll amplitude

2 use the amplitude dependence to determine a nonlinear damping function.

The first step uses the basic log decrement procedure, the derivation of which is repeated below. To perform the second step we must first derive a relationship between nonlinear damping and the equivalent linear damping. This can be done using a simple energy balance procedure.

Finding equivalent linear damping

We start with the linearised equation for free rolling,

$$I\theta'' + B_1\theta' + mgGM\theta = 0 \tag{7.1}$$

where the prime denotes differentiation with respect to real (unscaled) time, τ, I is the rotational moment of inertia about the centre of gravity, B_1 is the linear damping coefficient and $mgGM\theta$ is the roll restoring moment.

Equation (7.1) has the approximate solution, valid for light damping,

$$\theta = \theta_0 e^{-B_1 t/2I} \cos \omega_n t \tag{7.2}$$

where $\omega_n = 2\pi/T$ is the natural roll frequency. If we look at two consecutive maxima, θ_i and θ_{i+1} (i.e. one natural period apart) we find

$$\theta_{i+1} = \theta_i e^{-B_1 T/2I} = \theta_i e^{-\pi B_1/I\omega_n} \tag{7.3}$$

Finally we can then write

$$B_1 = \frac{I\omega_n}{\pi} \ln \frac{\theta_i}{\theta_{i+1}} \tag{7.4}$$

Alternatively the damping ratio is

$$\zeta = \frac{B_1 \omega_n}{2mgGM} = \frac{1}{2\pi} \ln \frac{\theta_i}{\theta_{i+1}} \tag{7.5}$$

which, as we are finding it for each cycle, is also a function of roll amplitude over that cycle. It is this dependence on amplitude which enables us to fit a nonlinear damping function to the data by applying the following method.

Finding the nonlinear damping coefficients

Firstly we rewrite our roll equation (7.1) to include nonlinear damping;

$$I\theta'' + B_1\theta' + B_2|\theta'|\theta' + mgGM\theta = 0 \tag{7.6}$$

where we have chosen a linear plus quadratic damping term.

To simplify the following derivation, we now re-write (7.6) in non-dimensional

form;

$$\ddot{x} + b_1\dot{x} + b_2|\dot{x}|\dot{x} + x = 0 \tag{7.7}$$

where, $x = \theta/\theta_V$, the derivatives are now with respect to rescaled time, $t = \omega_n\tau$ and the damping terms are scaled in the following manner;

$$b_1 = \frac{B_1}{\omega_n I} \qquad b_2 = \frac{B_2\theta_V}{I} \tag{7.8}$$

Taking a harmonic solution, $a\cos t$, and equating the energy loss from damping with the drop in potential energy over one cycle ($x_i \to x_{i+1}$) we find

$$\Delta PE = a\Delta a = \int_{x_i}^{x_{i+1}} \left(b_1 a \sin t + b_2 a^2 |\sin t| \sin t\right) dx \tag{7.9}$$

$$= 2\int_0^{\pi} \left(b_1 a^2 \sin^2 t + b_2 a^3 \sin^3 t\right) dt \tag{7.10}$$

where a is the amplitude and ΔPE is the change in potential energy from peak to peak ($x_i \to x_{i+1}$). Note that we are essentially viewing the decay (decrease in a) as occurring in steps every cycle.

Solving the integrals and cancelling a with x_{i+1} then leads to

$$\frac{x_i}{x_{i+1}} = 1 + \pi b_1 + \frac{8b_2 a}{3} \tag{7.11}$$

Thus, using the definition of ζ in (7.5) we can write

$$\zeta = \frac{1}{2\pi} \ln \left[1 + \pi b_1 + \frac{8 b_2 a}{3} \right] \tag{7.12}$$

$$\approx \frac{1}{2\pi} \left[\pi b_1 + \frac{8 b_2 a}{3} \right] \tag{7.13}$$

Finally we can now rewrite this in terms of the real roll amplitude, $A = a\theta_V$;

$$\zeta(a) = \frac{\beta}{2} + \frac{4 b_2 a}{3\pi} \tag{7.14}$$

$$\Longrightarrow \zeta(A) = \frac{\beta}{2} + \frac{4 b_2}{3\pi\theta_V} A \tag{7.15}$$

This is the formula needed to derive the damping coefficients, b_1 and b_2, from the slope and intercept of a $\zeta(A)$ best fit line.

7.4 Application to the roll decay data

Figures 7.1 and 7.2 show the ζ values plotted against the mid cycle amplitude, for the normal displacement conditioning[1]. In obtained these points we have actually considered the decay over a whole cycle. During the large angle tests it was frequently found that a little water entered the hull, causing a small bias in restoring. This problem was solved simply by considering the whole cycle.

From this simple analysis two main observations are made;

- the addition of appendages has a dramatic effect on ζ for *high and low amplitude* rolling (i.e. even with no bilge keel splashing)

[1] In appendix B.2 we present a list of all the tests performed and the mean ζ values calculated for the free roll tests. We look at the high gain ($\theta < 8°$) and low gain data separately. Note that some runs have been excluded due to poor quality data.

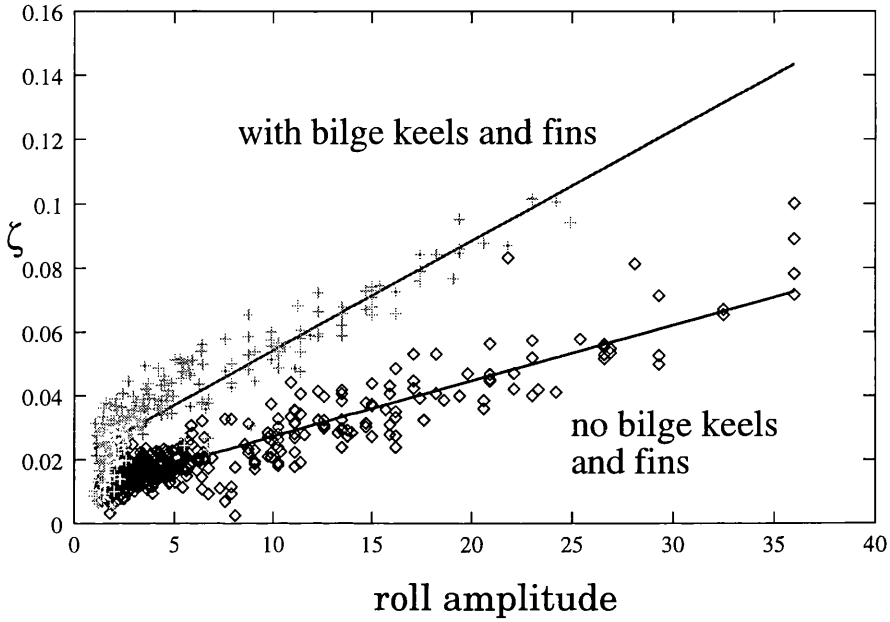

Figure 7.1: Average displacement $\zeta(A)$ (with and without appendages) plotted against mid-cycle amplitude, A (in degrees).

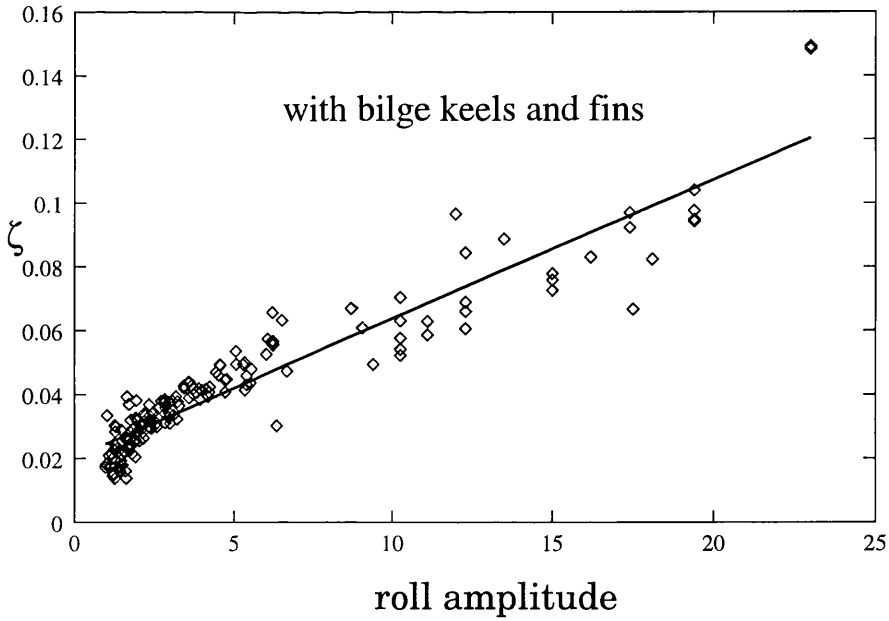

Figure 7.2: Low displacement ζ with appendages plotted against mid-cycle amplitude, A (in degrees).

- The strong dependence of ζ on A (with or without appendages) highlights the inadequacy of the linear roll damping model for general roll motion.

Best fit lines have been fitted through these values and from these we can recover the nonlinear damping functions. Comparison of the intercept and slopes of the best fit lines and the application of (7.15) gives the non-dimensional damping coefficients, b_1 and b_2. Using (7.8) these can then be rescaled into real damping coefficients for the scale model frigate.

This gives the following functions for the three conditions (the different GM conditions are not considered separately as this parameter should not affect the real damping levels).

Table 7.1: Damping coefficients

conditioning	b_1	b_2	B_1	B_2
avg displacement	0.022	0.29	0.815	2.862
avg displacement+BKs	0.033	0.74	1.222	7.194
low displacement+BKs	0.033	0.85	1.215	8.091

These damping functions are plotted in figure 7.3 where $B(\theta') = B_1\theta' + B_2|\theta'|\theta'$. The nonlinear damping term becomes more important when the appendages are in place. The effects of this nonlinear damping on capsize have been explored in chapter 6.

7.5 Validation

In order to show that the nonlinear damping functions obtained from the data are a good representation of the real damping, three numerically generated decay curves were compared with the original decay data. For the numerical model, the

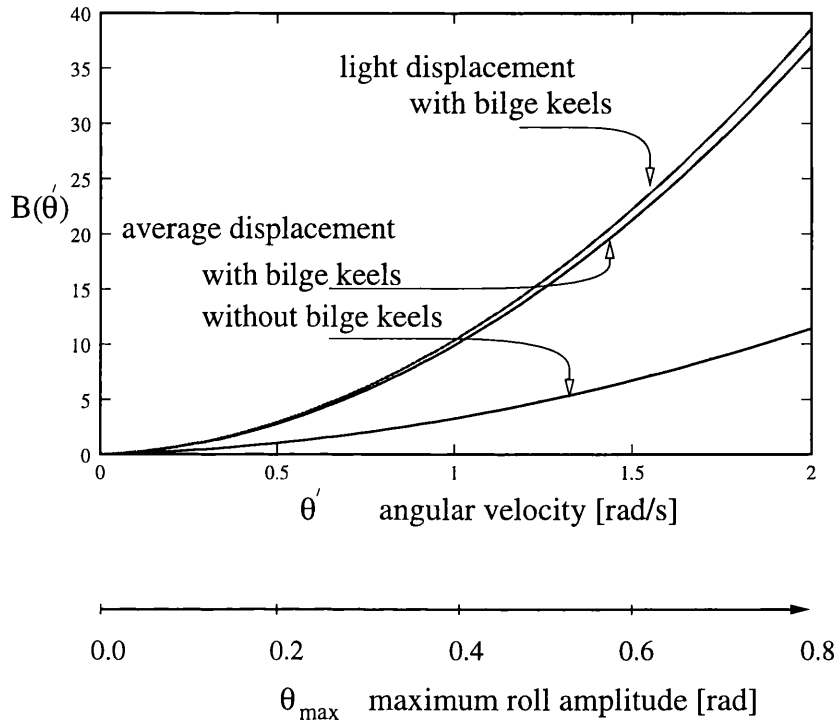

Figure 7.3: Damping functions, $B(\theta') = B_1\theta' + B_2|\theta'|\theta'$, for 3 different conditions. While displacement makes little difference, it is clear that the effect of appendages in considerable.

appropriate restoring and moments of inertia were used, along with the calculated damping coefficients for the particular model conditioning. The added mass was varied in a practical range in order to fit the roll frequencies correctly. Basically this meant choosing I such that

$$\omega_n = \sqrt{\frac{mgGM}{I}} \tag{7.16}$$

where ω_n and $mgGM$ were measured values.

In figures 7.4 to 7.9 the low and high gain decay data for runs 19, 38 & 45 are plotted with the numerically generated data superimposed.

In figures 7.4 & 7.5 the actual and numerically generated decay curves are almost indistinguishable, indicating that the damping functions obtained are a good model for the damping.

Average Draught with no Appendages

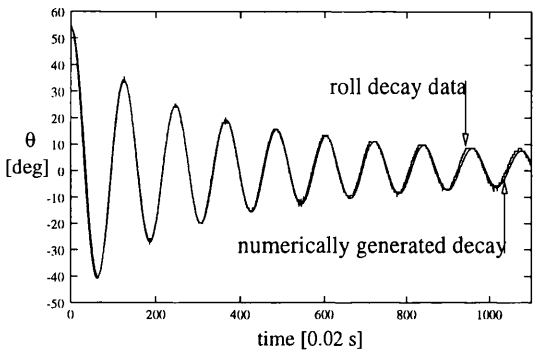

Figure 7.4: A good fit has been obtained for the low gain data, with any small discrepancies attributable to slight inaccuracies in the restoring or moment of inertia figures used for the numerical model.

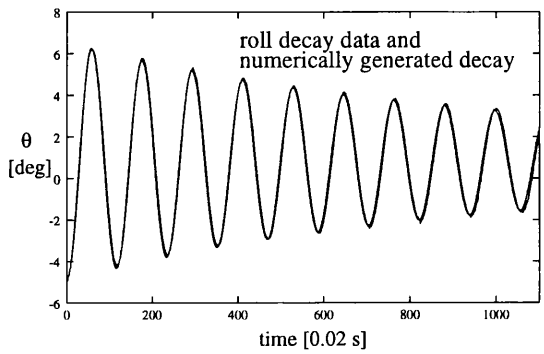

Figure 7.5: Here the high gain data is plotted with the numerically generated data. The calculated damping functions again provide a good fit.

Average Draught with Appendages

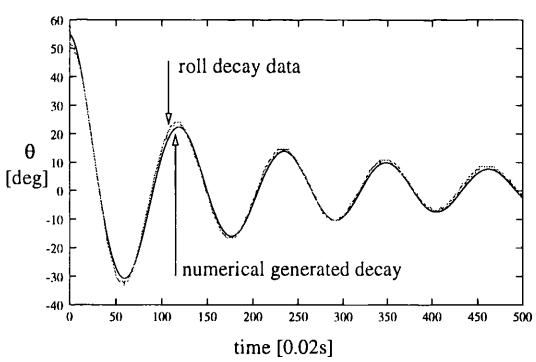

Figure 7.6: With the presence of appendages, the fit for the high gain data (large roll amplitudes) is again good.

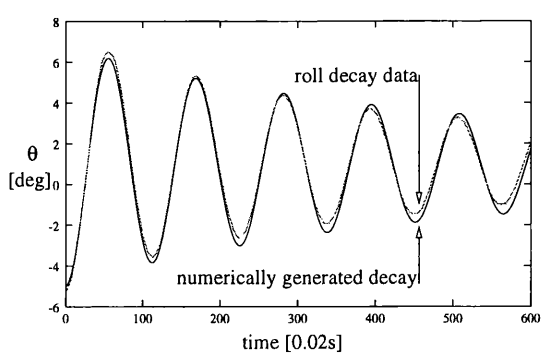

Figure 7.7: Here the high gain data is plotted with the numerically generated data and here the curves start to differ as the roll amplitude decays.

Low Draught with Appendages

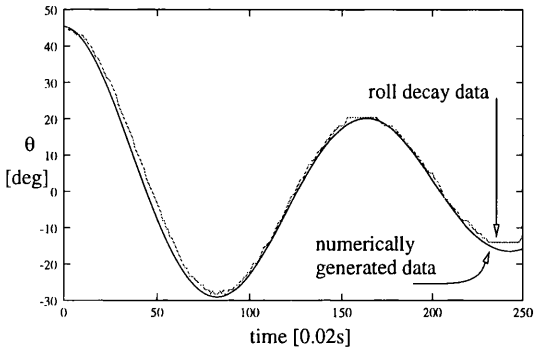

Figure 7.8: With the presence of appendages, the fit for the high gain data (large roll amplitudes) is good for the low draught condition.

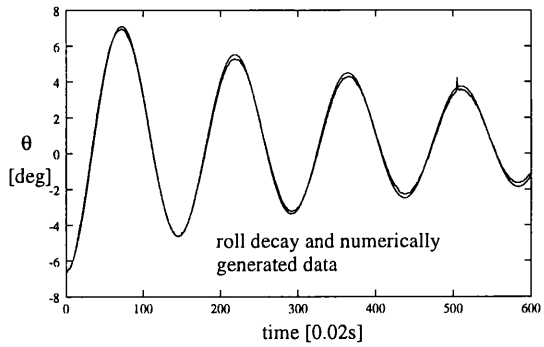

Figure 7.9: Here the high gain data is plotted with the numerically generated data.

The fit for figure 7.7 is noticeably worse than for the other cases. This can be attributed to the increased nonlinearity of the underlying damping function due to the presence of appendages. The greater the nonlinearity in the damping, the less effective a function with only two parameters is over a wide range of roll amplitudes. As a consequence the decay curves fit better for the high roll amplitudes in figure 7.6 than for the lower amplitudes in figure 7.7. This effect is less pronounced for the low draught case.

7.6 Conclusions

This series of large angle roll decay tests has highlighted the importance of nonlinearity in the damping, as well as helping to identify the source of the nonlinearity. The effect of bilge keels and fins is dramatic, causing a significant increase in the nonlinear damping coefficients. We can obtain a general idea of the effect this has on capsize by looking at the improved design formula (IDF), table 7.2. In this table the predicted critical wave slope from the IDF for quadratic and cubic restoring models are shown for the three conditionings. It is clear that the increase

Table 7.2: The effect of bilge keels on the IDF

conditioning	**IDF** (**wave slope**) quadratic	cubic
average displacement, with BKs	0.53	0.63
average displacement, no BKs	0.22	0.26
light displacement, BKs	0.63	0.76

in nonlinear damping caused by the bilge keels and fins (BKs) is very significant. Given that a breaking wave has slope $Ak \approx 0.44$, we can see how important such appendages might be. This brief analysis also nicely demonstrates the use of the improved design formula to provide an indication of the effect of such alterations to a hull.

Chapter 8

CAPSIZE EXPERIMENTS

8.1 Introduction

In recent years considerable progress has been made in the nonlinear modelling of ship capsize. Our understanding of the capsize process has been greatly enhanced by these advances, discussed at length in this thesis. However, there remains a lack of experimental work in this field, see for instance the studies of Contento & Francescutto (1997). A series of experiments were therefore performed to test the theoretical predictions, placing particular emphasis on the nonlinearities in the system and capsize. These tests took place in the UCL Civil Engineering Laboratory's wavetank, using a simple prismatic model, based upon a design from Wright & Marshfield (1980).

As a prelude to the roll experiments, some testing of the waves generated by the UCL wave tank was performed. We now examine the observed wave fronts and accompany this with numerical tests of a simple wave front model, the primary aim of which is to ascertain the significance of the way in which the wave builds up. The results of this wave modelling and the implications for the capsize tests

are then discussed in the first part of this chapter.

We begin the analysis of the capsize tests with a resonance response diagram, which with a bistable region, displays the nonlinear nature of the system. The results of a set of transient capsize tests are then compared to the improved design formula, bifurcation theory and numerical simulations. The existence of bias and its implications for modelling capsize are discussed with reference to the experimental evidence.

One of the key features of nonlinear systems is a sensitivity to initial conditions. This has considerable significance for the experimental testing of new designs and during our capsize tests was observed to be quite a typical feature. By starting the wavemaker paddle from different positions we were able to vary the wave build up and thus vary the initial conditions of the system. We could then observe the effect of this upon capsize. In section 8.6.1 we present some roll records which show the importance of such initial conditions in determining the outcome of transient roll.

Finally we also use the experimental model as an example for the application of the improved design formula to design. Using this approach it is possible to determine how a key parameter, such as GM, the metacentric height, may affect capsize.

8.2 Experimental details

The experiments were conducted in a wave tank of length 8.9m and width 0.585m and a water depth of 0.5m, with a vertical paddle wave maker, see figure 8.1. A wire mesh was placed in front of the paddle to damp out high frequency 'ripples' on the wave surface. The throw, being the amplitude of the paddle motion, controlled the height of the wave although this was also dependent on the frequency. The wave frequency was controlled by varying the paddle oscillation frequency. In

order to measure the height and frequency of the wave, we employed a wave probe connected to a computer for data acquisition, at a sampling rate of 30 Hz[1]. The wave probe was positioned 1.5m from the wavemaker and 0.5m in front of the model, see figure 8.1. The model was free to drift and this led to the encounter frequency varying a small amount, but since the drift speed was much lower than the wave celerity this effect was negligible.

Some limitations existed in the generation of large amplitude, long period waves and we have considered only deep water conditions ($d > 0.5\lambda$).

The roll angle was measured with a $\pm 50°$ inclinometer situated inside the model (again sampling at 30 Hz). The inclinometer was tested to ensure that the lateral accelerations likely to occur would not have a significant effect on the measured roll angle. An umbilical cable for data acquisition was held loosely above the model to minimise any effect on the rolling.

We wished to maximise damping of the waves at the beach thus minimising interference from reflected waves. The effect of reflections is to cause modulations in the wave amplitude once steady state is reached. These modulations were, however, quite small compared to the wave amplitude. When considering the wave height (or slope) for capsize, we recorded the mean of the steady-state wave while also noting the maximum height achieved. The effect of ramped forcing and initial peak wave heights on capsize is discussed in section 8.3.1.

8.3 Propagating wave front in tank tests

The transient studies described in chapter 3 imply that the direct roll excitation is sudden stepped, at time zero, to its full sinusoidal form. This is an extreme form of

[1]LabView data acquisition software was used to both acquire and manage the data.

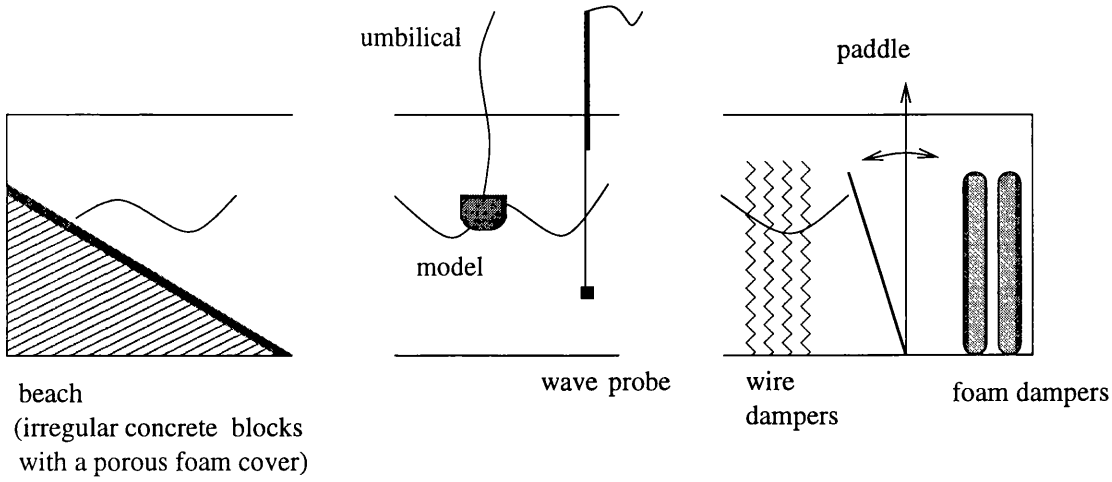

Figure 8.1: The wavetank

transient loading which could never be encountered at sea, and which can never be produced in a laboratory tank test. As a prelude to roll tests in the UCL wavetank it was therefore necessary to make some further studies on a more realistic wave build up. In particular we were interested in a boat in ambient conditions excited by the natural wave front propagating from a nearby wave-maker that had just been switched on. The roll excitation then built up rapidly but smoothly to its maximum amplitude. This form of loading is intermediate between the stepped sinusoid and that of a steady-state test in which the forcing magnitude would be increased very slowly, since the boat has only a short time to adapt its rolling motion to the oncoming waves. We are interested in how this might affect our capsize modelling and transient capsize diagrams in particular.

8.3.1 Naturally propagating waves

While the inclusion of monotonic wave increase brings the forcing somewhat closer to reality the importance of an initial (greater than steady state) wave steepness cannot be ignored when fitting a model to test results. Here we present some wave data, figure 8.2, obtained from the UCL wavetank.

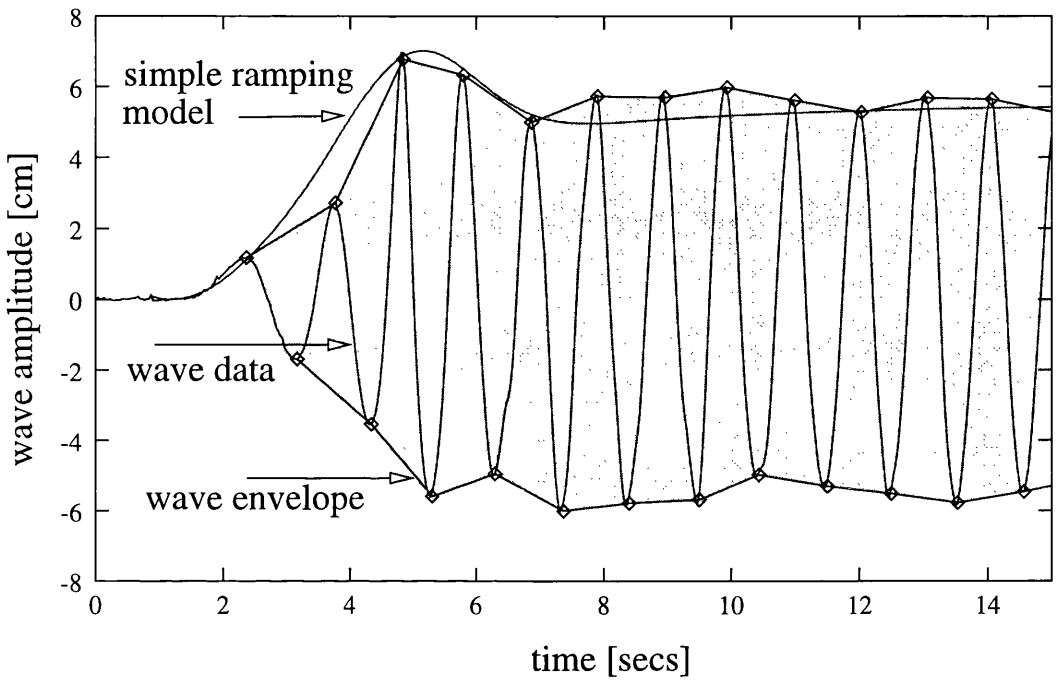

Figure 8.2: Wave build up after wave maker is switched on. Note that the speed of wave increase and size of the initial peak will vary with distance from the wave source and the steady-state height and frequency settings.

It can be seen that the wave envelope does not increase monotonically and instead reaches a peak amplitude before decreasing to the steady state heights. If a transient capsize diagram is to be experimentally realised, then the significance of this feature must first be tested. In order to do this we develop a simple model for wave build up which incorporates an initial peak wave height.

While it is possible to derive a theoretical model for a wavefront which incorporates the initial peaks seen in figure 8.2 (Mei 1989), the result is expressed using Fresnel cosine and sine integrals which are difficult to incorporate into the model. As a result a simple model for natural wave propagation, which retains the features we wish to capture, is used. Nondimensional forcing amplitude is now written as the following function of time

$$F(t) = F_0 \left[t^2/(1+t^2) + \mu e^{-k(t-n)^2} \right] \sin(\omega t) \tag{8.1}$$

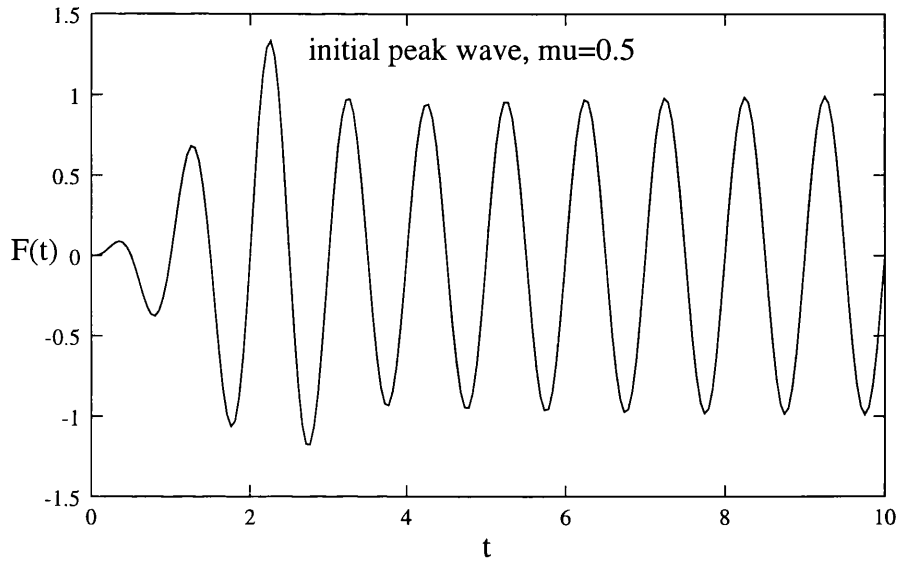

Figure 8.3: A simple model for a ramped wave front, with $\mu = 0.5$. The ramping shown here is used to generate a transient capsize diagram, plotted in figure 8.6. It shares many of the characteristics of the observed wave build up.

where F_0 is the steady state forcing amplitude, μ the peak height, k the peak width and n governs the peak position. By allowing time to be scaled we may also vary the rate of the wave build up, thus providing a great deal of flexibility over our modelling of the wavefront. This function may be fit to experimental wave data, as shown in figure 8.2, or used within a nondimensional context. The advantage of writing the ramping in this way is that we can vary μ and study the importance of the initial peak height for our capsize modelling.

In the following tests we choose the fitting parameters such that the number of waves before the peak (approximately 3) is roughly the same as that observed in the UCL wave tank. We wish to capture the important aspects of the wave propagation, namely;

1 initial monotonic increase in wave envelope

2 peak in wave envelope

3 decay to steady state amplitude

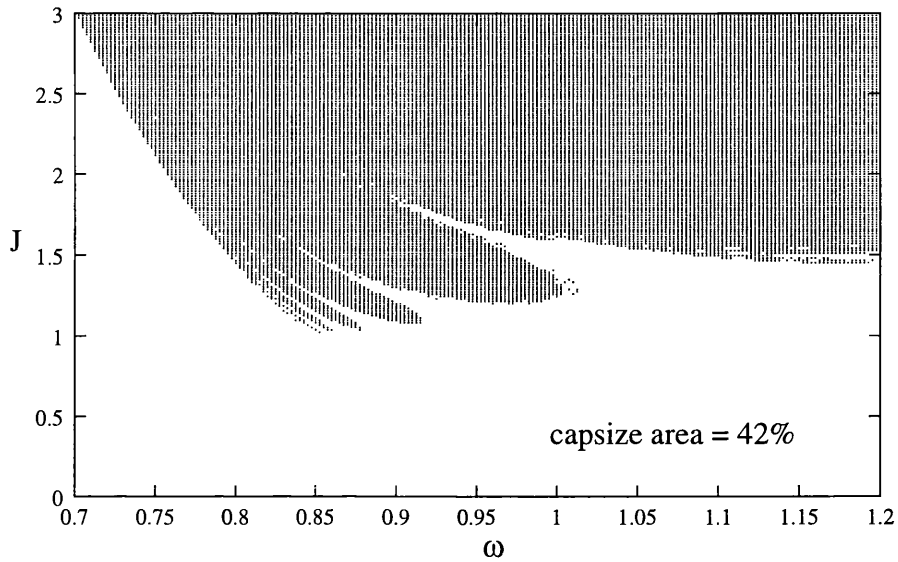

Figure 8.4: Transient capsize for a stepped sinusoidal wavefront. For comparison, 42% of the grid of control parameters caused capsize.

Note that this model does not take into account the reflection induced envelope modulation seen in the wave tank data.

8.3.2 Transient capsize under ramped forcing

We can now investigate the significance of ramping and an initial peak wave on the transient capsize diagrams detailed in chapter 3. Following our previous studies, we have used the linearly damped asymmetric roll model, (2.8).

Plotted in figures 8.4 to 8.6 are transient capsize diagrams for stepped, ramped and ramped with an initial peak forcing respectively. Importantly, these plots show little difference around resonant forcing frequencies, with the minimum points all around $J = 1$ (the simple design formula prediction).

In particular we find that the stepped sinusoidal forcing, figure 8.4 gives very similar results to the peak wave model, with the 'capsize areas' of similar sizes. This supports our use of the stepped sinusoidal approach to wave modelling.

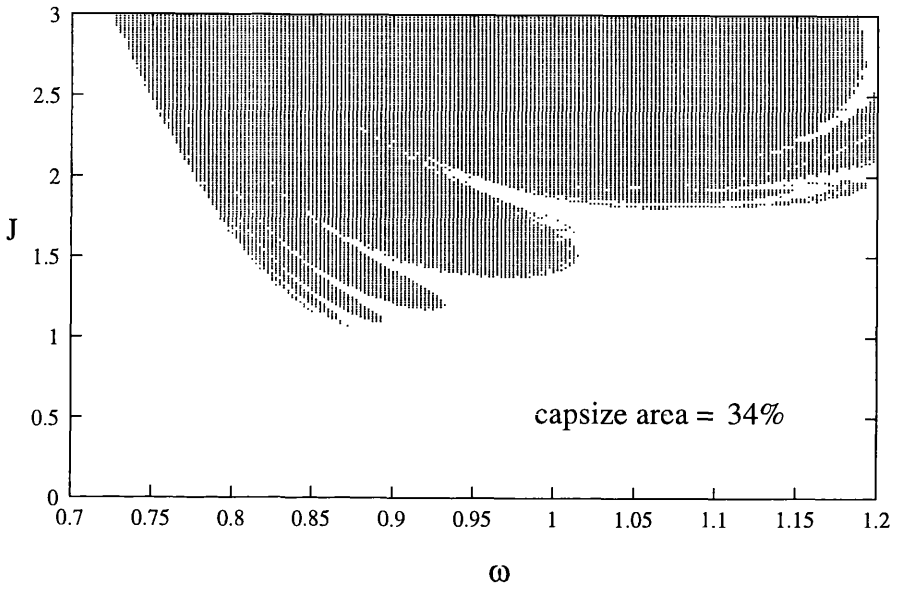

Figure 8.5: Transient capsize for a ramped wavefront with no initial peak, $\mu = 0$.In this case 34% of points caused capsize.

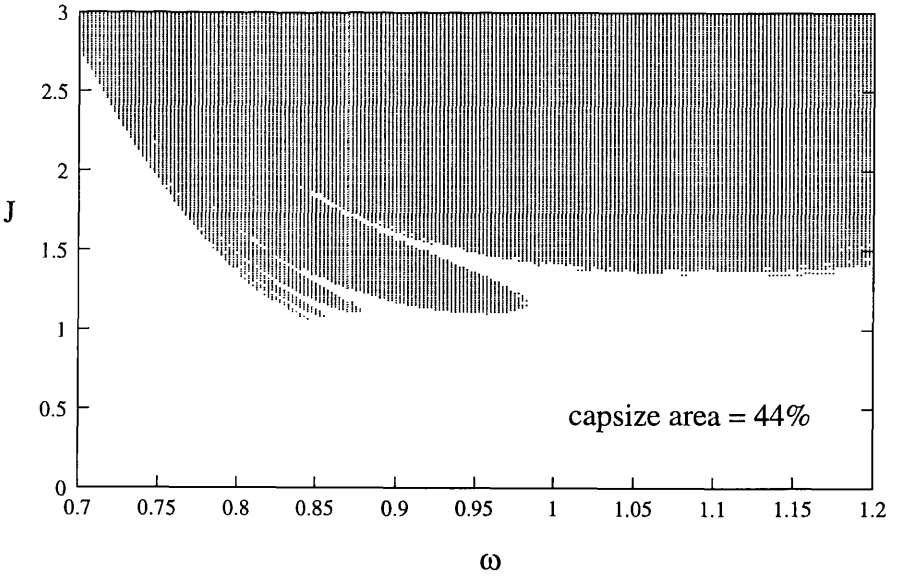

Figure 8.6: Transient capsize for a ramped wavefront with an initial peak of similar scale to that observed in the wavetank, $\mu = 0.5$. Here, 44% of the points caused capsize.

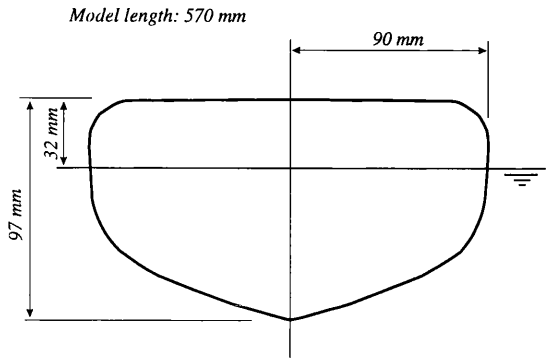

Figure 8.7: Cross-section of model hull.

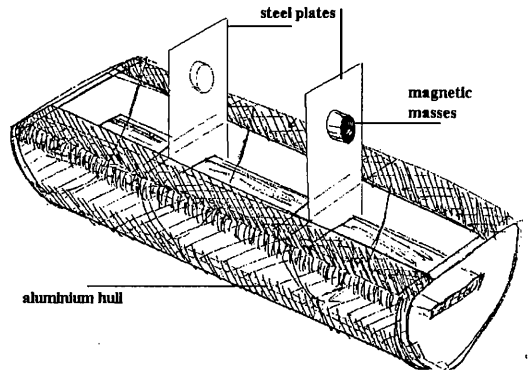

Figure 8.8: Sketch of model arrangement.

8.4 The experimental model

As the objective was to derive the capsize boundary, the model design was based upon the low freeboard hull used by Wright & Marshfield (1980), for which capsize tests had been successfully made. The actual hull form chosen was Form 1, section 9 (see figure 8.9), since midships was too close to a square cross-section. We also required a suitable size for the waves we could generate (i.e. for roll motion equation to be valid we require the cross-section to be small compared to wave length) . Furthermore, GM was chosen to ensure that capsize was achievable and that a range of ω_f values around resonance were available. Easy variation of model parameters was desired and the use of magnetic masses meant that GM and natural frequency were easily altered. Finally it was found that by leaving minimal clearance between the ends of the model and the sides of the tank, yaw motion was suppressed without contact being made. In figure 8.10 we show a photo of the model rolling in response to a low amplitude wave.

In order to compare our test results with numerical and theoretical studies we firstly measured the parameters defining our test model for the single degree of

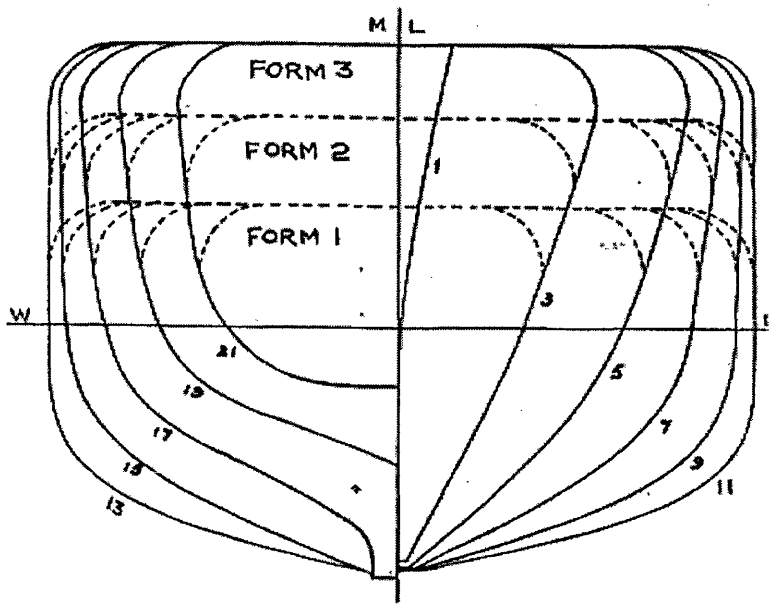

Figure 8.9: Lines plan of model reproduced from Wright and Marshfield (1980).

freedom roll equation;

$$I\theta'' + B(\theta') + mgGZ(\theta) = IAk\omega_f^2 \sin \omega_f \tau$$

where, as before, the prime denotes differentiation with respect to real (unscaled) time, τ, I is the rotational moment of inertia about the centre of gravity, θ is the roll angle relative to the wave normal, $B(\theta')$ is the nonlinear damping function, $mgGZ(\theta)$ is the roll restoring moment, Ak is the wave slope amplitude (A is the wave height and k the wave number) and ω_f is the wave frequency.

More specifically we needed to perform roll decay and GZ tests to determine $B(\theta')$ and $GZ(\theta)$. The moment of inertia I (including added mass) was derived from the natural frequency.

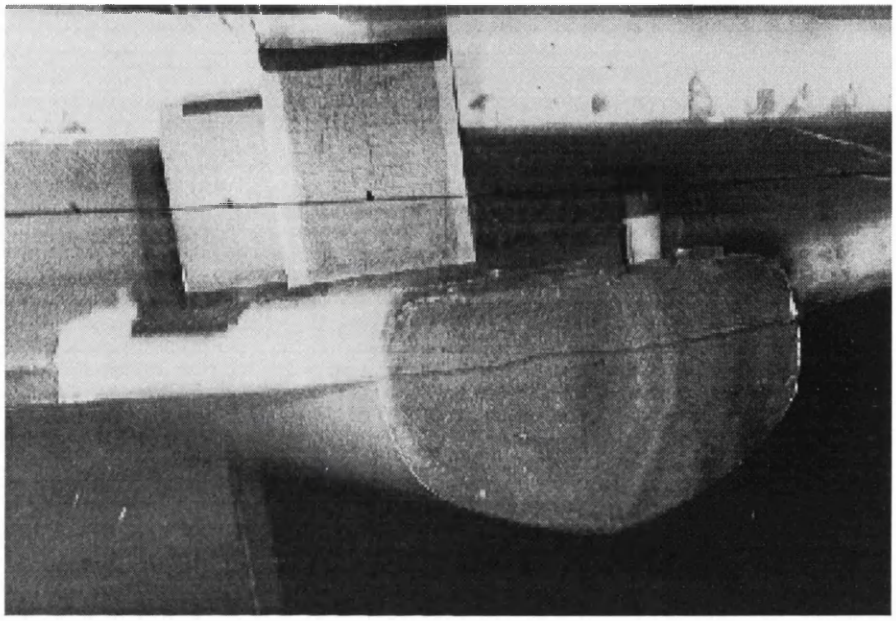

Figure 8.10: Photo of model rolling in response to a low amplitude wave.

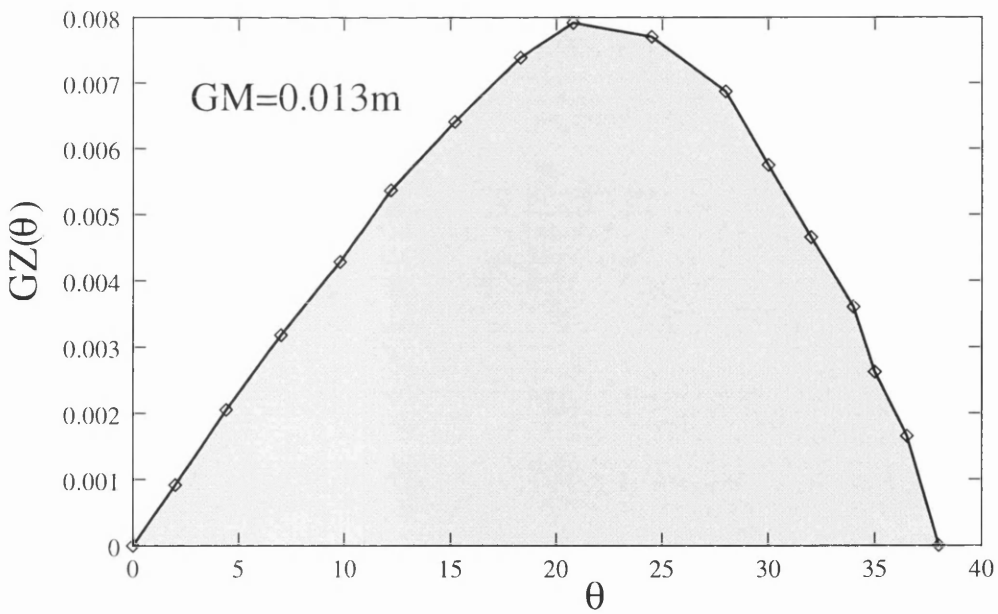

Figure 8.11: The GZ curve for the model.

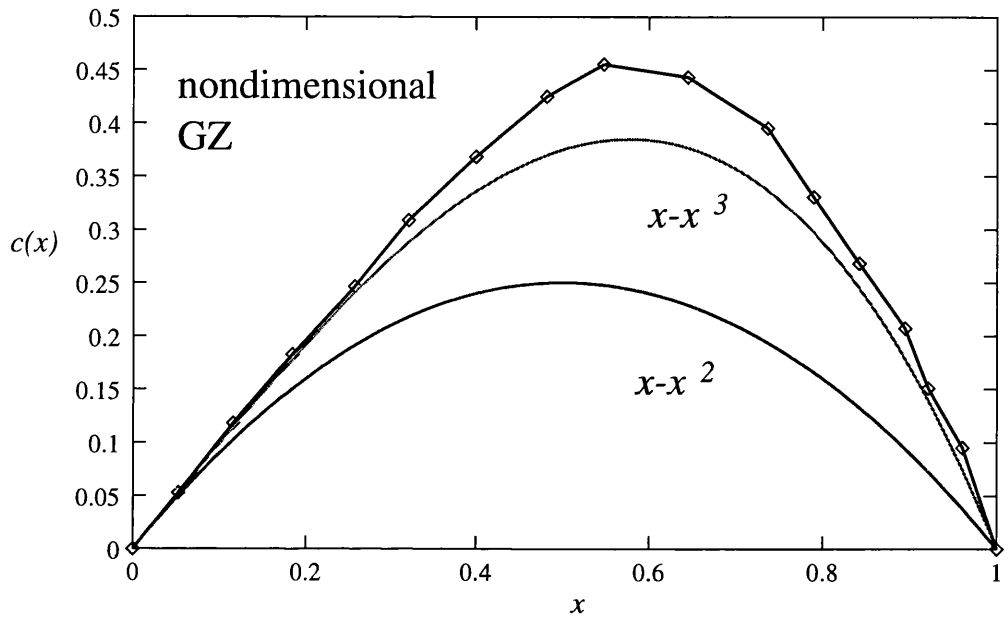

Figure 8.12: The non-dimensional GZ curve for the model, conditioned as for the capsize tests.

8.4.1 Model GZ

The GZ curve was determined by moving the magnetic weights and measuring the applied moment and induced heel angle. To obtain the GZ for angles beyond the maximum righting arm, the model was balanced at the unstable equilibrium point. A number of tests were made, and the GZ obtained is plotted in figure 8.11. For comparison we also show, in figure 8.12, the non-dimensionalised GZ curve, along with the quadratic and cubic restoring models we have frequently used in the theoretical studies in this thesis. Note that $x - x^3$ gives a better fit to the GZ curve than $x - x^2$. In section 8.6 we examine how these two possible fits to the restoring perform when we try to predict capsize.

8.4.2 Measurement of roll-damping

To calculate the damping coefficients we performed decay tests with the model conditioned as for the capsize tests.

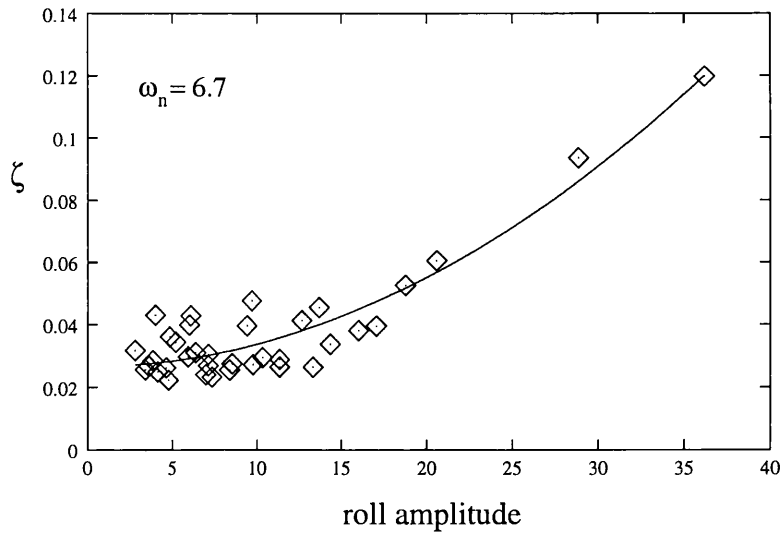

Figure 8.13: Equivalent linear damping, ζ plotted against the roll amplitude at the start of each cycle with GM set as for the capsize tests. A series of tests were conducted and the data from one of these is reproduced here.

In figure 8.13 we show the equivalent linear damping, ζ, plotted as a function of roll amplitude (see chapter 7 for a similar approach, based on the much larger frigate model). The data is taken from two tests with the same model parameter settings. The ζ values have been plotted against the amplitude at the start of each roll cycle. In total, 6 tests of this kind were performed.

Table 8.1: Damping coefficients

ω_n	b_1	b_3	$\zeta(\approx 0.5\theta_v)$	ζ^M
6.7	0.063	0.26	0.05	0.077

We assume the model has a (non-dimensional) nonlinear damping function of the form $b_1\dot{x} + b_3\dot{x}^3$ (in this case this was found to give a better fit to the data than the quadratic damping model). We can then obtain the coefficients b_1 and b_3 using the same method detailed in chapter 7 and shown in table 8.1.

Included in the table above is the equivalent linear damping at roll amplitudes of approximately $\theta_V/2$ and also the Melnikov equivalent damping, ζ^M. The latter figure is somewhat larger since it takes full account of the high amplitude motions

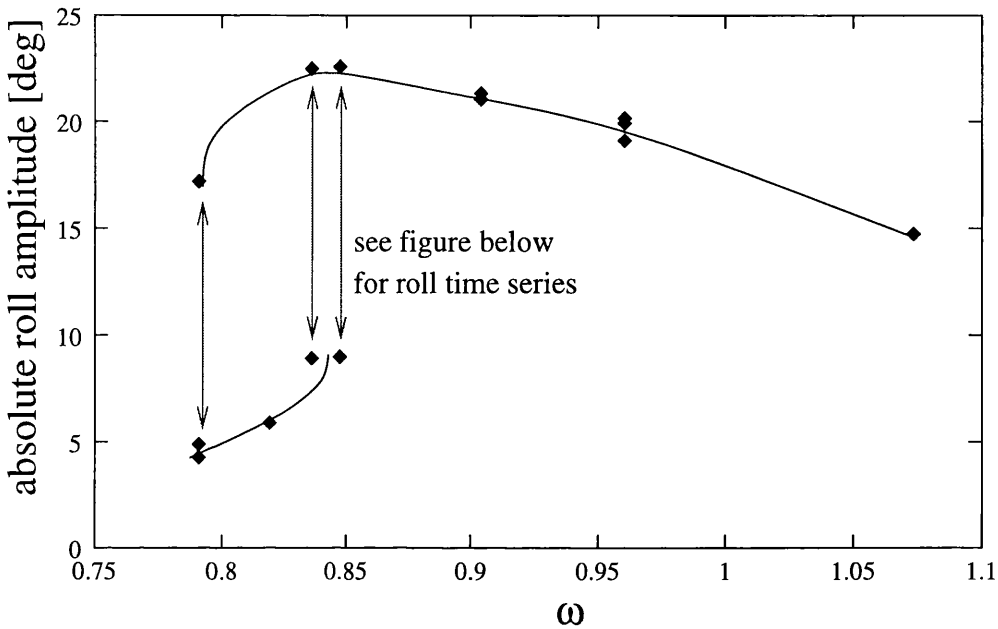

Figure 8.14: A frequency response diagram, plotted to show the nonlinear nature of the system. Two possible solutions exist just below resonance.

prior to capsize, at which damping levels tend to increase considerably. In deriving the Melnikov equivalent damping we have used the cubic model for restoring, see equation (6.23).

8.5 Resonance response

In order to better characterise the system before conducting the capsize tests, a resonance response test was made. This was evaluated by sweeping through a range of frequencies at fixed paddle throw. Throw was chosen to be held constant due to the difficulty of selecting a particular amplitude or wave slope with the paddle controls. The chosen position for the magnetic masses gave the natural frequency of the model as $\omega_n = 6.7s^{-1}$.

In figure 8.14 we show a resonance response plot which, with two steady-state solutions existing for the same wave frequencies, clearly displays the nonlinear

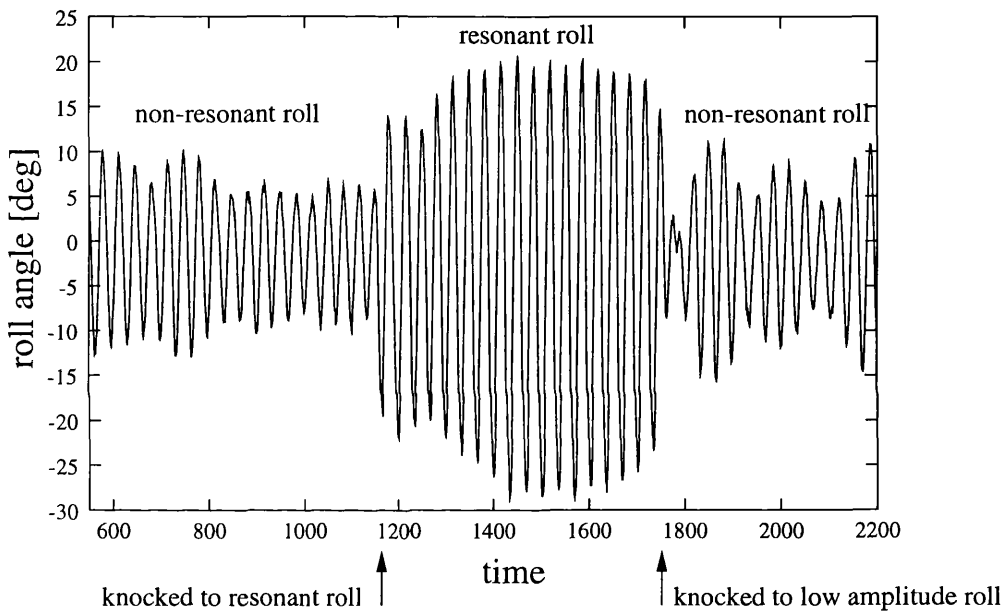

Figure 8.15: Two coexisting solutions for roll motion. The model was successfully knocked from one to the other a number of times: this plot shows this occurring twice; at $\tau \approx 1150$ and $\tau \approx 1750$. The modulation of the roll motion is due to the wave forcing modulation, an unavoidable result of the limited wave tank length. The wave for this test had a mean amplitude of $A = 0.035$m and frequency $\omega_f = 5.7s^{-1}$. The frequency ratio was therefore $\omega = 0.85$ and the mean wave slope $Ak = 0.11$.

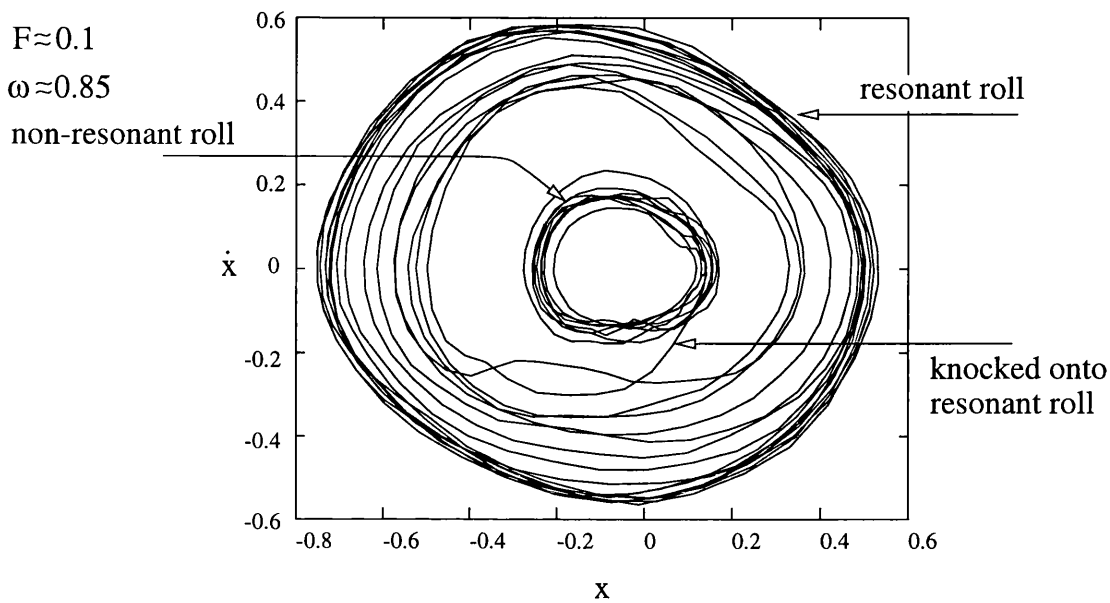

Figure 8.16: Phase space portrait of the two coexisting solutions for roll motion. The absolute roll angles have been transformed into nondimensional form by dividing through by θ_V. After several low amplitude roll cycles the model was knocked onto the resonant roll mode (onto which it takes several cycles to settle). Notice the significant bias towards the wave (in this case, negative x).

nature of the system. Also note the shift in the resonance peak to lower frequencies, as expected for a softening system (linear resonance is at $\omega = 1$). Note that, since wave slope increases with frequency, the roll amplitude remains large for high ω.

A time series in which the roll motion is knocked from large to small angle roll (and vice versa) is displayed in figure 8.15. Although some modulation (due to the modulation of the wave) is evident, the existence of two solutions can be seen and the model was knocked[2] between the two types of motion a number of times. Part of this time series is plotted as a phase portrait in figure 8.16. Transformed into nondimensional form, the phase portrait can be compared to the numerical simulation of figure 3.3 (in this case the bias is in the opposite direction and damping is higher). As can be seen in figure 8.14, this behaviour was observed over a range of wave frequencies.

[2]The model was perturbed from the steady-state oscillation and into the basin of attraction of an alternative steady-state oscillation, using a shock excitation

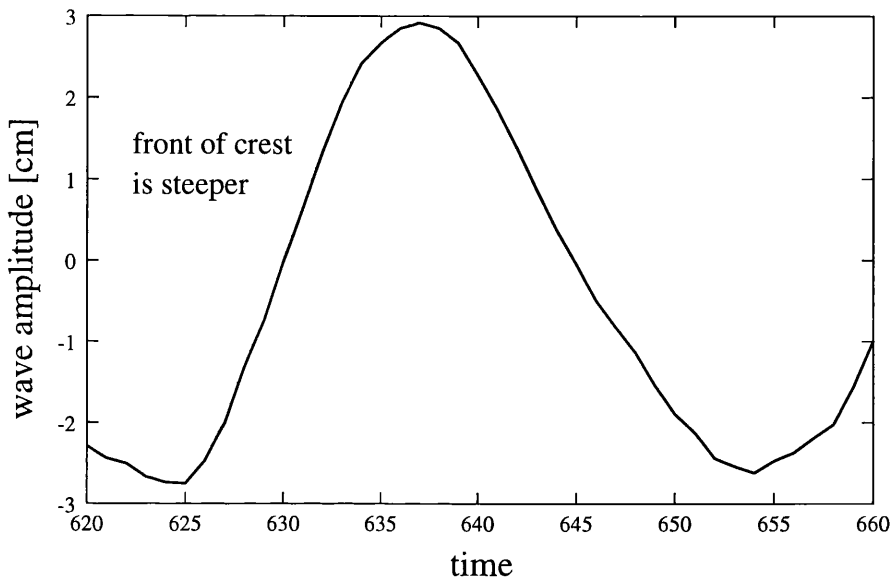

Figure 8.17: One wave with frequency close to that of the natural frequency of the model. The asymmetry in the wave form is visible in terms of the steepness either side of the crest.

It is also worth noting from figures 8.15 and 8.16 that there is significant bias in the response. This feature is particularly evident in the resonant motion, but was observed throughout the tests. The model itself was set up carefully to be symmetric in its static response and furthermore, when rotated by 180° the bias remained in the same direction, namely towards the wave. Hence, the bias in the response must have been due to asymmetry in the forcing, either from the shape of the waves or second order forces (drift effects). This aspect is certainly a very interesting topic for future research. Shown in figure 8.17 is one characteristic wave at a frequency around resonance. The front of the crest is visibly and quantitatively steeper, certainly one source of bias in the system. This feature was seen over all frequencies and amplitudes.

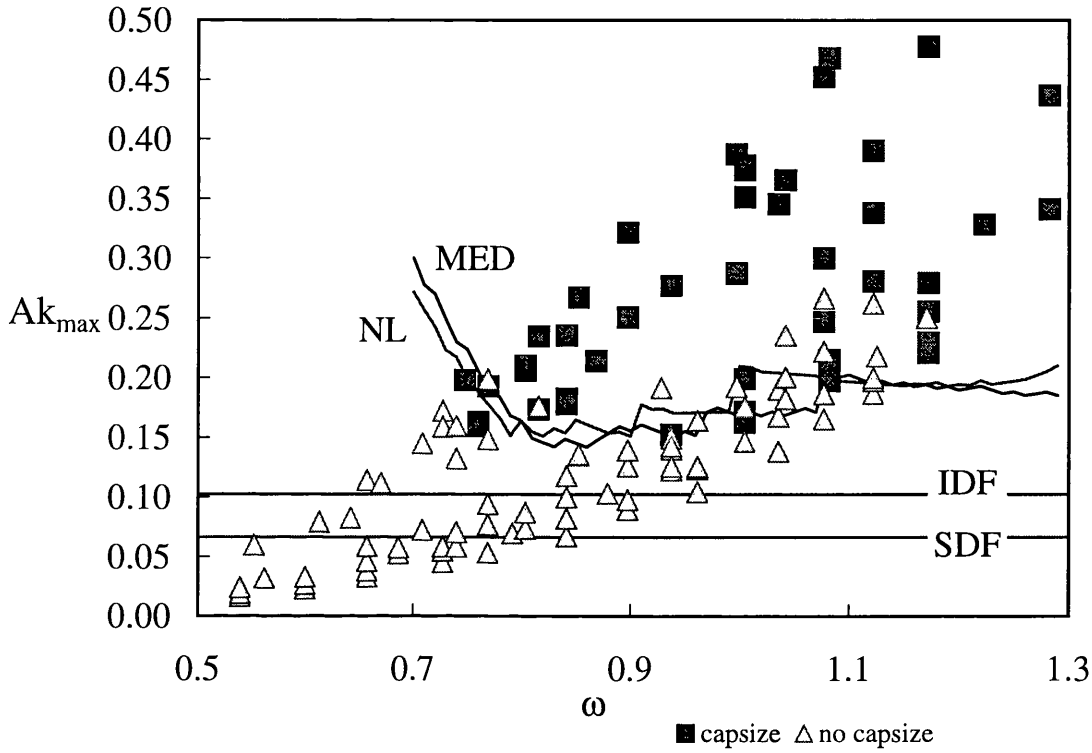

Figure 8.18: Transient capsize diagram from UCL tests. Superimposed are the numerically derived transient capsize boundaries using the full nonlinear damping and Melnikov equivalent damping. The measured GZ curve was used for both these numerical simulations. Also shown are the predictions from the simple and improved design formula.

8.6 Transient capsize tests

A series of sweeps through frequency was made for fixed paddle throws with the model placed initially at the same distance from the wavemaker for each test. As for the resonance response test, the natural frequency was set to be $\omega_n = 6.7s^{-1}$. Before switching on the wavemaker, any oscillations were allowed to die down. Note that as frequency was increased, the wave height (and slope) also increased. For each throw and frequency a capsize test was made and the roll and wave data recorded.

Due to the difficulty in assigning a steady state wave amplitude with the modulation present, we have considered a maximum A. Give the form of the wave front

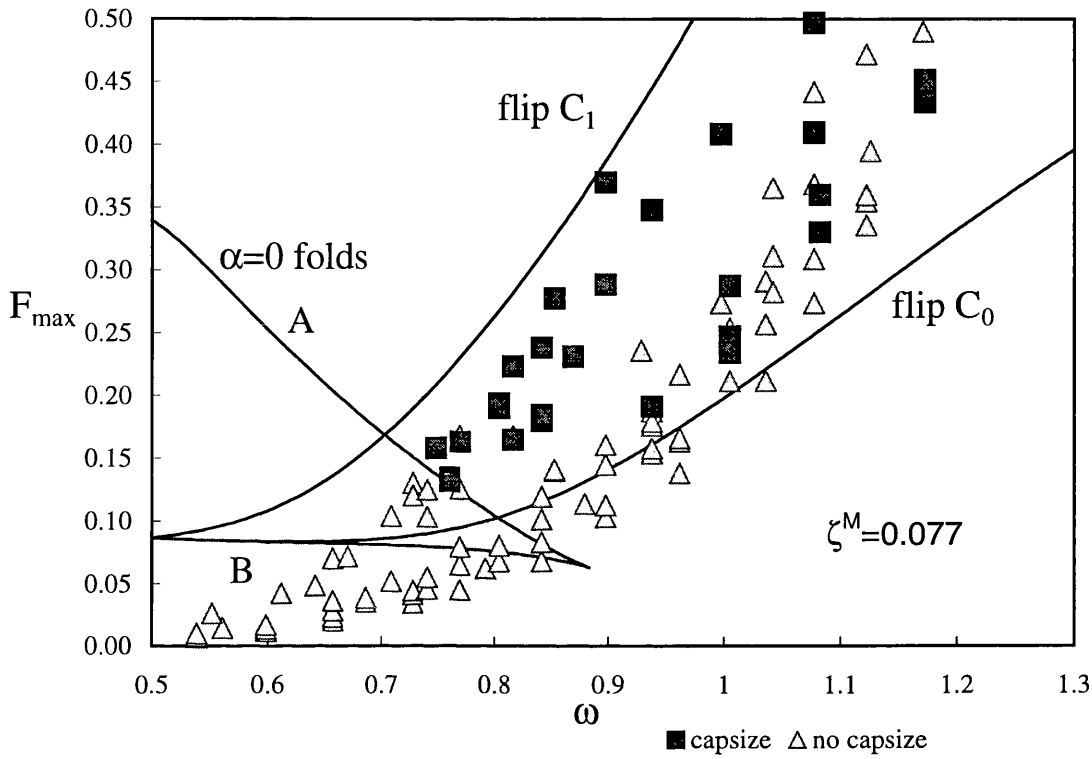

Figure 8.19: Capsize tests compared to steady state bifurcations. Superimposed are the fold and flip bifurcations for the quadratic and cubic escape equations. Melnikov equivalent damping is used. The flip for the $\alpha = 0$ system is marked C_0. Also shown is the flip bifurcation for the symmetric escape equation, C_1. Some areas of the parameter space could not be tested due to experimental limitations (primarily the difficulty of achieving long wavelength, high slope waves).

this is generally the amplitude of the initial peak waves. This is a sensible approach since capsize typically occurred when the model encountered these waves.

In figure 8.18 the data is plotted with the simulated transient capsize line for the nonlinear and Melnikov equivalently damped systems. Encouragingly, the predicted capsizing wave slope is close to that found in the tests. Also shown on this plot are the simple and improved design formula capsize lines, the derivation of which is detailed in chapter 6. We can see how the incorporation of the effects of nonlinear damping leads to a better prediction for the improved design formula.

The capsize results are shown again in figure 8.19, along with the steady-state

bifurcations that we expect to define the capsize domain. In chapter 4 we observed that the fold bifurcations are insensitive to α and so we have plotted only those for the $\alpha = 0$ system here. We expect steady state capsize to be bounded by the fold A and flip C. Note also that the bifurcations are for the $\zeta^M = 0.077$ case. Remember that we do not expect these steady state bifurcations to give a particularly good fit to the data since the capsize tests were essentially transient. In fact the fit is reasonable and significantly, it is the heavily biased, $\alpha = 0$ equation that gives the better prediction. Although superficially this may seem surprising, given the poor fit for the restoring seen in figure 8.12, it is in fact an experimental indication of the symmetry breaking discussed in chapter 4. As discussed in the previous section, the symmetry breaking here is due to the shape of the wave rather than any inherent bias in the model.

8.6.1 Initial conditions

Another feature of capsize observed was sensitivity to initial conditions. It was found that near the capsize boundary, variation of the initial paddle position had a major effect on capsize. In effect, the difference in the wave build up (determined by the paddle start position) was enough to cause the model to end up in a different basin of attraction (safe or capsizing). This sensitivity to the wave build up was consistently repeated and the same dependence seen for a particular slope and frequency. This behaviour can be seen in figures 8.19 and 8.18, particularly close to the flip C, where capsizing and non-capsizing tests exist for the same wave forcing[3]. In figure 8.20, the time series of a test repeated with a different paddle start position is plotted[4] The important difference is in the wave build up; in this case an initial trough causes capsize but if the first wave is a crest then steady-state

[3]There is some variation in Ak, even though the wavemaker control settings were the same.

[4]Note that, because the wave probe was in front of the model (with respect to the wave) the roll is delayed with respect to the wave. This is enhanced by the drift of the model.

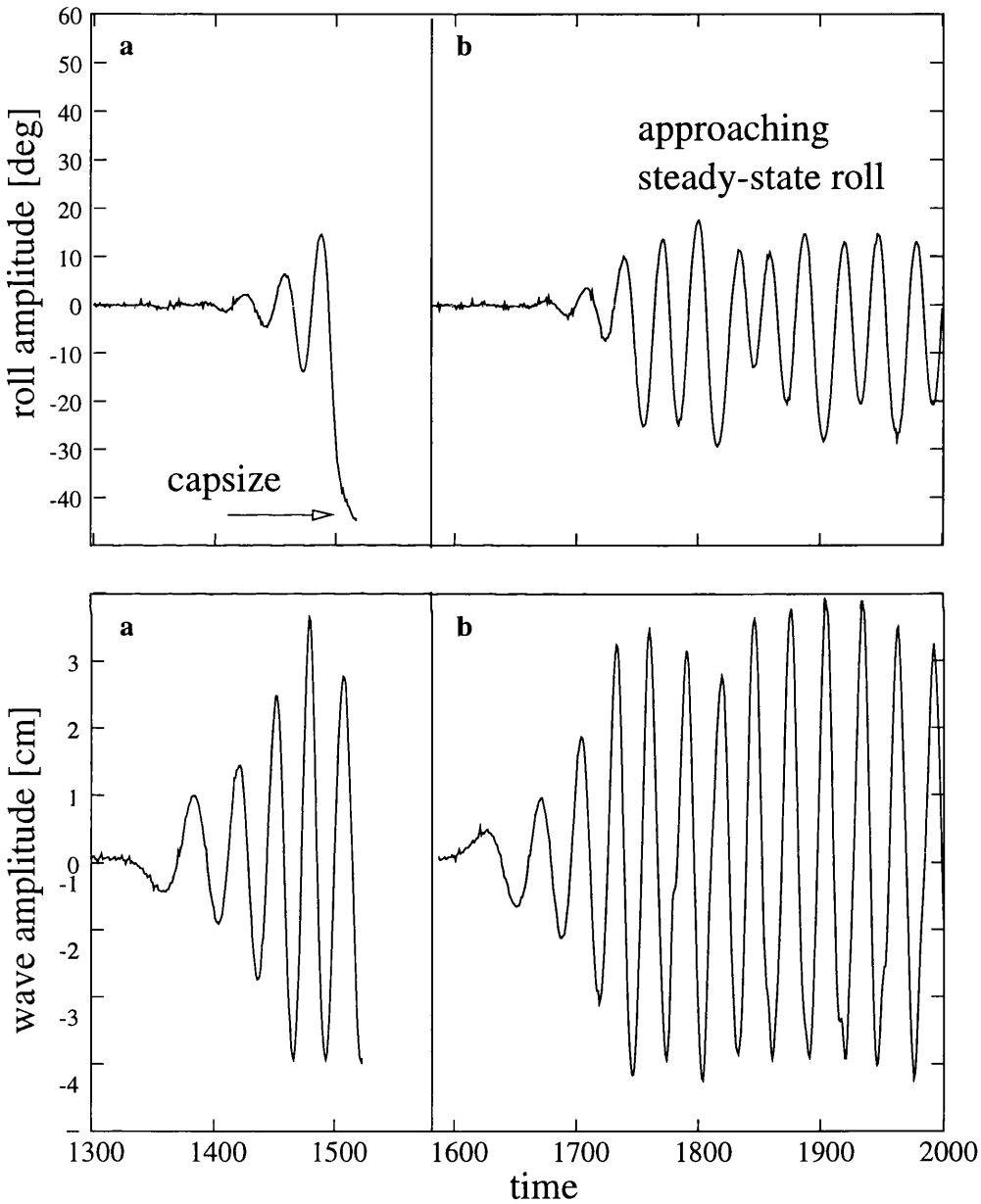

Figure 8.20: The significance of initial conditions: the first test, (a), leads to capsize whilst the second, (b), does not. The only difference is in the initial condition; the wave forcing is the same except (a) begins with a trough and (b) with a crest.

roll is the result.

As a further illustration of the bias present, the model always capsized towards the wave. In a short test in which we added a small bias on the side away from the wave it was found that a static heel of only a few degrees was enough to cause capsize to occur in that direction. This suggests that the wave induced biasing is equivalent (from a capsize perspective) to a static bias of a few degrees. It also supports the theoretical work of chapter 4 that symmetry breaking (even by a small bias) either inherent in the model, or in the wave forcing, has a profound effect on capsize.

8.7 Using the improved design formula

We have shown how the improved design formula can be used to estimate the capsize boundary (see figure 8.19). However, we can also use this approach to determine how one might alter the experimental model to reduce the chances of it capsizing. By substituting back in for the dimensional quantities we can see how the IDF alters as we vary certain parameters.

The IDF for cubic restoring is,

$$Ak^M_{crit} = 2\left[\frac{1}{2(ImgGM)^{1/2}}B_1 + \frac{2\sqrt{2}}{10I}\theta_V B_2 + \frac{6}{35I^{3/2}}\theta_V^2(mgGM)^{1/2}B_3\right]\theta_v \quad (8.2)$$

where $\omega_n = \sqrt{mgGM/I}$ and B_i in equation (3.3). If we now impose the values for I, θ_V and the damping coefficients for our experimental model we can plot the variation of this function against GM, figure 8.21.

In figures 8.21 and 8.22 we have plotted the variation of the IDF with GM for two

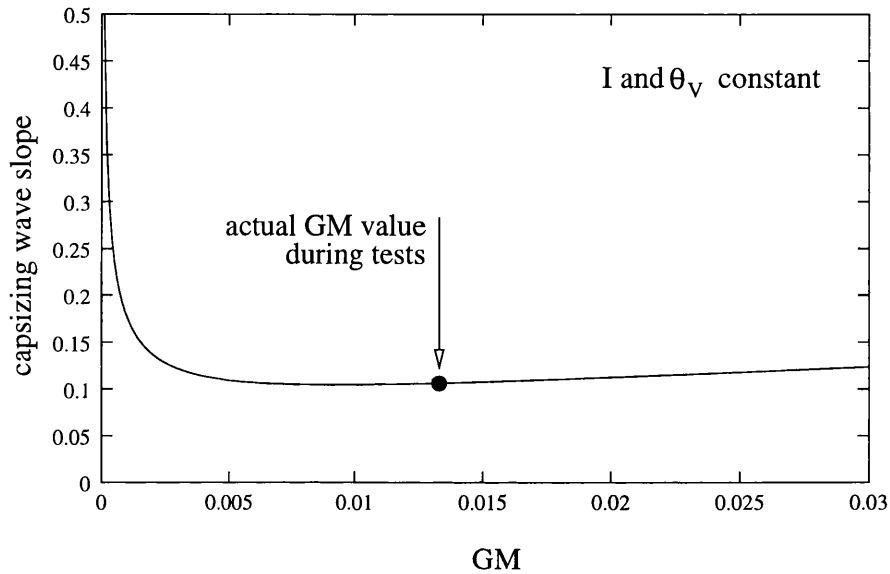

Figure 8.21: The variation of the IDF with GM, holding all other parameters constant. The point for which the tests were conducted is indicated by a filled circle. This graph therefore suggests that an increase in GM would have little effect on the capsizing wave slope. This is misleading since θ_V and I would both typically alter as one changed GM.

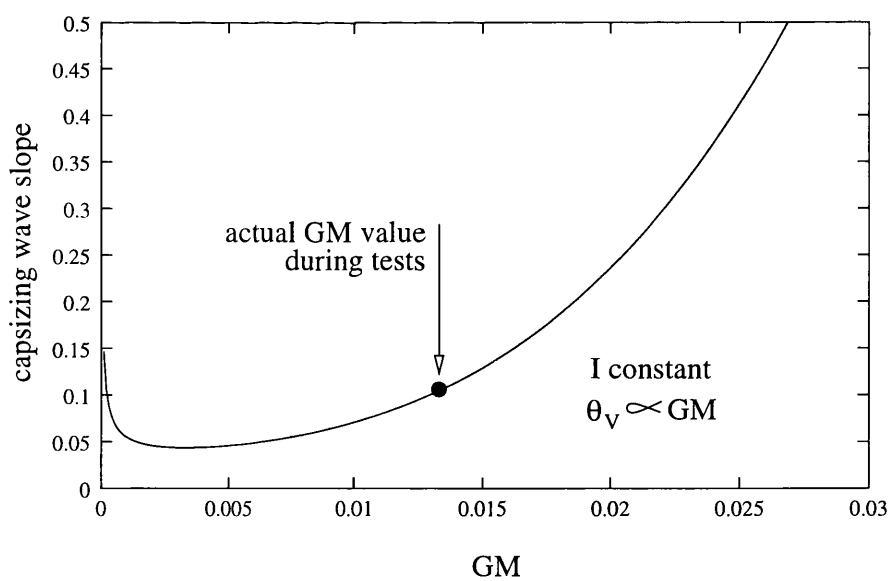

Figure 8.22: The variation of the IDF with GM, with an empirically derived linear relationship between GM and θ_V. The point for which the tests were conducted is again indicated by a circle. The addition of the relationship $GM \propto \theta_V$ has caused the minimum to move to much lower GM values. We thus find the reassuring result that increasing GM will significantly reduce the possibility of capsize.

situations; all other parameters held constant and $GM \propto \theta_V$. In the latter case we have used a local linear fit to measured values for θ_V as a function of GM. This is not valid for very low or high GM. Both plots suggest that a decrease in GM might actually increase the sustainable wave slope (for low enough GM). However, this is a misleading result since we have failed to incorporate the full relationships between the parameters. For instance, if we required $\theta_V \to 0$ as $GM \to 0$ then the capsizing wave slope from the IDF would fall to zero as $GM \to 0$ (see figure 6.10).

In the first figure we find that a small increase in GM has little effect. If we increase GM by 50%, holding all other parameters constant, we only see a 10% increase in sustainable wave slope. Adding an empirical relationship between θ_V and GM gives the more realistic plot of figure 8.22, for which the same increase in GM more than doubles the sustainable wave slope. Although the IDF still rises at low GM this is again misleading since our empirical relationship is only valid around the measured values, i.e. close to the actual value.

This simple analysis shows how one might use the IDF as part of a design process. A similar procedure could be applied to the Melnikov capsize formula.

8.8 Conclusions

In this series of tests we have added to the experimental evidence for the complex nonlinear phenomena which have been theoretically predicted to be linked to capsize. Two stable oscillations were found to exist for frequency ratios of $0.8 < \omega < 0.85$ ($Ak \approx 0.12$). Jumps between such oscillations proved easy to achieve experimentally (a light tap was typically enough) and this obviously has serious implications for stability as well as seakeeping in general.

A further feature observed in the tests was the presence of wave induced bias. This took the form of an effective static heel angle of approximately 2 to 3° and seemed to be fairly independent of roll amplitude. Taken with the sensitivity of capsize resistance to bias in the ship seen in chapter 4, the causes and effects of this bias certainly merit further investigation.

The capsize tests were then compared with a numerically generated 'transient capsize line'. This involved considering the capsize of the ship from one initial condition, given the sudden onset of a wave of a certain amplitude and frequency. Since only one initial condition was considered for each forcing condition, this concept depends on the so-called Dover Cliff phenomenon, a sudden loss of system integrity (Thompson, Rainey & Soliman 1990). In simple terms, above a certain wave slope most initial conditions lead to capsize when the wave is 'switched on'. In fact we compared the tests with two transient capsize boundaries; one for the nonlinear damping model and one using the Melnikov equivalent damping (MED) introduced in chapter 6. These experimental results again support the use of MED for capsize analysis.

We also plotted the capsize results against the steady state bifurcations of the quadratic and cubic escape equations. It was found that the quadratic model gave a much better fit to the data, perhaps surprisingly given its poor fit to the real restoring. However, this would seem to be an indication of the effect of symmetry breaking studied in chapter 4.

Given the simple nature of the roll model used the results were found to fit well with the numerical predictions and suggest the use of such approaches as part of a design testing procedure. These tests represent a first step and there is clearly a need for further work on this front.

We have also presented some data demonstrating the importance of considering

initial conditions when testing for capsize. A number of wave forcing parameters were found to only cause capsize for certain initial conditions. We demonstrated this by varying the wave build up (trough first or crest first). Particularly for a frequency range above resonance ($0.85 < \omega < 1.1$), capsize appeared to be highly sensitive to variation of the wave build up in this way. We should also note that throughout these experiments all tests were carried out at least twice (sometimes many more) for each condition in order to establish the repeatability of the outcome.

Finally we have used our experimental model in an example of how one might use the improved design formula as part of a design procedure. The advantage of analytic expression such as the IDF or the Melnikov capsize formula is that we may substitute in the dimensional quantities and quantify how they affect capsize.These formulae could play an important role in linking design to nonlinear dynamics and this certainly seems an interesting topic for future research.

Chapter 9

CONCLUSIONS

In this thesis we have attempted to improve our ability to use nonlinear dynamics in the modelling of roll and capsize, with a view to developing new approaches to design for the future. In this process we have explored a number of different areas; from the investigation of how simple roll models behave, to the development of formulae for application to real design problems. It is important to note that, at least from a design perspective, much of this work remains at an early stage. We have therefore focussed on obtaining a better understanding of the more promising techniques from nonlinear dynamics. Furthermore, we have accompanied these studies with experimental support for the significance of nonlinear dynamics within this field.

The first part of this thesis is a review of the background to this work, beginning with a systematic formulation of the problem. In deriving a nondimensional equation of motion we have also noted the relationship between capsizing wave slope, the angle of vanishing stability and the linear damping ratio. This relationship comes as a natural consequence of the formulation and leads onto the derivation of the simple design formula of Thompson (1997) which we have also included.

Before progressing with the analysis of the nonlinear dynamics, we then derived physically realistic limits to the validity of our roll model. Since we were generally interested in how the response was affected by changes in the forcing conditions this involved specifying maximum frequency and amplitude limits to our nondimensional forcing. These limits were a consequence of the long wavelength (compared to ship beam width) and regular wave assumptions.

Having framed the problem in terms of a nonlinear oscillator, the significant nonlinear dynamics in such systems, with particular reference to modelling escape from the potential well are then described. Focussing firstly on the steady state dynamics, we discussed the use of bifurcation theory in predicting escape from the potential well. We also presented a bifurcation diagram covering our physically realistic control space, extending previous studies to higher frequencies. As a final part of the steady state analysis we identified a second resonance region defined by previously unidentified bifurcations in this higher frequency region.

We then considered the transient dynamics, describing the concepts of basin of attraction for steady state solutions and how basin erosion plays a role in escape from the well. In particular we discussed the Dover Cliff phenomenon, its importance for the prediction of transient capsize and the realisation of transient capsize diagrams. We also discussed the use of Melnikov's Method for locating the homoclinic and heteroclinic bifurcations that signal the onset of basin erosion. This technique enables the derivation of an analytical expression for the capsize boundary. From a design perspective this has considerable advantages over numerical simulation approaches, not least because parameters defining a ship can be explicitly included.

If the approaches highlighted in the first part of this thesis are to eventually be of use to the naval architect, one of the primary requirements must be to ensure that

they are robust. Previous studies have found that the dynamics of the nonlinear oscillator models used in this work are remarkably robust to changes in the restoring and damping models. We have explored one area for which the behaviour of the system has proved to be highly sensitive - symmetry in the restoring function. A numerical algorithm was used to estimate the steady state capsize boundary as symmetry was broken, over a wide range of forcing frequencies. In this way two main capsize regions were identified around resonance, the higher frequency region of which showed extreme sensitivity to bias. This behaviour was then associated with a flip bifurcation. A careful analysis of this bifurcation as symmetry was broken then showed how its global structure lead to the sensitivity in steady state capsize.

By carefully examining how capsize modelling is affected by symmetry, we therefore demonstrated that this feature must be considered as part of any simulation based testing procedure. This study was accompanied by experimental results (in the final chapter) which indicated that sensitivity to symmetry in restoring may also be important for real testing procedures.

The need to develop robust approaches to capsize prediction was further tackled as part of a general analysis of the significance of saddle connection orbits within the ship capsize problem. Following our studies of biasing from a steady state perspective, we then considered the significance of bias for these orbits, for which Melnikov's Method provides a useful analytical estimate. The existence of two potential hilltops of slightly varying size leads to a complex problem in which the identification of the orbits of interest is not trivial. Using Melnikov's Method, it was possible to show how the balance between energy loss through damping and that gained from the potential difference between the saddle points governs the occurrence of the heteroclinic tangency. We were thus able to show how the occurrence of the tangencies of interest changed as we varied symmetry and damping.

These results were also confirmed using numerical algorithms to accurately locate the saddle connections in control space.

Finally we observed that the homoclinic tangency provides the best estimate for the occurrence of basin erosion, even where the heteroclinic occurs first. By directly locating the important orbits and analysing how they affect basin erosion, we have been able to indicate how one should use Melnikov's Method to predict escape (and hence capsize) for systems of this type.

We then used Melnikov's Method once more to develop a new concept for equivalent damping, deriving expressions for determining a linear damping model that can be used for capsize modelling. This is particularly useful for analytical approaches to capsize prediction and was then applied to produce an improved version of the simple design formula of Thompson (1997). In continuing the development of these new methods, we also highlighted some of the possibilities for their use in design, as well as some of the pitfalls. It was also noted that, because of the simple nature of the models from which they originate, we must be careful in applying these dynamic based formulae. However, they can certainly play a role as part of a wider design strategy.

A frequent (and justified) criticism of the use of simple, single degree of freedom models is the uncertainty in how far the observed behaviour conforms to that of the real system. In the final two chapters of this thesis we have grounded the theoretical work in the real world by conducting a series of roll damping and capsize experiments. These have enabled us not only to test the validity of our capsize models, but also to demonstrate the significance of nonlinearity in the equations of motion. While the simple roll model used in this work can certainly be improved upon (see for instance the modelling of excitation of Contento, Francescutto & Piciullo (1995)) we have found this approach to be surprisingly effective at pre-

dicting capsize under experimental conditions - from a design testing perspective this is indeed encouraging. Furthermore, a key observation from our series of tests was the prevalence of nonlinear behaviour in the roll motion. Regions of coexisting steady states were easily observable and occured over large ranges of forcing conditions.

Another significant experimental observation was the presence of wave induced bias. Despite efforts to condition the model to be symmetric in static response, the roll motion showed persistent and significant bias away from the wave. This behaviour also seemed to affect capsize and the test results supported the sensitivity to bias studied for our theoretical model.

The results of these experiments have considerable implications for testing procedures as well as general vessel operation. These tests represent a first step and, it is hoped, will lead to more thorough investigations along these lines.

Finally we used the experimental model as an example for short study on the use of the improved design formula in design. Formulae such as this and Melnikov's Method may play a useful role in design problems.

Of course the single degree of freedom roll model used throughout cannot hope to match hugely sophisticated, multi degree of freedom simulations when it comes to fitting experimental results to model predictions. However, the large and complex computer simulations of ships that are employed by practising engineers are relatively slow, so that a significantly lower number of simulations are possible. Furthermore, with the known sensitivity to initial conditions, care must be taken in drawing conclusions from such simulations. Perhaps more importantly, given the complexity seen in even simple, single degree of freedom models, it is clear that there is no hope at all of understanding the full dynamics of an industrial model.

A further aspect of considerable significance is the need for a closer link between

the nonlinear dynamics and ship design. While we may at present vary the form of a hull and observe the effect on the improved design formula or the steady state bifurcations, we cannot easily reverse this process. However, there is scope for progress, particularly in the construction of optimisation schemes (Spyrou, Cotton & Thompson 1997; Spyrou 1998). One possibility would be to maximise the capsize boundary predicted by a Melnikov analysis whilst conforming to current design criteria. A further step might be to develop a procedure for generating practical hull shapes given the restoring curve obtained using such optimisation schemes. In this way a link between hull design and the nonlinear dynamics of large angle roll and capsize seems within reach.

To summarise, the aim of this work is not to supplant the current approaches but to complement them with a better understanding of the underlying equations as well as an improved approach to modelling the real system. By utilising this nonlinear dynamical approach it is hoped that improved design procedures and methodologies may be developed in future years. Progress in the design of safe ships clearly depends on the vigorous interplay between both simple and complex mathematical models, accompanied by physical experiments in real waves.

References

Bikdash, B., Balachandran, B. & Nayfeh, A.H. (1994). Melnikov analysis for a ship with a general roll-damping mode . *Nonlinear Dynamics* **6**, 101–124.

Bishop, S.R. & de Souza, J.R. (1993). Transient and steady-state operational limits for ship roll. *Applied Mechanics Reviews* **46**, S47–S52.

Contento, G. & Francescutto, A. (1997, October). Intact stability in beam seas: Mathematical modelling of large amplitude motion. In *Third International Workshop on Theoretical Advances in Ship Stability and Operational Safety of Ships*, Hersonissos, Greece, pp. 59–68.

Contento, G., Francescutto, A. & Piciullo, M. (1995). On the effectiveness of the constant coefficients roll motion equation. *Ocean Engineering* **23**(7), 597–618.

Cotton, B. & Spyrou, K.J. (1997, November). Some recent advances in the analysis of ship roll motion. In *Third Workshop on Stability and Operational Safety of Ships*, National Technical University of Athens, pp. 59–68.

Cusumano, J.P. & Kimble, B.W. (1994). Experimental observation of basins of attraction and homoclinic bifurcation in a magneto-mechanical oscillator. In J.M.T. Thompson and S.R. Bishop (Ed.), *Nonlinearity and Chaos in Engineering Dynamics*, pp. 71–85. Chichester: Wiley.

Dalzell, J.F. (1978). A note on the form of ship roll damping. *Journal of Ship Research* **22**(3), 178–185.

de Souza, J.R. (1995). *Geometrical Methods of Nonlinear Dynamics in Ship Capsize*. Ph. D. thesis, University College London, London, UK.

Falzarano, J.M., Esparza, I. & Mulk, M. Taz Ul (1995). A combined steady-state and transient approach to study large amplitude ship rolling motion and capsizing. *Journal of Ship Research* **39**, 213–224.

Falzarano, J.M., Shaw, S.W. & Troesch, A.W. (1992). Application of global

methods for analyzing dynamical systems to ship rolling motion and capsizing. *Int. J. Bifurcation and Chaos* **2**, 101–116.

Foale, S. & Thompson, J.M.T. (1991). Geometrical concepts and computational techniques of nonlinear dynamics. *Computer Methods in Applied Mechanics and Engineering* **89**, 381–394.

Francescutto, A. (1993). Is it really possible to design safe ships ? *Transactions of Royal Institution of Naval Architects* **135**, 163–173.

Froude, W. (1874). On the resistance in rolling in ships. *Naval Science* **3**, 312.

Guckenheimer, J. & Holmes (1983). *Nonlinear Oscillations, Dynamical Systems and Bifurcations of Vector Fields.* New York: Springer.

Gurd, B.A. (1997, September). A Melnikov analysis of the Helmholtz-Thompson equation. Master's thesis, Centre for Nonlinear Dynamics.

Haddara, M.R. & Bennet, P. (1989). A study of the angle dependence of roll damping moment. *Ocean Engineering* **16**, 411–427.

Hsu (1987). *Cell-to-cell Mapping: A Method of Global Analysis for Nonlinear Systems.* New York: Springer.

Kan, M., Saruta, T. & Taguchi, H. (1991). Capsizing of a ship in quartering waves. *Naval Architecture and Ocean Engineering* **29**, 49–60.

Kan, M. & Taguchi, H. (1991). Chaos and fractals in asymmetric capsize equation. *Journal of the Society of Naval Architects of Japan* **169**.

Kerwin, J.E. (1955). Notes on rolling in longitudinal waves. *International Shipbuilding Progress* **2**(16), 597–614.

Lansbury, A.N. & Thompson, J.M.T. (1990). Incursive fractals: a robust mechanism of basin erosion preceding the optimal escape from a potential well. *Physics Letters* **A 150**, 355–361.

Lansbury, A.N., Thompson, J.M.T. & Stewart, H.B. (1992). Basin erosion in the twin-well Duffing oscillator: two distinct bifurcation scenarios. *International Journal of Bifurcation and Chaos* **2**, 505– 532.

Lloyd, A.R.J.M (1989). *Seakeeping: Ship Behaviour in Rough Weather.* Chichester: Ellis Horwood.

MacMaster, A.G. & Thompson, J.M.T. (1994). Wave tank testing and the capsizability of hulls. *Proceedings of the Royal Society London* **446**, 217–232.

Mei, Chiang C. (1989). *The applied dynamics of ocean surface waves.* Singapore: World Scientific.

Nayfeh, A.H. & Balachandran, B. (1995). *Applied Nonlinear Dynamics.* New York: Wiley.

Nayfeh, A.H. & Khdeir, A.A. (1986). Nonlinear rolling of ships in regular beam seas. *Int. Shipbuilding Prog.* **33**, 40–49.

Nayfeh, A.H. & Sanchez, N.E. (1990). Stability and complicated rolling responses of ships in regular beam waves. *International Shipbuilding Progress* **37**(412), 331–352.

Odabasi, A., Y. (1982, October). A morphology of mathematical stability theory and its application to intact ship stability assessment. In *Second International Conference on Stability of Ships and Ocean Vehicles*, Tokyo.

Rahola, J. (1939). *The Judging of the Stability of Ships and the Determination of the Minimum Amount of Stability.* Ph. D. thesis, University of Finland, Helsinki, Finland.

Sarchin, T.H. & Goldberg, L.L. (1962). Stability and buoyancy criteria for naval surface ships . *Transactions of the Society of Naval Architects and Marine Engineers* **70**, 418 –458.

Scolan, Y.M. (1997). Technical note on ship rolling associated to high degree polynomial restoring moment using the Melnikov Method. *Applied Ocean Research* **19**((3-4)), 225–234.

Soliman, M.S. & Thompson, J.M.T. (1989). Integrity measures quantifying the erosion of smooth and fractal basins of attraction. *Journal of Sound and Vibration* **135**, 453–475.

Soliman, M.S. & Thompson, J.M.T (1991). Basin organization prior to a tangled saddle-node bifurcation. *International Journal of Bifurcation and Chaos* **1**, 107–118.

Soliman, M.S. & Thompson, J.M.T. (1992). Global dynamics underlying sharp basin erosion in nonlinear driven oscillators. *Physical Review* **A 45**, 3425–3431.

Spyrou, K.J. (1996a). Dynamic instability in quartering waves: the behaviour of a ship during broaching. *Journal of Ship Research* **40**(1).

Spyrou, K.J. (1996b). Dynamics instability in quartering seas - Part 2: Analysis of ship roll and capsize for broaching. *Journal of Ship Research* **40**(4), 326–336.

Spyrou, K.J. (1998, September). Ship capsize assesment and nonlinear dynamics. In *Proceedings of the 4th International Workshop on Theoretical Advances in Ship Stability and Practical Impact*, St John's, Newfoundland, Canada.

Spyrou, K.J., Cotton, B. & Thompson, J.M.T. (1997, September). Developing an interface between the nonlinear dynamics of ship rolling in beam seas and ship design. In *Proceedings of the 6th International Conference on Stability of Ships and Ocean Vehicles*, Varna, Bulgaria, pp. 343–351.

Spyrou, K.J. & Thompson, J.M.T. (1998, March). Characterization of ship roll decay from extreme angles. Internal report, Centre for Nonlinear Dynamics, University College London, Gower St., London WC1E 6BT, UK.

Stewart, H.B., Thompson, J.M.T., Ueda, Y. & Lansbury, A.N. (1995). Optimal escape from potential wells: patterns of regular and chaotic bifurcation. *Physica D* **85**, 259–295.

Szemplinska-Stupnicka, W. (1992). Cross-well chaos and escape phenomena in driven oscillators. *Nonlinear Dynamics* **3**, 225–243.

Takezawa, S., Hirayama, T. & Acharrya, S. (1990, September). On large rolling in following directional spectrum waves. In *Fourth International Conference on Stability of Ships and Ocean Vehicles*, Volume 1, University of Naples, Italy, pp. 287–294.

Thompson, J.M.T. (1989). Chaotic phenomena triggering the escape from a potential well. *Proceedings of the Royal Society London* **42**, 195–225.

Thompson, J.M.T. (1992). Global unpredictability in nonlinear dynamics: capture, dispersal and the indeterminate bifurcations. *Physica D* **58**, 260–272.

Thompson, J.M.T (1996). Global dynamics of driven oscillators: Fractal basins and indeterminate bifurcations. In P. Aston (Ed.), *Nonlinear Mathematics and its Applications*, Chapter 1, pp. 1–47. Cambridge: Cambridge University Press.

Thompson, J.M.T. (1997). Designing against capsize in beam seas: Recent advances and new insights. *Applied Mechanics Reviews* **50**, 307–325.

Thompson, J.M.T., Bishop, S.R. & Leung, L.M. (1987). Fractal basins and chaotic bifurcations prior to escape from a potential well . *Physics letters* **A** **121**, 116 –120.

Thompson, J.M.T., Cotton, B., Spyrou, K.J., de Souza, J.R. & Bishop, S.R. (1998). The nonlinear dynamics of ship roll and capsize. Technical report, Centre for Nonlinear Dynamics, University College London.

Thompson, J.M.T. & McRobie, F.A. (1993). Indeterminate bifurcations and the global dynamics of driven oscillators, 1st European Nonlinear Oscillations Conf., Hamburg, Aug 1993. E. Kreuzer and G. Schmidt (eds), Akademie Verlag. *Berlin* **1993**, 107–128.

Thompson, J.M.T., Rainey, R.C.T. & Soliman, M.S. (1990). Ship stability criteria based on chaotic transients from incursive fractals. *Philosophical Transactions of the Royal Society London.* **332**, 149–167.

Thompson, J.M.T., Rainey, R.C.T. & Soliman, M.S. (1992). Mechanics of ship capsize under direct and parametric wave excitation . *Philosophical Transactions of the Royal Society London* **A 338**, 471–490.

Thompson, J.M.T. & Soliman, M.S. (1990). Fractal control boundaries of driven oscillators and their relevance to safe engineering design. *Proceedings of the Royal Society London* **A 428**, 1–13.

Thompson, J.M.T & Stewart, H.B. (1986). *Nonlinear Dynamics and Chaos* . Chichester: Wiley.

Umeda, N., Hamamoto, M., Takaishi, Y., Chiba, Y., Matsuda, A., Sera, W., Susuki, S., Spyrou, K. & Watanabe, K. (1995). Model experiments of ship capsize in astern seas. *Journal of the Society of Naval Architects of Japan* **177**, 207–217.

Vassalos, D. (1985). A critical look into the development of ship stability criteria based on work/energy balance. *Trans. Roy. Inst. Nav. Archits* **127**, 217–234.

Virgin, L.N. (1988). On the harmonic response of an oscillator with unsymmetric restoring force. *Journal of Sound and Vibration* **126**, 157–165.

Virgin, L.N. (1989). Approximate criterion for capsize based on deterministic dynamics. *Dynamics and Stability of Systems* **4**, 55–70.

Wright, J.H.G. & Marshfield, W.B. (1980). Ship roll response and capsize behaviour in beam seas. *Transactions of the Royal Institute of Naval Architects* **122**, 129–148.

Appendix A

Melnikov calculations

A.1 Solution for integrals used in Melnikov's Method

We are looking for homoclinic and heteroclinic tangencies in the following system,

$$\ddot{x} + \beta\dot{x} + x(1-x)(1+\alpha x) = F\sin(\omega t) \tag{A.1}$$

A.1.1 Homoclinic tangencies

We begin with the Hamiltonian system

$$\ddot{x} + x(1-x)(1+\alpha x) = 0 \tag{A.2}$$

Making a coordinate change so that $s = x - 1$ we can rewrite (A.2),

$$\ddot{s} = \alpha s^3 + (2\alpha+1)s^2 + (\alpha+1)s \tag{A.3}$$

and integrating then gives,

$$\frac{\dot{s}^2}{2} = \frac{\alpha s^4}{4} + \frac{(2\alpha+1)s^3}{3} + \frac{(\alpha+1)s^2}{2} \tag{A.4}$$

which we can rearrange,

$$\frac{ds}{dt} = \pm\sqrt{(\alpha/2)s\left[(s+a)^2 - b^2\right]} \tag{A.5}$$

where

$$a = 2(2\alpha+1)/3\alpha \qquad b^2 = 2(1-\alpha)(2+\alpha)/(9\alpha^2)$$

The solution of an integral of this form is known (Gurd 1997) so we finally write,

$$s = \frac{b^2 - a^2}{a + b\cosh(\sqrt{1+\alpha}t)^2} \qquad \frac{ds}{dt} = \frac{b\sqrt{1+\alpha}(a^2-b^2)\sinh(\sqrt{1+\alpha}t)}{(a+b\cosh(\sqrt{1+\alpha}t))^2} \tag{A.6}$$

A.1.2 Applying Melnikov's Method

We can think of Melnikov's method as an energy balance , in effect we simply need to balance the terms from the added damping and forcing to locate the homoclinic tangency, or

$$M(t_0) = \int_{-\infty}^{\infty} \frac{ds}{dt}\left[F\sin(\omega(t+t_0)) - \beta\frac{ds}{dt}\right]dt = E_F - E_D = 0 \tag{A.7}$$

We now need to balance the forcing and damping energy terms (E_F and E_D respectively) which in this case this is completely equivalent to applying the Melnikov method in full.

The forcing term

Substituting in for ds/dt the forcing term becomes,

$$E_F = \frac{F\sqrt{1+\alpha}(a^2-b^2)\cos(\omega t_0)}{b}\int \frac{\sin(\omega t)\sin(\sqrt{1+\alpha}t)}{(a/b+\cosh(\sqrt{1+\alpha}t))^2}dt \tag{A.8}$$

and letting $\tau = \sqrt{1+\alpha}t$ gives,

$$\frac{F(a^2-b^2)\cos(\omega t_0)}{b}\int \frac{\sin(\mu\tau)\sinh(\tau)}{(a/b+\cosh(\tau))^2}dt \tag{A.9}$$

where $\mu = \omega/\sqrt{(}1+\alpha)$.

This can be solved using a contour integration approach. We begin by rewriting the integral as the imaginary part of the following integral,

$$\int_{-\infty}^{\infty} \frac{e^{i\mu\tau}\sinh(\tau)}{(A+\cosh(\tau))^2}dt \qquad \text{where} \quad A = a/b \tag{A.10}$$

If we now consider integrating this integral,

$$\int_{-\infty}^{\infty} \frac{e^{i\mu z}\sinh(z)}{(A+\cosh(z))^2}dt \qquad \text{where} \quad z = x + iy \tag{A.11}$$

along the following contour,

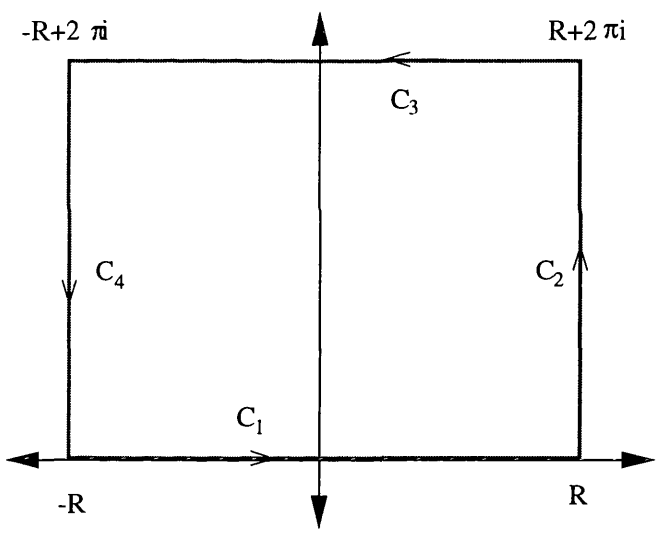

with the limit $R \to \infty$, then I_1 (the integral of (A.11) along C_1) is the integral we are trying to solve. We can now use Cauchy's residue theorem to find I_1.

Since, for large R, the terms in I_2 and I_4 tend to $1/e^R$ they both go to zero as $R \to \infty$ so we only need consider C_3. Substituting $y = 2\pi i$ into (A.11) gives,

$$-e^{-2\mu\pi}\int_{-R}^{-R} \frac{e^{\mu x i}\sinh(x)}{(A+\cosh(x))^2}dx = -e^{-2\mu\pi}I_1 \tag{A.12}$$

By Cauchy we know that the sum of the integrals must equal $2\pi i$ times the sum of the residues enclosed by the contour so we can now write,

$$(1 - e^{-2\mu\pi}) \int_{-R}^{-R} \frac{e^{\mu x i} \sinh(x)}{(A + \cosh(x))^2} dx = 2\pi i \Sigma \text{residues} \tag{A.13}$$

and hence

$$I_1 = \frac{2\pi i \Sigma \text{residues}}{(1 - e^{-2\mu\pi})} \tag{A.14}$$

Calculating the residues

To calculate the residues we must first identify the poles (where the denominator of the integrand is zero) within the contour;

$$\cosh(z) = -A \tag{A.15}$$

$$\Rightarrow z_\pm = \pm \log\left[-A + \sqrt{A^2 - 1}\right] \tag{A.16}$$

$$\Rightarrow z_\pm = \pm \log\left[+A - \sqrt{A^2 - 1}\right] \tag{A.17}$$

Changing variable once more so that $w = z - z_\pm$ we again rewrite the integrand as,

$$\frac{e^{i\mu(w+z_\pm)} \sinh(w + z_\pm)}{(A + \cosh(w + z_\pm))^2} \tag{A.18}$$

Expanding the hyperbolics, substituting back in for $z_\pm$ and rearranging leads finally to,

$$\frac{e^{\mu z_\pm i}}{w^2(A^2 - 1)} \left[\frac{e^{\mu w i}(-A \sinh(w) \pm \sqrt{A^2 - 1} \cosh(w))}{(\pm A(1 - \cosh(w))/(w\sqrt{A^2 - 1}) + \sinh(w)/w)^2} \right] \tag{A.19}$$

The residue of the expression is the coefficient of $1/w$ in the Laurant series expansion,

$$\begin{aligned}
&\frac{e^{\mu z \pm i}}{w^2(A^2-1)}\left[1+\mu w i+\cdots\right] \\
&\times\left[-A(w+w^3/3!+\cdots)\pm\sqrt{A^2-1}(1+w^2/2+\cdots)\right] \qquad \text{(A.20)}\\
&\times\left[1\pm wA(2/\sqrt{A^2-1})+\cdots\right]^{-2} \\
=\ &\frac{e^{\mu z \pm i}}{w^2(A^2-1)}\left[1+\mu w i+\cdots\right] \\
&\times\left[-A(w+w^3/3!+\cdots)\pm\sqrt{A^2-1}(1+w^2/2+\cdots)\right] \qquad \text{(A.21)}\\
&\times\left[1\pm wA/\sqrt{A^2-1}+\cdots\right]
\end{aligned}$$

which gives us a residue of,

$$\pm\frac{e^{\mu z \pm i}}{(A^2-1)}[A-A\pm\mu\sqrt{A^2-1}i]=\pm\frac{\mu e^{i\mu z\pm}}{\sqrt{A^2-1}}i \qquad \text{(A.22)}$$

We now sum the two residues,

$$\Sigma\text{residues}=\frac{\mu}{\sqrt{A^2-1}}i\left[e^{\mu z+i}-e^{\mu z-i}\right] \qquad \text{(A.23)}$$

and substituting from (A.17) gives

$$\begin{aligned}
&= -\frac{2\mu e^{-\mu\pi}}{\sqrt{A^2-1}}\sin(\mu\log(A-\sqrt{A^2-1})) && \text{(A.24)}\\
&= \frac{2\mu e^{-\mu\pi}}{\sqrt{A^2-1}}\sin(\mu\cosh^{-1}(A)) && \text{(A.25)}
\end{aligned}$$

So finally, using (A.14), we find that,

$$\begin{aligned}
I_1 &= 2\pi i\frac{2\mu e^{-\mu\pi}\sin(\mu\cosh^{-1}(A))}{\sqrt{A^2-1}(1-e^{-2\mu\pi})} && \text{(A.26)}\\
&= \pi i\frac{2\mu\sin(\mu\cosh^{-1}(A))}{\sqrt{A^2-1}\sin(\mu\pi)} && \text{(A.27)}
\end{aligned}$$

and this gives us the solution for the forcing term of the Melnikov expression,

$$E_F = \frac{F\sqrt{1+\alpha}(a^2-b^2)\cos(\omega t_0)}{b} 2\pi \frac{\mu \sin(\cosh^{-1}(a/b))}{\sqrt{(a/b)^2-1}\sin(\mu\pi)} \tag{A.28}$$

where as before $\mu = \omega/\sqrt{(}1+\alpha)$ and $A = a/b$.

The damping term

We firstly rewrite the damping term as the area under the homoclinic orbit in phase space, using equation (A.5),

$$E_D = \int_{-\infty}^{\infty} \beta \frac{ds}{dt} dt \tag{A.29}$$

$$\Rightarrow E_D = \beta\sqrt{\frac{\alpha}{2}} \int \pm s \left[(s+a)^2 - b^2\right]^{1/2} ds \tag{A.30}$$

where the second integral is taken around the homoclinic orbit. Since the orbit is symmetric about $ds/dt = 0$ we can remove the ambiguity of the $\pm$ by rewriting this as the sum of the two parts,

$$E_D = \beta\sqrt{2\alpha} \int_0^{b-a} s \left[(s+a)^2 - b^2\right]^{1/2} ds \tag{A.31}$$

where the limits are obtained from (A.5).

The solution to this integral is,

$$\beta\sqrt{2\alpha}\left[\left(\frac{-a^2-2b^2}{6} + \frac{as}{6} + \frac{s^2}{3}\right)\sqrt{-b^2+((a+s))^2} + \right. \tag{A.32}$$

$$\left. \frac{ab^2}{2}\log\left[a+s+\sqrt{(-b^2)+((a+s))^2}\right]\right]_0^{b-a} \tag{A.33}$$

$$= \beta\sqrt{2\alpha}\left[\frac{ab^2}{2}\log(b) - \frac{(-a^2-2b^2)\sqrt{a^2-b^2}}{6} - \right. \tag{A.34}$$

$$\left. \frac{ab^2}{2}\log\left[a+\sqrt{a^2-b^2}\right]\right] \tag{A.35}$$

$$= \beta\sqrt{2\alpha}\left[\frac{(a^2+2b^2)\sqrt{a^2-b^2}}{6} - \frac{ab^2}{2}\log\left[\frac{a}{b}+\sqrt{(a/b)^2-1}\right]\right] \tag{A.36}$$

$$\Rightarrow E_D = \frac{\beta\sqrt{2\alpha}}{6}\left[(a^2+2b^2)\sqrt{a^2-b^2} - 3ab^2\cosh^{-1}\left(\frac{a}{b}\right)\right] \tag{A.37}$$

where in the final step we have used the identity $\cosh^{-1}(x/a) = \log(x/a + \sqrt{((x/a)^2 - 1})$.

Hence we can finally write down the Melnikov expression for the homoclinic tangency,

$$\begin{aligned} M(t_0) &= E_F - E_D \\ &= \frac{F\sqrt{1+\alpha}(a^2-b^2)\cos(\omega t_0)}{b} 2\pi i \frac{2\mu \sin(\cosh^{-1}(a/b))}{\sqrt{(a/b)^2-1}\sin(\mu\pi)} \\ &\quad -\frac{\beta\sqrt{2\alpha}}{6}\left[(a^2+2b^2)\sqrt{a^2-b^2} - 3ab^2\cosh^{-1}\left(\frac{a}{b}\right)\right] \end{aligned} \tag{A.38}$$

A.1.3 Heteroclinic tangency in the perturbed system

The derivation of the Melnikov expression for the perturbed heteroclinic connection can be considered as a simple extension to the symmetric heteroclinuc connection problem. We just need to add a term to account for the change in potential from one saddle to the other. Thus the Melnikov expression can be written,

$$M(t_0) = E_F - E_D + \Delta V \tag{A.39}$$

where ΔV is the potential difference between the two saddles. Since E_F and E_D are calculated for the unperturbed heteroclinic orbit, we need only find the contribution from ΔV and add that to the known expression for the symmetric system (Nayfeh & Balachandran 1995),

$$\Rightarrow M(t_0) = \frac{-2\sqrt{2}\beta + 3\sqrt{2}F\omega\pi\sin(\omega t_0)}{3\sinh(\omega\pi/2)} + \Delta V \tag{A.40}$$

To find ΔV we first rewrite our perturbed system,

$$\ddot{x} + \beta\dot{x} + x(1-x)(1+\alpha x) = F\sin(\omega t) \tag{A.41}$$

$$= \ddot{x} + \beta\dot{x} + x - x^3 + (1-\alpha)(x^2 - x^3) = F\sin(\omega t) \tag{A.42}$$

and hence,

$$\Delta V = \int_{-1}^{1} x^2 - x^3 dx \tag{A.43}$$

$$\Rightarrow \Delta V = \frac{2(1-\alpha)}{3} \tag{A.44}$$

So the Melnikov expression for the perturbed heteroclinic connection is,

$$M(t_0) = E_F - E_D + \Delta V = \frac{\sqrt{2}\left(\alpha - 1 - \sqrt{2}\beta\right)\sinh(\frac{\omega\pi}{\sqrt{2}})}{3\omega\pi\sin(\omega t_0)} \tag{A.45}$$

Note that one can also frame this problem using the standard Melnikov approach (see for example (Guckenheimer & Holmes 1983)) but the analysis is identical.

A.2 Solutions for Melnikov equivalent damping

Quadratic Restoring, $\mathbf{HT_0}$

We start with the Hamiltonian system,

$$\ddot{x} + x - x^2 = 0 \tag{A.46}$$

or alternatively

$$\begin{aligned} \dot{x} &= y \\ \dot{y} &= x^2 - x \end{aligned}$$

$$\Longrightarrow \frac{dy}{dx} = \frac{x^3 - x}{x} \tag{A.47}$$

Integrating (A.47) and using suitable initial conditions then gives us the equation describing the homoclinic orbit,

$$y = \frac{ds}{dt} = s\sqrt{1 + 2s/3} \qquad \text{where } s = x - 1 \tag{A.48}$$

Integrating again we arrive finally at the expression for the velocity $\dot{x}$ as a function of time,

$$s(t) = \frac{-3}{1+\cosh t} \tag{A.49}$$

$$\Longrightarrow \dot{x}(t) = \frac{3\sinh t}{(1+\cosh t)^2} \tag{A.50}$$

We now wish to consider the perturbed system in which we have introduced forcing and damping terms. For our purposes we require the integrals representing the energy lost through damping over one roll cycle, which we approximate by the Hamiltonian oscillation. For cubic damping we require I_1, I_2 and I_3, where

$$I_1 = \int_0^\infty \frac{9\sinh^2 t}{(1+\cosh t)^4} dt = \frac{3}{5} \tag{A.51}$$

$$I_2 = \int_0^\infty \frac{27\sinh^3 t}{(1+\cosh t)^6} dt = \frac{9}{32} \tag{A.52}$$

$$I_3 = \int_0^\infty \frac{81\sinh^2 t}{(1+\cosh t)^8} dt = \frac{54}{385} \tag{A.53}$$

Substituting these values into equation (6.17) we arrive finally at,

$$\zeta^M = \left[\frac{3}{5}b_1 + \frac{9}{32}b_2 + \frac{54}{385}b_3\right]\frac{5}{6}$$

$$\Longrightarrow \zeta^M = \frac{1}{2}b_1 + \frac{15}{64}b_2 + \frac{9}{77}b_3 \tag{A.54}$$

If we then compare this result with (6.6) for the quadratic terms we find

$$\frac{15}{64} = \frac{4a}{3\pi} \tag{A.55}$$

$$\Longrightarrow a \approx 0.552 \tag{A.56}$$

or comparing the cubic terms.

$$\frac{9}{77} = \frac{3a^2}{8} \tag{A.57}$$

$$\Longrightarrow a \approx 0.558 \tag{A.58}$$

Cubic Restoring, $\mathbf{HT}_1$

We start with the Hamiltonian system,

$$\ddot{x} + x - x^3 = 0 \tag{A.59}$$

or alternatively

$$\begin{aligned} \dot{x} &= y \\ \dot{y} &= x^3 - x \end{aligned}$$

$$\Longrightarrow \frac{dy}{dx} = \frac{x^3 - x}{x} \tag{A.60}$$

Integrating (A.60) and using suitable initial conditions then gives us the equation describing the heteroclinic orbit,

$$y = \frac{dx}{dt} = \pm\frac{x^2 - 1}{\sqrt{2}} \tag{A.61}$$

Integrating again we arrive finally at the expression for the velocity $\dot{x}$ as a function of time,

$$x(t) = \pm\tanh(t/\sqrt{2}) \tag{A.62}$$

$$\Longrightarrow \dot{x}(t) = \pm\frac{1}{\sqrt{2}\cosh^2(t/\sqrt{2})} \tag{A.63}$$

As for quadratic restoring we require I_1, I_2 and I_3, where

$$I_1 = \int_{-\infty}^{\infty} \left[\sqrt{2}\cosh^2(t/\sqrt{2})\right]^{-2} dt = \frac{4}{3\sqrt{2}} \tag{A.64}$$

$$I_2 = \int_{-\infty}^{\infty} \left[\sqrt{2}\cosh^2(t/\sqrt{2})\right]^{-3} dt = \frac{8}{15} \tag{A.65}$$

$$I_3 = \int_{-\infty}^{\infty} \left[\sqrt{2}\cosh^2(t/\sqrt{2})\right]^{-4} dt = \frac{16}{35\sqrt{2}} \tag{A.66}$$

Substituting these values into equation (6.17) we arrive finally at,

$$\zeta = \left[\frac{4}{3\sqrt{2}}b_1 + \frac{8}{15}b_2 + \frac{16}{35\sqrt{2}}b_3\right]\frac{3\sqrt{2}}{8}$$

$$\Longrightarrow \zeta = \frac{1}{2}b_1 + \frac{2\sqrt{2}}{10}b_2 + \frac{6}{35}b_3 \tag{A.67}$$

If we then compare this result with (6.6) for the quadratic terms we find ,

$$\frac{2\sqrt{2}}{10} = \frac{4a}{3\pi} \tag{A.68}$$

$$\Longrightarrow a \approx 0.67 \tag{A.69}$$

or comparing the cubic terms.

$$\frac{2\sqrt{2}}{10} = \frac{3a^2}{8} \tag{A.70}$$

$$\Longrightarrow a \approx 0.67 \tag{A.71}$$

p

Appendix B

Roll damping experiments

B.1 Model conditioning

Table B.1: Roll model details: Mass, GM and roll period

Aerial mass position	Mass		GM		Roll Period	
	Model kg	f/s T	Model m	f/s m	f/s s	Model s
Average Condition						
high	249.54	4000	0.033	0.816	3.02	15.1
mid	249.54	4000	0.038	0.952	2.46	12.3
low	249.54	4000	0.046	1.142	2.304	11.52
Light Condition						
high	218.34	3500	0.036	0.888	2.927	14.64
mid	218.34	3500	0.044	1.106	2.417	12.09
low	218.34	3500	0.05	1.243	2.26	11.3

Table B.2: Roll model details: Moments of inertia

Aerial mass position	Moment of Inertia NoDamp Model kg.m2	NoDamp f/s T.m2	Damp Model kg.m2	Damp f/s T.m2
Average Condition				
mid	18.45	1.85E+05	18.72	1.88E+05
high	14.29	1.43E+05	14.52	1.46E+05
low	15.04	1.51E+05	15.3	1.53E+05
Light Condition				
mid	16.51	1.65E+05	16.47	1.65E+05
high	14.02	1.41E+05	14.27	1.43E+05
low	13.78	1.38E+05	13.97	1.40E+05

Table B.3: Roll model details: Radii of gyration

Aerial mass position	Radius of Gyration NoDamp Model m	NoDamp FullScal m	Damped Model m	Damped FullScal m
Average Condition				
mid	0.239	5.98	0.241	6.03
high	0.272	6.8	0.274	6.85
low	0.245	6.14	0.248	6.19
Light Condition				
mid	0.253	6.34	0.256	6.39
high	0.275	6.87	0.275	6.87
low	0.251	6.28	0.253	6.32

Table B.4: Roll model details: GZ curves

Heel Angle [deg]	GZ [m] Average Condition Hi GM	Mid GM	Lo GM	Light Condition Hi GM	Mid GM	Lo GM	No Superstructure Mid GM
0	0	0	0	0	0	0	0
5	0.098	0.085	0.07	0.105	0.093	0.074	0.084
10	0.194	0.167	0.139	0.205	0.182	0.144	0.167
15	0.287	0.247	0.205	0.296	0.263	0.206	0.247
20	0.376	0.323	0.267	0.378	0.334	0.259	0.322
25	0.46	0.395	0.324	0.448	0.393	0.3	0.393
30	0.537	0.46	0.377	0.505	0.44	0.33	0.459
35	0.61	0.521	0.427	0.553	0.478	0.352	0.52
40	0.683	0.582	0.477	0.597	0.513	0.372	0.58
45	0.763	0.65	0.537	0.65	0.559	0.403	0.641
50	0.865	0.742	0.62	0.727	0.627	0.459	0.664
55	1.012	0.878	0.75	0.848	0.742	0.562	0.645
60	1.218	1.077	0.941	1.04	0.927	0.737	0.593
65	1.425	1.281	1.135	1.276	1.158	0.959	0.516
70	1.606	1.46	1.305	1.484	1.362	1.155	0.423
75	1.748	1.596	1.439	1.652	1.527	1.314	0.316
80	1.83	1.669	1.515	1.759	1.631	1.415	0.194
85	1.846	1.677	1.527	1.789	1.66	1.441	0.055
90	1.814	1.641	1.494	1.774	1.644	1.424	-0.102

B.2 Test results

p or s	release from port or starboard heel
mdl	model
f/s	full scale
M of I	Moment of Inertia

Table B.5: Roll test results

No.	p or s	Mass mdl (kg)	Mass f/s T	GM mdl m	GM f/s m	M of I mdl kgm^2	M of I f/s Tm^2	Comments
Average Displacement with Bilge Keels								
1	p	249.54	4000	0.038	0.952	14.52	14520	small roll
2	p	249.54	4000	0.038	0.952	14.52	14520	start with roll to top of GRP
3	p	249.54	4000	0.038	0.952	14.52	14520	start with roll to foam deck MODEL MAY HAVE TAKEN ON WATER
4	p	249.54	4000	0.038	0.952	14.52	14520	ditto MODEL FOUND TO HAVE TAKEN ON WATER
5	s	249.54	4000	0.038	0.952	14.52	145200	start with roll to fwd BK just in water
6	s	249.54	4000	0.038	0.952	14.52	145200	ditto
7	p	249.54	4000	0.038	0.952	14.52	145200	start with roll to top of GRP. BK hits surface on return roll
8	p	249.54	4000	0.038	0.952	14.52	145200	ditto
9	s	249.54	4000	0.038	0.952	14.52	145200	start with roll so BK just out of water
10	s	249.54	4000	0.038	0.952	14.52	145200	ditto

Table B.6: Roll test results, cont.

No.	p or s	Mass mdl (kg)	Mass f/s T	GM mdl m	GM f/s m	M of I mdl kgm^2	M of I f/s Tm^2	Comments
Average Displacement with Bilge Keels								
11	p	249.54	4000	0.046	1.142	15.3	153000	start with roll to top of GRP
12	p	249.54	4000	0.046	1.142	15.3	153000	ditto
13	p	249.54	4000	0.033	0.816	18.72	187200	BAD RUN
14	p	249.54	4000	0.033	0.816	18.72	187200	start with roll to top of GRP. BK emerges on return roll
15	p	249.54	4000	0.033	0.816	18.72	187200	ditto
16	p	249.54	4000	0.033	0.816	18.72	187200	start with roll to foam deck. BK emerges on return roll
17	p	249.54	4000	0.033	0.816	18.72	187200	ditto
18	p	249.54	4000	0.046	1.142	15.3	153000	start with roll to foam deck. BK emerges on return roll
19	p	249.54	4000	0.046	1.142	15.3	153000	ditto

Table B.7: Roll test results, cont.

No.	p or s	Mass mdl (kg)	Mass f/s T	GM mdl m	GM f/s m	M of I mdl kgm^2	M of I f/s Tm^2	Comments
Low Displacement with Bilge Keels								
20	p	218.34	3500	0.044	1.106	14.27	142700	
21	p	218.34	3500	0.044	1.106	14.27	142700	
22	p	218.34	3500	0.044	1.106	14.27	142700	
23	p	218.34	3500	0.044	1.106	14.27	142700	
24	p	218.34	3500	0.044	1.106	14.27	142700	PROBLEMS WITH 50Hz NOISE RUNS 023-031
25	p	218.34	3500	0.044	1.106	14.27	142700	
26	p	218.34	3500	0.044	1.106	14.27	142700	PROBLEMS WITH 50Hz NOISE RUNS 023-031
27	p	218.34	3500	0.036	0.888	16.47	164700	
28	p	218.34	3500	0.036	0.888	16.47	164700	
29	p	218.34	3500	0.05	1.243	13.97	139700	start roll from GRP level
30	p	218.34	3500	0.05	1.243	13.97	139700	poor zero level for -6/6deg channel
31	p	218.34	3500	0.05	1.243	13.97	139700	start roll from GRP level (repeat 029)
32	p	218.34	3500	0.044	1.106	14.27	142700	BAD RUN
33	p	218.34	3500	0.044	1.106	14.27	142700	start roll from GRP level
34	p	218.34	3500	0.044	1.106	14.27	142700	ditto
35	p	218.34	3500	0.044	1.106	14.27	142700	start roll from near bottom of funnel
36	p	218.34	3500	0.044	1.106	14.27	142700	ditto
37	p	218.34	3500	0.036	0.888	16.47	164700	start roll from GRP level
38	p	218.34	3500	0.036	0.888	16.47	164700	ditto
39	p	218.34	3500	0.036	0.888	16.47	164700	start roll from near bottom of funnel
40	p	218.34	3500	0.036	0.888	16.47	164700	ditto

Table B.8: Roll test results, cont.

No.	p or s	Mass mdl (kg)	Mass f/s T	GM mdl m	GM f/s m	M of I mdl kgm^2	M of I f/s Tm^2	Comments
Average Displacement with no Bilge Keels								
41	p	249.54	4000	0.038	0.952	14.52	145200	start roll GRP level
42	p	249.54	4000	0.038	0.952	14.52	145200	ditto
43	s	249.54	4000	0.038	0.952	14.52	145200	ditto
44	s	249.54	4000	0.038	0.952	14.52	145200	ditto
45	p	249.54	4000	0.038	0.952	14.52	145200	start with roll to foam deck
46	p	249.54	4000	0.038	0.952	14.52	145200	ditto
47	p	249.54	4000	0.038	0.952	14.52	145200	start roll from near bottom of funnel
48	p	249.54	4000	0.038	0.952	14.52	145200	ditto
49	p	249.54	4000	0.033	0.816	18.72	187200	start roll from GRP level
50	p	249.54	4000	0.033	0.816	18.72	187200	ditto
51	p	249.54	4000	0.033	0.816	18.72	187200	start with roll to foam deck
52	p	249.54	4000	0.033	0.816	18.72	187200	ditto
53	p	249.54	4000	0.033	0.816	18.72	187200	start roll from near bottom of funnel
54	p	249.54	4000	0.033	0.816	18.72	187200	ditto
55	p	249.54	4000	0.046	1.142	15.3	153000	start roll from GRP level
56	p	249.54	4000	0.046	1.142	15.3	153000	ditto

Table B.9: Roll test results, cont.

No.	p or s	Mass mdl (kg)	Mass f/s T	GM mdl m	GM f/s m	M of I mdl kgm^2	M of I f/s Tm^2	Comments
Average Displacement with no Bilge Keels								
57	-	249.54	4000	0.046	1.142	15.3	15300	FORCED ROLL + RELEASE TEST. Loose centre ballast
58	-	249.54	4000	0.046	1.142	15.3	15300	FORCED ROLL + RELEASE TEST. Loose centre ballast
59	p	249.54	4000	0.046	1.142	15.3	15300	start with roll to foam deck. Loose centre ballast
60	-	249.54	4000	0.046	1.142	15.3	15300	WAVES - 0.42Hz. Amplitude 0.04m
61	-	249.54	4000	0.033	0.816	18.72	18720	WAVES - 0.42Hz. Amplitude 0.08m
62	-	249.54	4000	0.033	0.816	18.72	18720	WAVES - 0.42Hz. Amplitude 0.09m 0.01
63	-	249.54	4000	0.033	0.816	18.72	18720	WAVES - 0.42Hz. Amplitude 0.16m 0.01
64	-	249.54	4000	0.033	0.816	18.72	18720	WAVES - 0.33Hz. Amplitude 0.13m 0.01
65	-	249.54	4000	0.033	0.816	18.72	18720	WAVES - 0.33Hz. Amplitude 0.15m 0.01

Appendix C

UCL capsize experiments: Test results

Table C.1: Capsize test details

Data File	wave maker frequency setting	wave frequency [rads/s]	steady state wave amplitude [cm]	max wave amplitude [cm]	Comments
caps3.dat	70	5.386	5.559	6.960	capsize
caps4.dat	75	5.712	5.656	8.031	capsize
caps5.dat	80	6.283	5.581	6.875	capsize
caps6.dat	85	6.732	5.975	7.601	capsize
caps6.dat	85	6.732	6.221	8.089	capsize
caps6.dat	85	6.732	6.247	8.175	capsize
caps7.dat	90	6.981	5.661	7.353	capsize
caps7.dat	90	7.250	6.209	8.730	capsize
caps8.dat	100	8.195	4.932	7.590	capsize
caps8.dat	100	7.854	4.735	7.590	capsize
caps9.dat	60	4.597	2.154	2.434	no capsize
caps10.dat	65	4.960	1.771	2.326	no capsize
caps11.dat	70	5.386	2.257	2.482	no capsize
caps12.dat	75	5.890	2.714	2.915	no capsize
caps13.dat	80	6.283	2.568	3.044	no capsize
caps14.dat	85	6.732	2.613	3.172	no capsize
caps15.dat	90	6.981	2.984	4.031	no capsize
caps16.dat	95	7.540	2.577	3.761	no capsize

Table C.2: Capsize test details, cont.

Data File	wave maker frequency setting	wave frequency [rads/s]	steady state wave amplitude [cm]	max wave amplitude [cm]	Comments
caps17.dat	60	4.597	2.196	2.674	no capsize
caps18.dat	65	4.960	2.310	2.808	no capsize
caps19.dat	70	5.386	2.494	2.944	no capsize
caps20.dat	75	5.712	3.302	4.053	i.c. capsize
caps21.dat	80	6.283	2.915	3.782	i.c. capsize
caps22.dat	80	6.283	2.833	3.480	i.c. capsize
caps22.dat	80	6.283	2.939	3.705	i.c. capsize
caps23.dat	85	6.732	2.974	3.707	capsize
caps23.dat	85	6.732	3.164	4.307	capsize
caps24.dat	90	6.981	3.210	3.663	i.c. capsize
caps24.dat	90	6.981	3.609	4.738	i.c. capsize
caps24.dat	90	7.250	3.163	4.014	i.c. capsize
caps25.dat	95	7.854	3.295	4.059	capsize
caps26.dat	100	7.854	3.310	4.439	capsize
caps26.dat	100	8.195	3.184	4.795	capsize
caps27.dat	100	7.854	2.745	3.651	capsize
caps28.dat	95	7.854	2.931	3.508	i.c. capsize
caps29.dat	90	7.250	3.002	3.680	i.c. capsize
caps30.dat	85	6.732	2.863	3.802	no capsize
caps31.dat	85	6.732	3.007	3.511	i.c. capsize
caps32.dat	80	6.283	2.764	3.544	no capsize
caps32.dat	80	6.283	2.768	3.122	no capsize
caps37.dat	74	5.712	3.352	4.079	no capsize
caps39.dat	50	3.696	3.806	4.295	no capsize
caps40.dat	55	4.098	3.503	4.617	no capsize
caps41.dat	60	4.488	4.897	5.434	no capsize
caps42.dat	65	4.960	5.135	6.347	no capsize
caps45.dat	70	5.386	5.375	7.093	capsize
caps46.dat	67	5.094	4.291	6.024	capsize
caps47.dat	66	4.960	4.322	5.265	no capsize